SUPERCRITICAL CARBON DIOXIDE (scCO$_2$) PROCESSING OF DISPERSED POLYMER/CLAY NANOCOMPOSITES: STRUCTURAL AND BARRIER PROPERTIES

by

Fengyuan Yang

A dissertation submitted to Johns Hopkins University in conformity with the requirements for the degree of Doctor of Philosophy

Baltimore, Maryland

May, 2014

ABSTRACT

Improved polymeric packaging materials have significantly economic and environmental impact on food, beverage and other industries. In this dissertation, we developed polymer/clay nanocomposites, by incorporating impermeable layered silicates into polymeric matrix to enhance barrier properties. We utilized the unique properties of super critical carbon dioxide ($scCO_2$) to exfoliate clay layers and improve polymer-clay interactions, which are two key challenges in the field of nanocomposites.

Firstly, the $scCO_2$ processing was applied to pre-disperse various commercial Cloisite® clays, the effects of $scCO_2$ processing and chemical and physical properties of clay particles on clay pre-dispersion were investigated and the extent of clay pre-dispersion was assessed by SEM, WAXD and TGA. We found that the $scCO_2$ processing results in pre-dispersion of organic modified clays regardless what kind of modifier on them. The degree of dispersion of different kind of clays actually is a competitive result between carbon dioxide-philicity and modifiers interaction. In addition, TGA data confirm that the $scCO_2$ processing does not remove surface modifiers from clays, which maintain good solubility of clay in organic solvent and compatibility with organic phase.

Secondly, the pre-dispersed clay particles were solution blending with polystyrene (PS) to form nanocomposites, whose structural physical properties were characterized and evaluated by WAXD and TEM. The effects of $scCO_2$ processing, clay dispersion, modification and fraction on improvements of physical properties such as rheology and barrier of nanocomposites were investigated. In addition, structure-barrier properties relationship was assessed based on several phenomenological models. In particular, we identified that 10A is the best reinforcement for improving PS barrier properties.

Microstructural and barrier properties characterizations revealed that $scCO_2$ processed clays prevent reorganization of platelets and lead to more homogenously clay dispersion with improved interfaces. As the increase of clay fraction and dispersion, gas permeation decreased continuously, in this study ~83% reduction of permeation had been achieved with 3.1 vol% of $scCO_2$ processed clays with a calculated effective aspect ratio of 109.

Finally, the concept of $scCO_2$ processing reinforced polymer/clay nanocomposites based on PS matrix was translated to more complex melting extrusion of engineering polymers, such as polyethylene terephthalate (PET) and high density polyethylene (HDPE). The effects of $scCO_2$ processing, clay dispersion, modification and fraction and temperature on improvements of structural and physical properties of matrix were investigated and discussed. 30B and 20A were identified as the best candidate for improving barrier properties of PET and HDPE respectively. Similarly, we found that $scCO_2$ processed clays lead to more homogenously clay dispersion with improved interfaces. Nevertheless, unlike previous research, permeation of PET did not decrease continuously with increase of clay fraction or dispersion. In this study, with only 1wt% of clay, pre-dispersed clay lead to a more significant reduction of oxygen permeation (~33%) than as-received clay did (~8%) and a maximum reduction (44%) of oxygen permeation was achieved by adding 3wt% of pre-dispersed clay. In addition, we confirmed that effect of temperature on the permeation of PET/clay nanocomposites depended both on the Arrhenius behavior of the organic phases and tortuous path effect, where improved clay dispersion resulted in a higher effective activation energy. Moreover, both the transparency and mechanical properties have been improved by using $scCO_2$ processed clay.

ACKNOWLEDGMENTS

CONTENTS

LIST OF TABLES

LIST OF FIGURES

CHAPTER 1: INTRODUCTION

1.1 Motivations

1.1.1 Overview

It is natural for people to recognize that numerous chronic and acute illnesses could result in death, because everyone, no matter where you live and how rich you are, has nearly equal possibility of suffering those illnesses. However, hunger and malnutrition, in fact are listed as the top causes of leading human death. When you logon the website of World Food Programme and search key word for hunger, a very impressive image will show up [1].
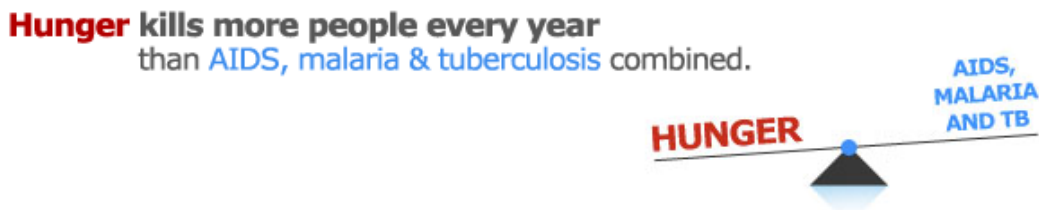
Figure 1 Cartoon poster from World Food Programme website.

A simple cartoon of teeterboard (Figure 1) indicates a startling fact that hunger kills more people every year than AIDS, malaria and tuberculosis combined. Those people from developed countries may be not suffering for hunger or malnutrition themselves and wondering asking for detailed statistics about hunger and malnutrition. To help answer these questions, I cite a list of facts on world hunger provided by World Food Programme.

- 870 million people in the world do not have enough to eat. This number has fallen by 130 million since 1990, but progress slowed after 2008.

- Asia and the Pacific have the largest share of the world's hungry people (some 563 million) but the trend is downward.

- Poor nutrition causes nearly half (45%) of deaths in children under five - 3.1 million children each year.

- One out of six children -- roughly 100 million -- in developing countries is underweight.

- 66 million primary school-age children attend classes hungry across the developing world, with 23 million in Africa alone.

- WFP calculates that US$3.2 billion is needed per year to reach all 66 million hungry school-age children.

According to another report from World Health Organization, hunger-associated disorders kill 36 million people each year worldwide. This is more than coronary heart disease, stroke and other cerebro-vascular diseases, lower respiratory infections, chronic obstructive pulmonary disease, diarrheal diseases, HIV/AIDS, tuberculosis, tracheal, bronchial, and lung cancers, road traffic accidents, and premature or low birth weight combined. Details of statistical data are available in Figure 2 [2].
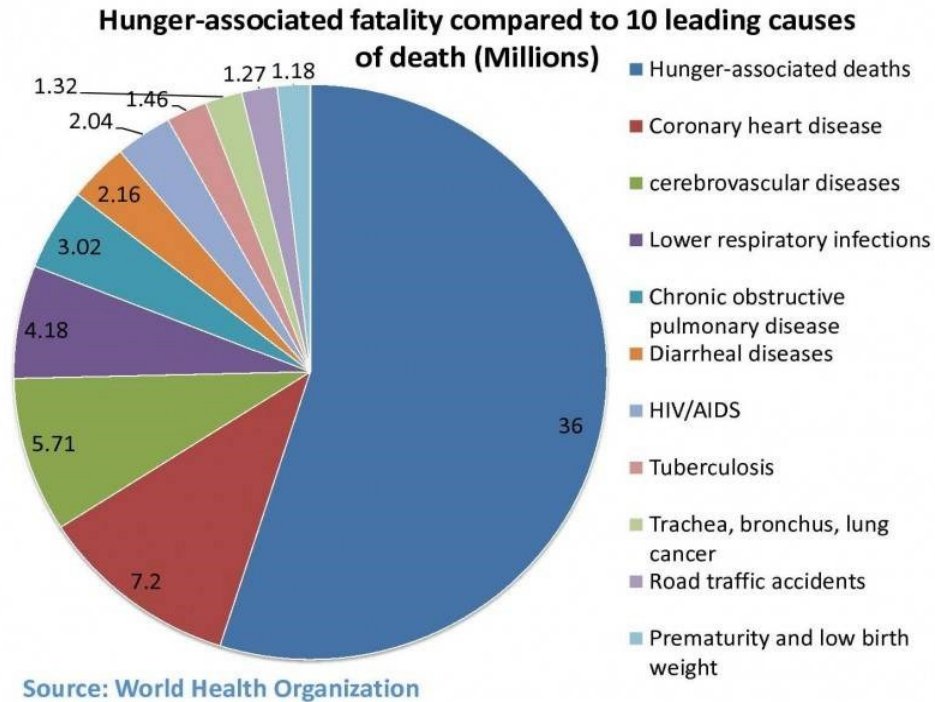
Figure 2 Hunger-associated fatality compared to 10 leading causes of death.

After reviewing those data and facts, people may gain enough awareness and start thinking how we can defeat the battle with serious food crisis. Naturally, people will pay their attention on increasing food production such as grain products and meat, by developing organic agriculture, stock raising and fish culture. However, actually, for the past two decades, the rate of global food production has increased faster than the rate of global population growth. The world already produces more than 1.5 times enough food to feed everyone on the planet [3]. Therefore, in fact, hunger is mainly caused by poverty and inequality, rather than scarcity [4]. Moreover, beside poverty and inequality, food losses, referred as the decrease in edible food mass throughout the part of the supply chain that specifically leads to edible food for human consumption, is also attributed to have a big contribution to world hunger. The results of a recently study suggest that roughly one-third of food produced for human consumption is lost or wasted globally, which amounts to about 1.3 billion tons per year [5].

Food losses take place at production, postharvest and processing stages in the food supply chain. The causes of food losses and waste are mainly connected to financial, managerial and technical limitations in harvesting techniques, storage and cooling facilities in difficult climatic conditions, infrastructure, packaging and marketing systems [6]. Among all of those causes, insufficient and ineffective food packaging system contributes a huge portion (~25%) to the total food losses. The principal roles of food packaging are to protect food products from outside influences and damage, to contain the food, and to provide consumers with ingredient and nutritional information. The goal of food packaging is to contain food in a cost-effective way that satisfies industry requirements and consumer desires, maintains food safety, and minimizes environmental impact. Food packaging can retard product deterioration, retain the beneficial effects of processing, extend shelf-life, and maintain or increase the quality and safety of food. In doing so, packaging provides protection from three major classes of external influences: chemical, biological, and physical. Therefore, developing a qualified, effective and reliable food packaging system will be helpful leading to a reduction in food losses, which consequently could have an immediate and significant impact on solving food crisis and world hunger [7].

In order to fulfill the requirements for an effective and reliable food packaging system, people have never stopped working on innovation in food packaging materials ever since our ancient ancestor. For example, historical research suggests that about 5000 years ago, people started using pottery to preserve extra food for later or winter when there is food shortage [8]. Recently, with the innovations and developments in mining, metallurgy, polymer science, biology and manufacturing, people keep on developing new

generations of food packaging materials. In fact, tens of hundreds of different materials have evolved with rather specialized characteristics that meet the needs of our complex food packaging system. As shown in the following figure, during the last approximately 100 years, Coca-Cola bottles have experienced glass, plastic and renewable/sustainable packaging eras, which helping improve the quality of people's daily lives.

Facing with the fact people need superior and improved food packaging materials to win the critical battle against serious food crisis, materials scientists and engineers may play a significant role in developing superior and improved food packaging materials.

1.1.2 Polymeric packaging materials

Packaging material design and construction determining the shelf life of food products play significant roles in food packaging system. The right selection of packaging materials and technologies maintains product quality and freshness during distribution and storage. Materials that have traditionally been used in food packaging include paper, cardboard, glass, metals (aluminum foils and laminates, tinplate, and tin-free steel) and plastics.

Figure 3 Classification of packaging materials in an example of Coca-Cola bottles.

As shown in the classic figure (Figure 3) from the standard introductory textbook for materials science and engineering students, beside paper and cardboard packages, solid packaging materials can be conveniently grouped into three basic categories: metals, ceramics, and polymers [9]. This scheme is based primarily on chemical makeup and atomic structure. Actually, except paper and cardboard packages, all of other packaging materials fall into one distinct grouping or another. Each category of packaging materials possesses its own specialized structures and characteristics which endow it with some

unique properties, which can be utilized to manufacture food packages with specific applications. On the other hand, their unique structures also could result in particular disadvantages that limit their applications.

For example, atoms in metals and their alloys are arranged in a very orderly manner, and in comparison to the ceramics and polymers, are relatively dense, which gives them excellent barrier properties. With regard to mechanical characteristics, these materials are relatively stiff and strong, yet are ductile (capable of large amounts of deformation without fracture), and are resistant to fracture, which accounts for their widespread use in high pressure food can applications. On the other hand, metallic materials have large numbers of non-localized electrons, and many properties of metals are directly attributable to these electrons. For example, metals corrode easily and are not transparent to visible light, which limits their application in some food packages which require resistant to corrosive components.

Ceramics are compounds between metallic and nonmetallic elements; they include aluminum oxide, silicon dioxide and silicon carbide and, in addition, what some refer to as the traditional ceramics, those composed of clay minerals, as well as cement and glass. Typically, ceramic materials are relatively stiff and hard and insulate to the passage of heat and electricity, and are more resistant to high temperatures and harsh environments than metals and polymers. This makes them superior food containers which are durable and microwavable. However, ceramics have extreme brittleness and are highly susceptible to fracture. Therefore, ceramic packages require more matter to make them strong enough, which increases the deadweight of the package and limits their wide application.

Some of the common and familiar plastics are polyethylene terephthalate (PET), polyethylene (PE), polypropylene (PP) and polystyrene (PS). All of them are organic polymers, with low densities, whereas their mechanical characteristics are generally dissimilar to the metallic and ceramic materials—they are not as stiff or as strong as these other materials. However, on the basis of their low densities, many times their stiffness and strength on a density basis are comparable to the metals and ceramics. In addition, many of the polymers are extremely ductile and pliable, which means that they can easily be formed into complex shapes. Those advantages lead them wiedly been used in various type of food packages such as boxes, bottles and bags, with relatively good mechanical performance. However, one of many drawbacks to the polymers is that they have very large molecular structures, which result in large intrinsic 'free volume'. Small gases or water molecules tend to be absorbed within the free volume and diffuse through them, leading to poor barrier properties in final products which limit their applications in beer, beverage and diary packages. Therefore, these products are sensitive to oxygen, moisture or loss of carbon dioxide [10]. Although plastics have other disadvantages beside low barrier property, they still share 20.6% of total consumption of packaging materials and present a 38.3% yearly increase in 2002 [11]. Another report indicates consumption of metal packaging represented over 15% of the 2010 market but will be losing market share to competing products, especially rigid plastic, to represent only 14% of the 2016 market, while demand for plastic containers is anticipated to accelerate at the same time [12].

Based on the above discussion, among those potential candidates for superior food packaging materials, polymer-based packaging materials are more competitive than metal and ceramic packaging materials due to their superior mechanical property,

processability, and light weight. However, their major disadvantage-low gas and water barrier properties could be the fatal defect limiting their tremendous applications in the food packaging industry [13]. In order to overcome the low barrier property of polymeric packaging materials, many practical solutions have been studied and developed. For example, surface coating techniques have been introduced and studied. Basically, this approach coats polymer surface with a thin layer of metal or ceramic materials which has higher barrier property [14, 15]. Another effective approach for improving barrier property of polymer is a multiple layer processing method named lamination, where a thin layer of materials with higher barrier property is sandwiched between two layers of the highly permeable polymer. The lamination processing techniques have been applied to produce thin polymer films with improved barrier property, as suggested by the fact that 70% of barrier PET bottles today are multi-layer structures [16]. In above solutions, however, the inherently large property disparities between substrate materials and additional materials, make processing complicated, with interfacial disparities.

1.2 Polymer/clay nanocomposites

Taking into account the significant demands in food packaging for transparent containers with high barrier property, and considering the various processing drawbacks of previous approaches to improve barrier property of polymeric packaging materials, my dissertation aims to improve the poor barrier property of polymeric packaging materials by using polymer/clay nanocomposites technology which has been proven to be an effective solution and be relatively cheap and simple could be adopted by current manufacturing processes [17]. In order to overcome the widely well-known obstacles for forming polymer/clay nanocomposites, namely poor clay dispersion and interfacial

interactions, [18, 19] I utilize improved supercritical fluid processing technique to pre-disperse nano-clays, and further compound them with polymers to form polymer/clay nanocomposites. In this section, I focus on several topics related with polymer/clay nanocomposites, while the relevant details for supercritical carbon dioxide processing will be introduced and discussed in the following section.

1.2.1 Barrier property of polymer/clay nanocomposites

Gas/water permeation in a polymeric membrane or film is a complex process that consists of three main stages: initially the gas/water molecules are adsorbed on one side of membrane surface, and then they diffuse through the bulk region of membrane, finally, they reach the other side of membrane surface and desorb from the film. During adsorption, the gas/water molecules are positioned in the free volume holes of the polymer that is created by Brownian motions of the chains or by thermal perturbations. The diffusion process occurs by jumps through neighboring holes. Thus, it depends on the number and the size of these holes (static free volume) and on the frequency of the jumps (dynamic free volume). The static free volume is independent of thermal motions of the macromolecules and is related to the gas solubility, while the dynamic free volume originates from the segmental motions of the polymer chains and is related to the gas diffusivity [20].

Both adsorption and diffusion affect the permeation of gas/water molecules through polymer [21]. Thus, the permeability coefficient, P, can be written as a product of the diffusion coefficient, D and the sorption coefficient or solubility, S, as the following equation.

$$P = D \times S$$

The diffusion coefficient is a kinetic factor that reflects the mobility of the gas molecules in the polymeric phase, whereas the solubility coefficient is a thermodynamic factor related to the interactions between the polymer and the permeants molecules.

Barrier properties are found to be significantly improved for polymer/clay composites, since adding high aspect ratio clay particles to a polymer matrix increases the tortuosity inside the membrane [22-26]. The mass transport mechanism of permeants through a clay-reinforced polymer is somewhat similar to that in a semi-crystalline polymer [27]. It is generally accepted that the transport mechanism within the polymer matrix follows Fick's law, and that the matrix maintains the same properties and characters. One of the first attempts to describe the permeability of polymeric membranes, where a second phase (crystalline region) is dispersed in matrix (amorphous region) with a regular arrangement manner, was made by Barrer and Petropoulos [28]. These authors calculated the diffusion through a regular array of parallelepipeds of a second phase dispersed in a matrix with different diffusion coefficients. When this approach is applied in the case of polymer/clay nanocomposites, the nanocomposites are considered to consist of a permeable phase (polymer matrix) in which non-permeable clay particles are dispersed. There are three main factors that influence the permeability of a nanocomposites: the volume fraction of the clay particles; their orientation relative to the diffusion direction; and their aspect ratio [21, 24, 29, 30].

Based on tortuosity theory, the change of the permeability is found to be proportional to the fractional cross section that is available for the permeants to move forward and depends on the tortuosity of the path, which can be expressed by the following equation.

$$P = D \times S = (1-\phi)S_0 D_0 \tau = (1-\phi)P_0 \tau$$

Where, P, D and S are permeability coefficient, diffusion coefficient and solubility coefficient of nanocomposites and P_0, D_0 and S_0 are permeability coefficient, diffusion coefficient and solubility coefficient of neat matrix. ϕ is volume fraction of clay particles, and τ is the tortuosity factor which is calculated as a function of both volume fraction and aspect ratio of the clay particles. In this approximation, the solubility does not depend on the morphological features of the phases. The clay particles act as impermeable barriers to the diffusing molecules, forcing them to follow longer and more tortuous.
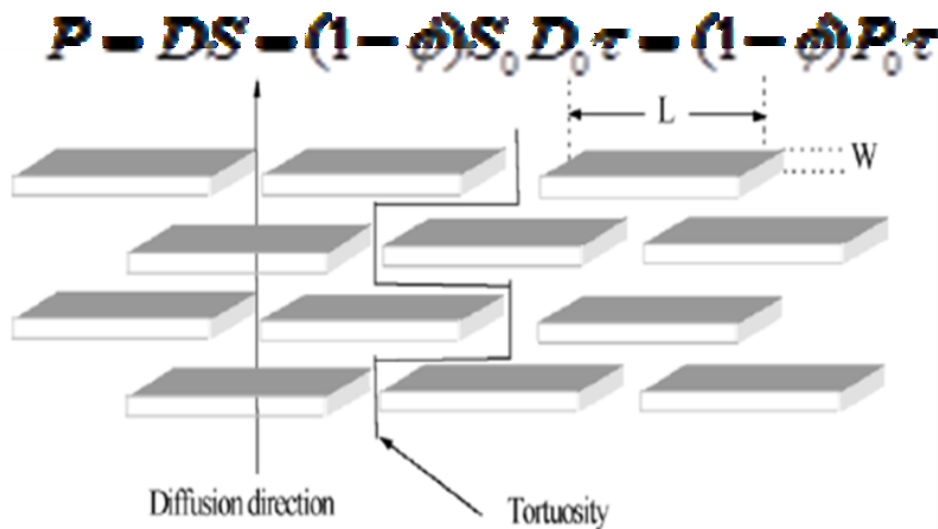
Figure 4 Nielsen model of predicting permeability of nanocomposites with regularly arranged slab shape clay particles based on tortuosity theory.

A simple permeability model for a regular arrangement of clay particles has been proposed by Nielsen [31] and is presented in figure 4. The clay particles are evenly dispersed and considered to be rectangular platelets with finite width, L, and thickness, W. Their orientation is perpendicular to the diffusion direction. Later, several modifications and improvements have been considered and added to mimic more reality structure of polymer/clay nanocomposites and improve accuracy of the model. For example, Cussler

et al. conducted systematic studies and proposed two models to take into account additional factors, including the shape, dimensional polydispersity, and array distribution of the dispersed clay particles [32]. The diffusion in nanocomposites containing oriented and randomly arrayed 3D disk shape clay particles were molded by both Fredrickson and Bicerano [33], and Gusev and Lusti [34] based on a second-order approximation from multiple scattering formulation and finite element calculation, respectively.

Figure 5 demonstrates an analytical solution of relative permeation, the ratio of permeation of nanocomposites respect to neat polymer matrix, as a function of aspect ratio and volume fraction of inorganic clay particles by using Nilsen model [31] as we discussed.
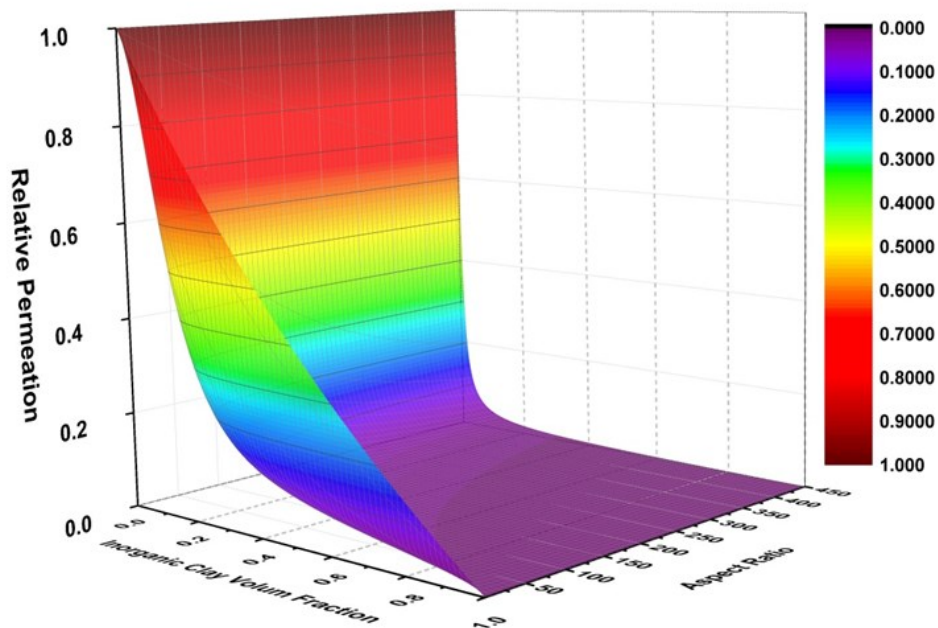
Figure 5 Nielsen model of predicting relative permeation of nanocomposites as a function of aspect ratio and volume fraction of inorganic clay particles [31].

We can see that permeation of nanocomposites continuously decrease with increase of aspect ratio or volume fraction of inorganic clay particles. Theoretically, with large enough aspect ratio or high volume fraction of clay particles, the permeation of

nanocomposites could infinitely approach to zero. Ideally, only by incorporating less than 5vol% of clay particles with aspect ratio of 200-300, the permeation of nanocomposites could decrease by 50%, which corresponding to an improvement of barrier factor by 2. In another word, if we use those nanocomposites as food packaging materials, we could simply double the shelf life of the food by only incorporated less than 5vol% of clay particles.

1.2.2 Montmorillonite

Base on the above analytical study, the structure and morphology of clay particles have significant effect on improving barrier property of polymer/clay nanocomposites, therefore choosing clay particles with specific physical and chemical structure and property are critical to this research. Even though many nano-silicate clays with varying structures, cations and surface charges; however, in this study I focus on a natural type of clay-Montmorillonite (MMT) [35] with high aspect ratio and surface area. Moreover, it is abundant, cheap and nontoxic.

MMT is one of the widely used nano filler materials for polymer/inorganic nanoparticle nanocomposites, which possesses subtype of 2:1 layered structure, or phillosilicates. The water content of MMT is variable and it increases greatly in volume when it absorbs water. Chemically it is hydrated sodium calcium aluminium magnesium silicate hydroxide $(Na,Ca)_{0.33}(Al,Mg)_2(Si_4O_{10})(OH)_2 \cdot nH_2O$. A single layer of MMT contains one octahedral sheet and two tetrahedral crystalline sheets. The octahedral sheet consists of hydroxyl groups, oxygen, aluminum, iron, and magnesium atoms. On the other hand, the tetrahedral sheet comprises a central silicon atom and four oxygen atoms or hydroxyl groups. The structure of 2:1 phyllosilicates is shown in Figure 6 [36-38] .

14
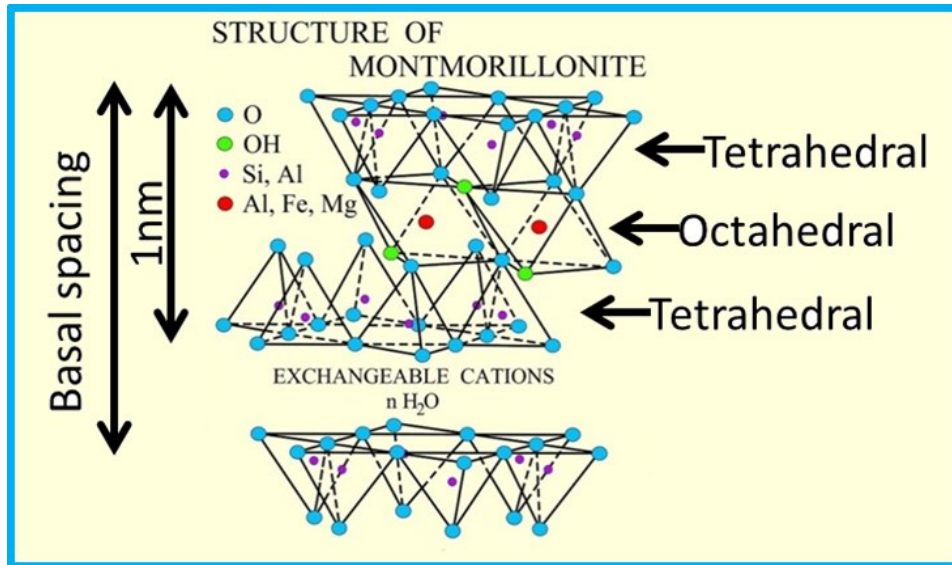
Figure 6 Crystal structure of Montmorillonite.

Generally, at least one dimension of dispersed nano particles in nanocomposites must be in the nanometer range (<100 nm). Typical nano fillers which are currently under investigation are classified by their geometries. Silica nanoparticles and carbon black are examples of nanoparticles, while carbon nanotubes and nanofibers are classified as fibrous materials. Clay layers with plate-like structure belong to layered nanomaterials. The layer thickness of each MMT platelet is on the order of 1 nm and its lateral dimension changes in a wide range from 30 nm to hundred nanometers with an approximate average of 200 nm, which corresponding to a relative large aspect ratio of 200 [39].

Another reason for the layered-clay materials wildly be used to prepare nanocomposites is due to their very large amount of potential interfacial surface area that could be available to interact with the host polymer (760 m^2/g if totally delaminated). The individual layers of these clay platelets are attracted to each other through van der Waal forces. The space between the layers, which is referred to as the interlayer or gallery spacing, is approximately 1nm. The galleries of MMT are occupied by hydrated Na^+, K^+

or Ca^{2+} cations. The ability of clay minerals to hold cations is named the cation exchange capacity (CEC), which is generally expressed as mmeq/100 g clay. Substitution of cations in the tetrahedral sheet (e.g. Si^{4+} is replaced by Al^{3+}) or in the octahedral sheet (e.g. replacement of Al^{3+} with Mg^{2+} or Fe^{2+}) leads to the generation of a net negative surface charge. This replacement of ions with relatively similar sizes is called isomorphous substitution. The negative charge can be counterbalanced by alkali and alkaline earth cations such as Na^+ or Ca^{2+} situated in the gallery [40].
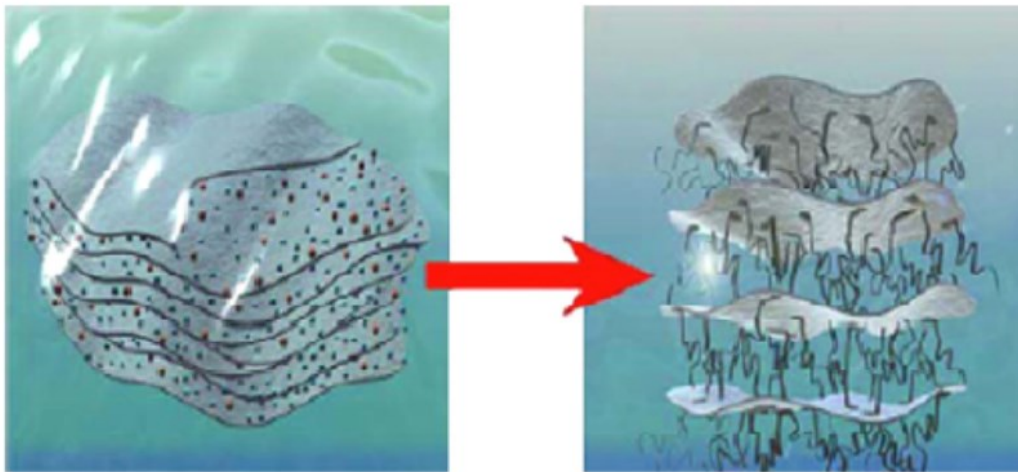
Figure 7 Schematic of nano-clay ion-exchange reaction where the sodium ions are replaced by the ammonium ions rendering the clay more organophilic and increasing the inner gallery spacing.

MMT is highly polar and its surface is hydrophilic. Therefore, delamination of MMT in many engineering polymeric matrices is problematic. In order to make a miscible blend from MMT and polymers it is essential to render the hydrophilic silicate surface more organophilic [41, 42]. Via this conversion, intercalation of most polymeric matrices between silicate nanolayers becomes possible. Cationic surfactants such as alkylammonium, alkylphosphonium and alkylimidazolium can penetrate into the interlayer space of silicate nanolayers via ion exchange reactions [36]. The produced organosilicate has a lower surface energy, higher interlayer spacing, and more ability for

polymer wetting in comparison with unmodified MMT. In some cases these organic modifiers or surfactants possess functional groups interacting with the polymer matrix. Figure 7 displays a schematic representation of a cation exchange reaction between pristine MMT and a cationic surfactant. These cationic surfactants modify interlayer interactions by lowering the surface energy of the inorganic component and improve the wetting characteristics with the polymer. They can also provide functional groups that can react with the polymer or initiate polymerizations of monomers and thereby improve the strength of the interface between the polymer and inorganic. In addition, cation exchange carried out with long chain surfactant molecules increase the gallery spacing between silicate layers. This increasing of gallery spacing helps the diffusion of polymer chains into individual layers [40, 43, 44].

1.2.3 Challenges of forming polymer/clay nanocomposites

As shown in previous sections, the presence of obstructing platelets can slow down the transmission of gases through nanocomposites by creating a long tortuous pathway. Improving barrier property of polymer/clay nanocomposites depends on homogeneous dispersion and delamination of clay in polymeric matrices and superior improvement of polymer-clay interactions, which are regarded as two key challenges in the field of nanocomposites [36, 45].

Generally, depending on the interfacial interaction strength between the polymer matrix and the nanolayers, three main types of polymer layered silicates morphologies may be observed as following descriptions [46, 47].

Immiscible or phase-separated systems, polymer chains are not able to penetrate between the silicate layers gallery spacing. Therefore, the d-spacing of the

nanolayers remains unchanged and the properties of the resulting composites cannot be better than conventional microcomposites.

Intercalated nanocomposites are obtained when polymer chains are inserted in the interlayer gap between the silicate nanolayers. In the intercalated morphology the stacking order of the nanolayers is retained, however due to the penetration of several polymer chains the interlayer d-spacing expands [48, 49].

Delaminated or exfoliated nanocomposites refer to the morphology in which silicate nanolayers are dispersed individually in the polymer host matrix. In this case, the distance between separated layers is typically 10 nm or higher, which depends on clay loading. Remarkable improvements are expected to be obtained via exfoliation of silicate nanolayers within polymer matrices [50, 51].

Figure 8 Schematic representation of the three morphologies of polymer layered silicates, immiscible or phase-separated (A), intercalated (B) and delaminated or exfoliated (C) nanocomposites [52].

Figure 8 illustrates a schematic representation of the three morphologies of polymer layered silicates. Generally, the final morphology of polymer layered silicates is determined by the interplay of entropy and enthalpy changes. The entropy change includes an entropy loss due to the confinement of polymer chains within the interlayer spacing of nanolayers, and an entropy gain because of gallery enhancement and increased conformational freedom of organic modifier chains. If the entropic penalty of polymer

18

confinement is equal to or larger than the entropy gain, enthalpy will determine if intercalation is thermodynamically feasible. The enthalpy of mixing depends on the interactions of the polymer chains with the silicate nanolayer surface and the organic modifier chains [53].

Besides tuning the dispersion of inorganic clay particles within organic matrices, improving polymer-clay interfacial interaction and interface are also critical to optimizing polymer nanocomposite properties and are intrinsically difficult due to their strong enthalpic incompatibility [54-56]. Classic composites theories assume that the incorporation of fillers does not affect the physical and chemical properties of matrix. In another word, the properties of matrix remain the same all over the nanocomposites [57]. However, the enthalpic incompatibility of organic polymer matrices and high surface energy inorganic nanoparticles often leads to phase separation in polymer nanocomposites, which precluding the realization of anticipated property enhancements.
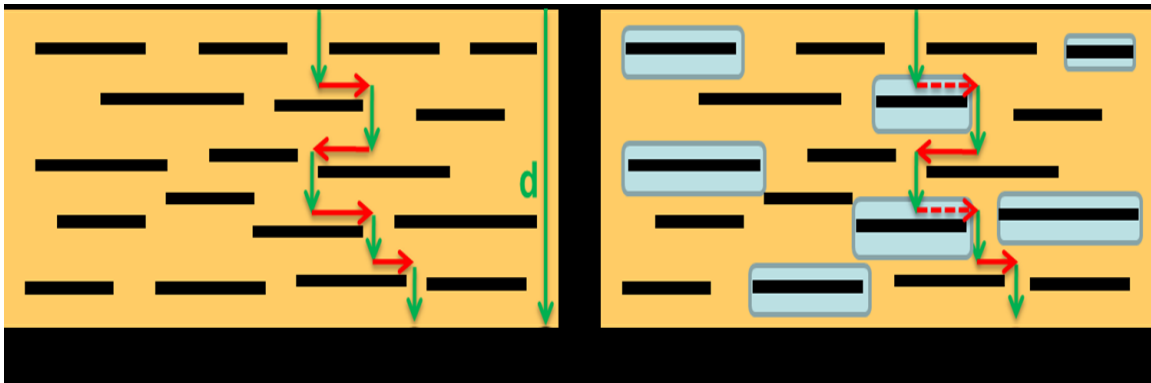
Figure 9 Schematic representation of ideal polymer/clay nanocomposites with effective interface and ineffective interface.

For example, for ideal composites without voids, the presence of the clay particles should decrease the relative permeability for permeants by the corresponding amount of increased tortuosity factor as suggested by detour theory. However, if the particles affect the local properties of the matrix, then the assumptions behind detour theory does no

longer apply. Likewise, it can be argued that voids around clay particles as suggested by Figure 9 would be ineffective obstacles for the permeant molecules. Even worse, they may accelerate the diffusion of permeants molecules, which may form a tunnel which in turn will lead to a deviation from the anticipated relative permeability [58, 59]. Clearly, it is crucial to improve both dispersion and interfacial interaction at same time, if one would like to approach the realization of anticipated property enhancements.

1.2.4 Conventional polymer/clay nanocomposites preparation methods

As we have discussed, enhancement in material properties are directly related to the extent of dispersion of the clay platelets in the polymer matrix and extent of interactions between clay and polymer. The roles of processing, which will affect the orientation, dispersion and morphology of the nanoparticles in matrices and polymer-clay interfacial interaction, have gained sufficient attentions in nanocomposite production. Many of the present research in clay nanocomposites are focused on overcoming the difficulties in separating and evenly dispersing the clay layers in the polymer matrix through different processing methods, while still maintaining the high aspect ratio of the clay layers. Separating the clay layers will allow for a higher surface area to be available for better polymer–clay interactions which in turn contribute to enhancements in polymer/clay nanocomposite properties. The most common strategies for processing nanocomposites fall into one of three categories: in-situ polymerization, mechanical solution blending and compounding/melt mixing [60].

In-situ polymerization was firstly used to prepare polymer/clay nanocomposites by Kojima et al. in a polyamide 6/MMT system [61]. In this method the nano-clay is swollen in monomer and the polymerization is initiated by increasing the temperature or

by the addition of a curing agent or initiator. In-situ polymerization has been shown to give a wide range of dispersion levels with a variety of different property enhancements depending on the polymerization scheme used [62, 63]. The best property improvements were obtained from chain tethering to the surface of the clay or to the modifier during the polymerization process and form a bridge connecting the confined polymer to the rest of the polymer matrix [64]. Although exfoliation may be attainable, in-situ polymerization is complex, expensive, system specific, and can only be utilized at the time of polymer polymerization which limits its applicability in industrial applications [65].
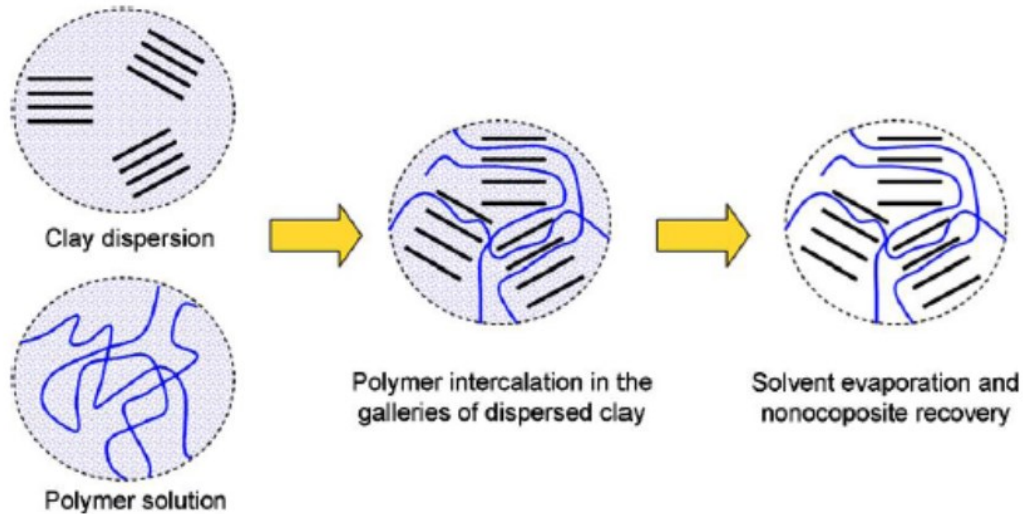
Figure 10 Schematic representation of solution blending technique.

In the solution blending technique as showed in Figure 10, firstly the nano-clay is swollen in an organic solvent. The polymer which is also pre-dissolved in a solvent is added to the clay/solvent solution and intercalation of polymer between the clay layers occurs. The technique requires copious amount of organic solvents which later needs to removed, making this an environmental unfriendly method [66]. Although it is simple in its approach, has generally proven to be relatively ineffective at producing good clay dispersion [67]. Wide spread exfoliation is not seen in these systems due to

thermodynamic barriers present. Clay intercalation increases polymer confinement, which is entropically unfavorable. To overcome such a barrier requires good interactions between the polymer and clay which may not occur due to competition between the polymer and solvent for clay modifier interaction [68].

The melt intercalation process was first reported in 1993 when prepared polystyrene/clay nanocomposites [69]. In this technique a molten thermoplastic is annealed along with an organic-clay at a temperature above the glass transition temperature of the polymer. In this method the polymer chains undergo partial of mass transport in between the clay layers even though the unperturbed radius of gyration of the used polymer are roughly an order of magnitude greater than the inter-gallery spacing of the clay [66]. The polymer losses its conformational entropy during the intercalation and the proposed driving force is the enthalpic contribution of the polymer/clay interactions during annealing [70, 71]. Mechanical compounding is advantageous due to the short processing times, the absence of solvents, and the ease of incorporation into industrial applications, although it has been met with limited success when additives are not used [72, 73]. Although this method can be successful in several systems, in most industrially important polymers, high temperatures must be used to promote chain diffusion into galleries in order to minimize processing time. However, these temperatures can also have a detrimental effect on clay spacing by degrading the organic modifier and causing platelet collapse [74, 75]. The collapse leads to a negative effect on nanocomposite properties since the inter gallery spacing is reduced and fewer polymer chains can penetrate it. This issue is most prevalent for high molecular weight polymers, which have the most demanding processing temperature requirements. Increasing sheer rate can help

to introduce enough energy to assist in clay delamination, yet it also causes a decrease in platelet aspect ratio. To overcome these dispersion limitations, researches have employed polymer modification or added polar compatibilizers and co-polymers to increase the inter-gallery spacing and make the local environment more organophilic enabling dispersion upon application of shear [76]. Functionalized polymers however are a relatively expensive solution to dispersion and need to be tailored to maximize polymer-compatibilizers and compatibilizers-clay interactions. On the other hand, compatibilizers generally have low molecular weight and this can have a negative effect on the nanocomposite properties.

1.3 Supercritical carbon dioxide (scCO$_2$) process

In this dissertation, I explored a more effective, cheap, simple, and green processing technique involving supercritical fluid- supercritical carbon dioxide (scCO$_2$) which has been widely applied in various industrial production such as supercritical fluid extraction, dry cleaning and foaming of polymers, to disperse clay particles and form polymer/clay nanocomposites with homogenousclay dispersion and improved superior polymer-clay interfacial interface [77, 78].

1.3.1 Supercritical carbon dioxide (scCO$_2$)

Supercritical carbon dioxide (scCO$_2$) is a fluid state of carbon dioxide where it is held at or above its critical temperature and critical pressure [79]. The phase diagram of carbon dioxide is showed in Figure 11. Carbon dioxide usually behaves as a gas in air at standard temperature and pressure (STP), or as a solid called dry ice when frozen. If the temperature and pressure are both increased from STP to be at or above the critical point for carbon dioxide, it can adopt properties midway between a gas and a liquid. More

specifically, it behaves as a supercritical fluid above its critical temperature (304.25 K) and critical pressure (74 Bar or 7.39 MPa), expanding to fill its container like a gas but with a density like that of a liquid.

scCO$_2$ has diffusivity, viscosity and solubility comparable to a gas, but a tunable density near that of a liquid. They have been receiving attention in various applications from including food and pharmaceutical industries as well as in the plastics industry. Particularly, carbon dioxide is non-toxic, non-flammable, abundant, recoverable, and it has a relatively low critical point. Using scCO$_2$ as a processing aid does not producing CO$_2$ because it only borrows CO$_2$ from the atmosphere, therefore is an environmental friendly benign process.
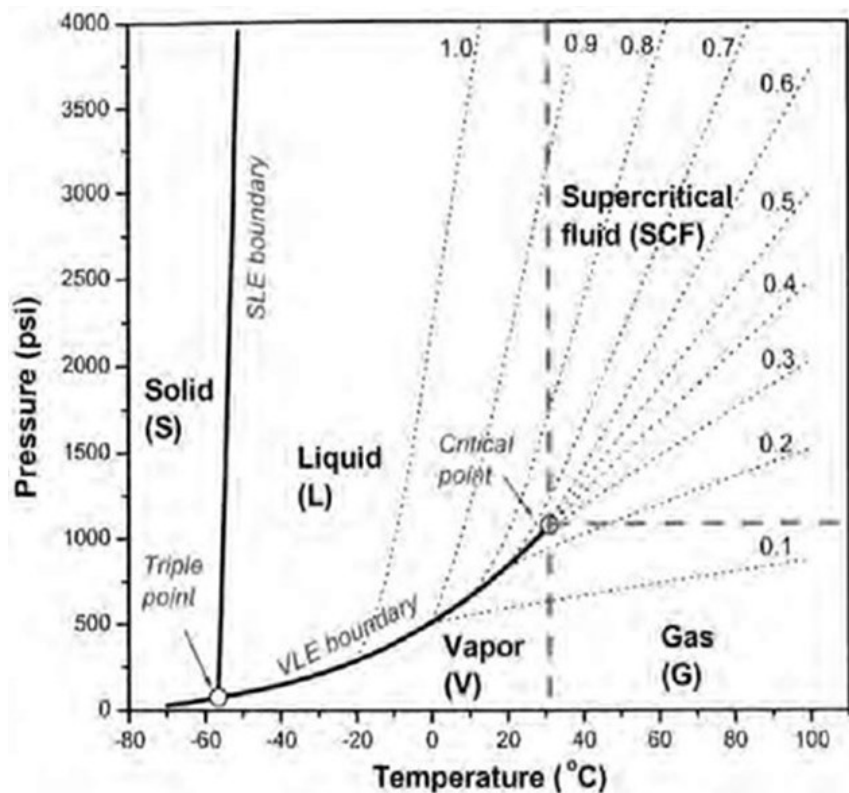
Figure 11 Phase diagram of carbon dioxide.

scCO$_2$ can be used in a wide range of applications in polymer processing including plasticizers, foaming agents and processing solvents [80, 81]. One of the earliest application for scCO$_2$ as an aid for polymer processing is plasticizing agents. scCO$_2$ behaves like a polar, highly volatile organic solvent, which swells and plasticizes polymers when it interacts with them. scCO$_2$ is proven to be efficient for lowering the viscosity of high molecular weight polymers of various polymer melts [82, 83].

Clearly, tremendous applications of scCO$_2$ in polymer processing inspire us it may have potential applications as processing aids used for the impregnation of polymer matrices with additives, such as forming polymer/clay nanocomposites [84].

1.3.2 scCO$_2$ processing strategies, setups and mechanism

Three strategies are designed to produce polymer/clay nanocomposites using the scCO$_2$ processing technique. In the first approach the nanoclay including natural, commercial or customized sample is processed under the appropriate conditions by themselves, without the presence of a polymer matrix. The resulting nanoclay can be solution, in-situ polymerization or melt-mixed/compounded with an appropriate polymer to create a nanocomposite. To our knowledge, this is the only process currently published with the unique ability to disperse clay by itself [85-87].

The second method involves blending the as-received nanoclay with a CO$_2$-philic polymer and processing the resulting mixture in scCO$_2$. It is worth to mention here, the pre-dispersed clay by using the approach above, also can be reprocessed in scCO$_2$ again with the presence of a polymer to make a nanocomposite with improved properties [88].

A third method, similar to the second one involves the use of a solvent along with the polymer and nanoclay to assist in processing [78, 89]. This method is employed when

polymers with a high glass transition temperature (Tg) are used to increase polymer solubility. Also, due to the limited thermal stability of the clay modifiers, processing at high enough temperatures and for long enough times to make processing polymers with high Tg feasible would cause platelet gallery collapse. To address these issues, a concentrated solution of polymer in solvent is used in place of pure polymer to allow decreasing processing temperatures. Furthermore, to optimize the clay disorder upon depressurization, it is preferential to have the most dramatic CO_2 density change possible. The density change decreases the farther for the higher critical temperature the material is processed at, which can be proved by study the phase diagram of carbon dioxide in Figure 11.
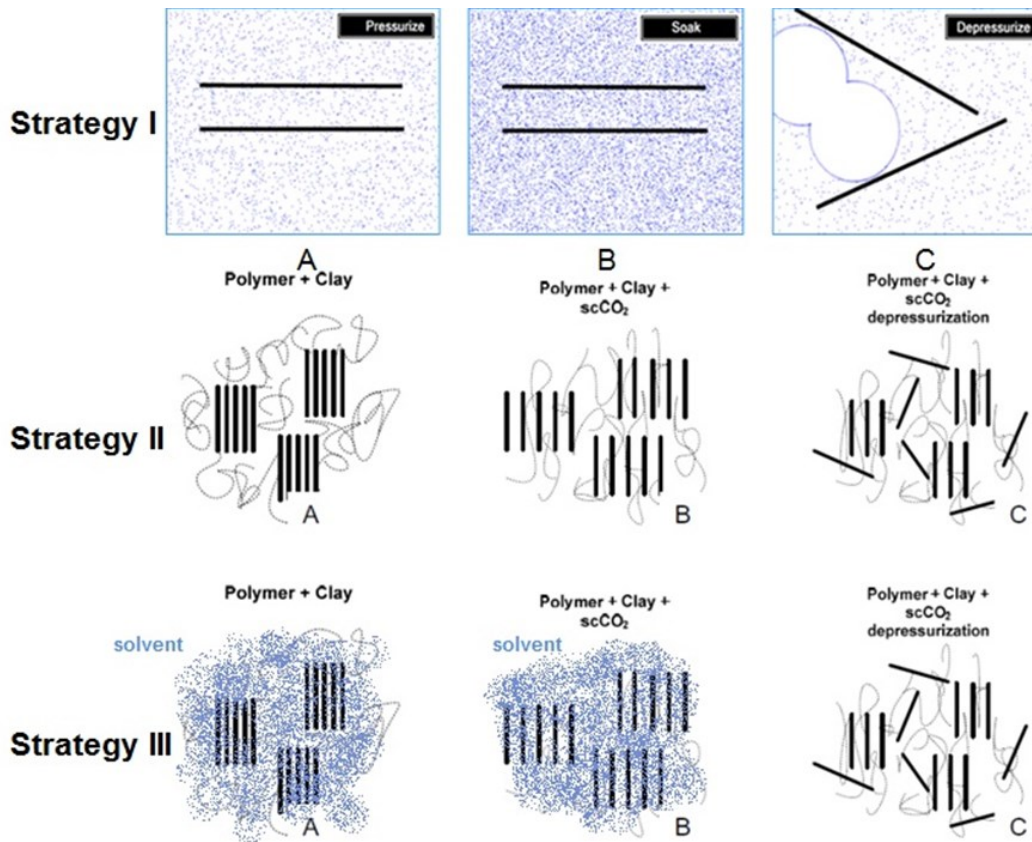
Figure 12 Sketch of proposed scCO$_2$ processing methods.

The scCO$_2$ processing methods are displayed in Figure 12. Basically, all of different processing strategies involve three steps as shown in above figure A, B and C. Step A represents the pre-loading or pre-mixing of the targeting processing system which could be nanoclays, the polymer/clay mixtures or the polymer/solvent/clay mixtures. It is worth to mention here that in the case where a solvent is used the process is very similar as strategy II. The only difference is that the polymer and solvent are loaded in the reactor and hand mixed until the mixture is homogeneous, after which the nanoclay is added to the mixture and again is hand mixed to make sure the there are no clay chunks in the system. Step B involves contacting the nanoclays, the polymer/clay mixtures and the polymer/solvent/clay mixtures with dry scCO$_2$. The pre-loaded or pre-mixed systems are loaded and they are contacted with CO$_2$ in a high pressure vessel. The system is then raised to the desired temperature and pressure, above the critical point of CO$_2$. Following a desired processing time where the mixture is allowed to soak in scCO$_2$. The polymer viscosity can be reduced significantly depending on the polymer solubility in scCO$_2$ due to the solvation effect which helps in polymer processing. Furthermore, by carefully choosing the pressure and temperature of the system, the density and solubility parameter of scCO$_2$ can be adjusted effectively allowing great control over these solvation and expansion effects. During step C, the system is rapidly depressurized to atmospheric pressure [88].
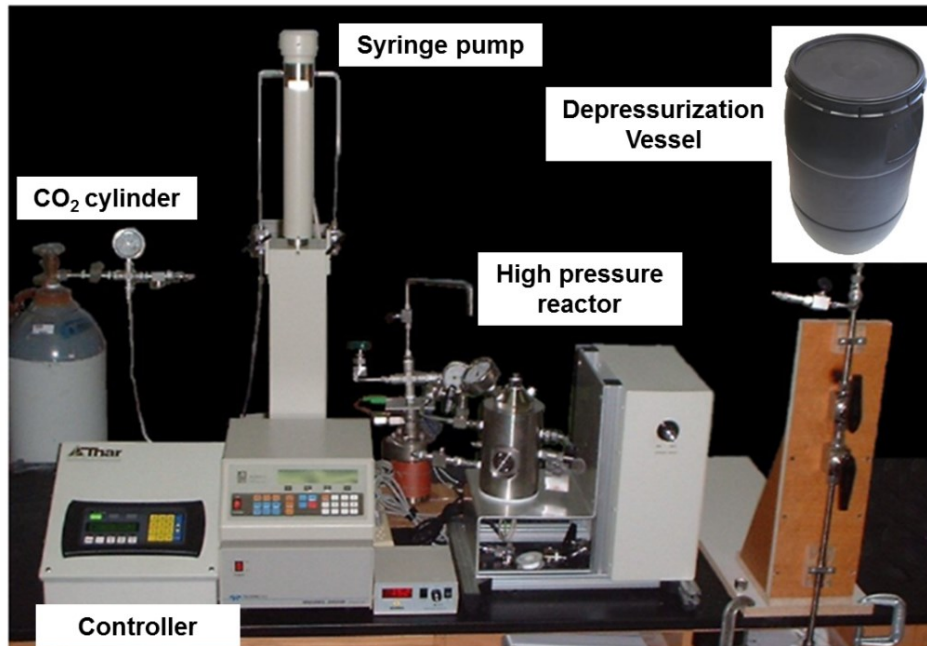
Figure 13 Photo of scCO$_2$ processing facilities and setups.

The proposed hypothesis for the mechanism is that during the soaking step in the case where polymer or polymer/solvent is present, the high diffusivity and low viscosity of the CO$_2$- philic polymer in the mixture enable clay layer penetration. In the case where only CO$_2$ and clay are present the CO$_2$ diffuses into the CO$_2$-philic clay gallery. During depressurization, the outward force due to expansion of the scCO$_2$ between the layers pushes them apart resulting in dispersed nanocomposites or dispersed nanoclays. When the CO$_2$ is completely removed a good portion of the nanoclay platelets remain separated or in the case where polymer is present the organic material remains between the layers, coating the surfaces of the layers, thus preventing most of the reformation of the layered structure [87]. If a solvent is used, it is initially removed under high vacuum and room temperatures and then elevated temperatures and low vacuum to make sure that no residual solvent is left in the nanocomposite [60].

In my dissertation, I will mainly focus on strategy I [87]. The facilities and setups for $scCO_2$ processing are showed in figure 13. The processing vessel used is a 256 mL stainless steel THAR reactor with sapphire windows and is capable of handling pressures up to 69 MPa at 150^oC without and 41 MPa with the magnetic agitator installed. The reactor is outfitted with a series of valves, which control the depressurization rate. The CO_2 is charged into the vessel via a 266 mL Teledyne Isco syringe pump capable of a pressure of 52 MPa and flow rates ranging from 0.001 – 107 mL/min.

1.3.3 Manufacture of nanocomposites by using $scCO_2$

Recently, numerous processing by utilizing $scCO_2$ to prepare superior polymer/nanoparticle nanocomposites have been developed. Multiple $scCO_2$ based processing procedures have been reported to produce nanocomposite with improved physical properties [60, 90]. Basically, $scCO_2$ in those processing technique are used either as solvent or processing aids [82].

$scCO_2$ was widely used as a polar and low viscosity solvent with the combination of the in-situ polymerization method to prepare polymer/clay nanocomposites. Zerda et al. used $scCO_2$ for the synthesis of PMMA/organic-MMT nanocomposites by mixing organic-MMT, MMA, initiator in the $scCO_2$ in a high pressure apparatus. The primary purpose of the $scCO_2$ was to allow MMA monomers to readily diffuse and homogeneously disperse within the gallery spacing of the silicate layers. After the saturation period for mixing, the temperature was raised to complete the polymerization step. Once polymerization was complete, the pressure was reduced to atmospheric conditions over a period of 15hrs. Removal of trapped CO_2 was accomplished by exposing the samples to temperatures above the glass transition to allow foaming to occur.

This technique produced well dispersed, intercalated polymer/clay composites with clay concentration of 40 wt%. Isotropic forms of the 40 wt % composite showed a 50% increase in tensile modulus while melt processed samples containing orientation showed an increase in the tensile modulus of 220% [91]. Qian Zhao et al. prepared Poly (methyl methacrylate)/clay nanocomposites using this technique through in-situ polymerization by using $scCO_2$ as solvent; their results showed partially exfoliated/intercalated structures as well as enhanced thermal stabilities and mechanical properties [92]. However, none of these reports showed the potential for application in industry due to the limited product amount.
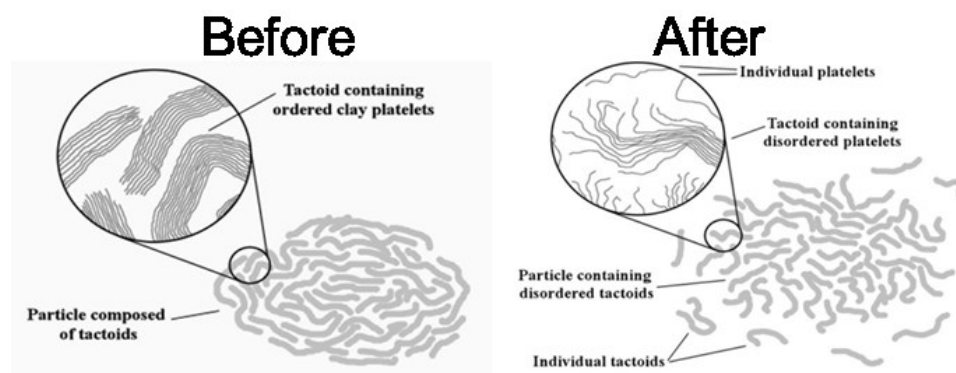
Figure 14 Schematic structure evolution of clay during $scCO_2$ processing [60].

In 2002, Manke et al. first developed a process that used $scCO_2$ as a processing aid and allows clay particles to be pre-socked within $scCO_2$ in a pressurized vessel and then rapidly depressurized into another vessel at atmospheric pressure to force the clay platelets apart [87]. The result showed exfoliated nanoclay particles by X-Ray diffraction. This method relies on the drastic volumetric expansion of $scCO_2$ between aggregated particles upon depressurization that break down particle size and pushes the sheets/platelets apart, effectively disordering and/or dispersing them. When the CO_2 is completely removed, a good portion of the nano-clay platelets remain separated. A

schematic structure evolution of clay during the processing is given in Figure 14. Later, Steven Horsch et al. furthered above study and demonstrated possibility of dispersing multiple types of organic nano-clays by using quiescent $scCO_2$ processing and studied rheological properties of resultant nanocomposites, they found that the extent of clay dispersion depend on the 'CO_2-philicity' and the delaminated nano-clay increase the ability to produce dispersed polymer-clay nanocomposites [85]. It is worth to mention, to the best of our knowledge, this is the only process currently published with the unique ability to disperse clay by itself. Then, Manitiu et al. by using the similar technique and did further study about the effects of $scCO_2$ processing conditions on clay dispersion and polymer-clay interactions in polystyrene (PS)/Cloisite 10A system, where significant dispersion and rheological enhancement have been reported with help of $scCO_2$ processing and co-solvent [60].

The techniques using $scCO_2$ with the combination of melt bending method to prepare polymer/clay nanocomposites also have been developed. Nguyen et al. developed a technique by first saturating the nanoclay in $scCO_2$ and then releasing the nanoclay rapidly back through a stopped extruder filler with polymer pellets, which is showed in Figure 3-5 [90]. The saturation was conducted in a custom pressure chamber designed with an inlet for the addition of CO_2 and an exit with a ball valve for the subsequent release of the mixture. Their results from WAXD showed an increase in the exfoliation levels of the $scCO_2$ produced material as compared to samples produced with dry mixing of polymer and clay. Mechanical tests showed a 17% improvement in the Young's modulus of scCO2 produced composite containing 6.5wt% silicate over composite with the same weight percent of silicate produced from dry mixing of the silicate and clay.

Subsequently, Chen Chen et al. modified above processing method into a semi-continuous process (Figure 15) and compounded polypropylene (PP) /clay nanocomposites with high clay loading (~10 wt%) by using the modified extruder. With help of maleic anhydride grafted polypropylene, they reported results indicating remarkable improvements on modulus and tensile strength of 88 % and 12%, respectively, compared to the pure polymer matrix [93, 94]. By combining the conventional melt blending method with $scCO_2$ technique, one should expect the benefits from both sides, which are excellent dispersion from $scCO_2$ and simplicity, fast speed, and industrial compatibility from melt blending method.
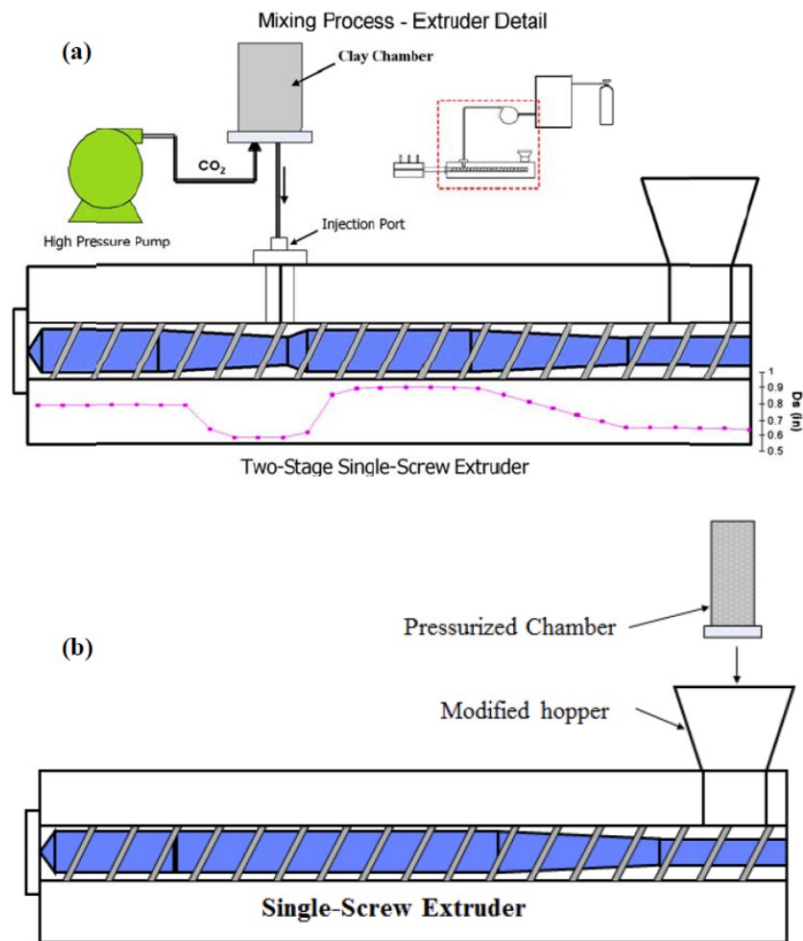
Figure 15 Scheme of extruders equipped with $scCO_2$ processing.

All of above examples proved the fact that scCO$_2$, who has a liquid-like density and gas-like diffusivity can penetrate into the platelet galleries of soaked clays, and then by following an instantaneous depressurization, the large density change of the supercritical fluid pushes the platelets apart to reach exfoliated structure, which result in more available surface for polymeric matrix to penetrate and would lead to a homogeneous and exfoliated dispersion with improved interfacial interaction in final nanocomposites. However, still there is need for gaining a better understanding on what the morphology and properties of the nano-clay is affected after scCO2 processing. Moreover, a better understanding on the effects that different factors such as processing conditions, clay modifiers and different polymers, have on the resulting composites morphology and properties is crucial to optimize the supercritical carbon dioxide processing technique for potential industrial applications.

1.4 Significance of research

1.4.1 Fundamental significance

Materials science and engineering, is an interdisciplinary mainly focused on investigating the relationship between the structure of materials at atomic or molecular scales and their macroscopic properties. In addition to structure and properties, two other important components involved in the science and engineering of materials—namely, processing and performance are considered with attempts of industrial manufactures and real-world application. With regard to the relationships of these four components, the structure of a material will depend on how it is processed. Furthermore, a material's

performance will be a function of its properties. Thus, the interrelationship between processing, structure, properties, and performance is as depicted in the Figure 16.
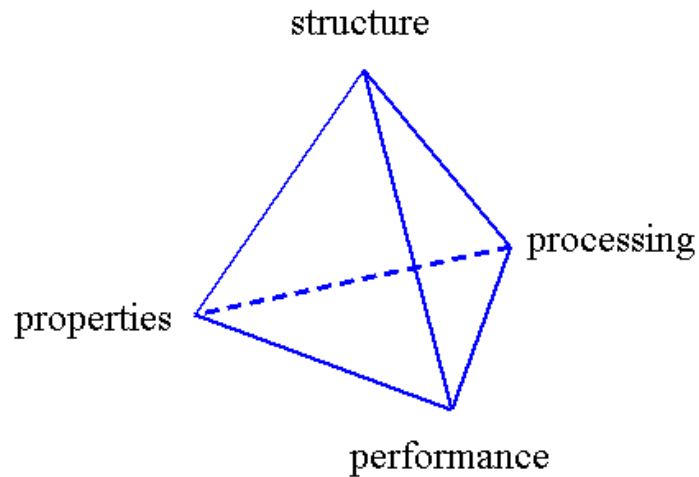
Figure 16 Four components of the discipline of materials science and engineering and their interrelationship.

Throughout my dissertation, I will draw a specific picture of relationship among these four components in terms of design, production, characterization and utilization of materials by using a practical real example. Initially, I start with the demand for high performance food packaging materials with improved barrier properties and design the structure of the raw polymeric materials to fulfill those requirements. Then the relationship between structure and properties will be investigated by using theoretical modeling and physical characterizations. I will optimize the current processing method to overcome obstacles which prevent materials forming and assembling the most wanted structure and property. Moreover, I will think about how to get the most out of the processing to make the method more effective and scientifically viable. By systemically demonstrating four components of the discipline of materials science and engineering and covering and revealing the interacting relationships between them, I will try to gain

insights on how these facts affect each other, within the framework of dispersed polymer-clay nanocomposites.

1.4.2 Food packaging applications

Beside academic significance, the results of the proposed research will have impact and real-world applications in plastic food packaging industry. For example, as we have mentioned, the proposed semi-crystalline polymeric matrix polyethylene terephthalate (PET) in my dissertation is linear thermoplastic polyester which has become an important commercial polymer owing to its rapid market growth. Global demand of PET for packaging applications in 1985 was about 0.5 million metric tons, while in 1990, 1.5 million metric tons of PET was consumed. Seven million metric tons of PET was consumed in 2000, and this increased to more than 10 million metric tons in 2005 in the packaging industry [95].

On the other hand, glass containers, usually used for beverage packaging, are heavier than an equivalent PET bottle. Besides, PET bottles do not shatter or break. The world market for PET resin in packaging could be doubled if PET would gain 50% of the market share in beer bottles. However, delicate flavor of beer, especially light beer, is very sensitive to exposure to oxygen. For example, considering that allowable oxygen concentration limit in beer is 1 ppm, it has been reported that beer quality preservation in typical 1.5 L PET bottles is around one month. Loss of carbon dioxide of carbonated soft drinks leaves a flat drink. Improvement in oxygen and carbon dioxide barrier properties of PET could have significant practical implictaions.[15, 44].

In fact, the preparation of PET nanocomposites with exfoliated morphology and good barrier properties remains challenging, and novel approaches need to be undertaken

to improve these materials. Therefore, practical and real-world applications could emerge, if we can successfully incorporate and exfoliate nanoclay particles into PET matrix and improve PET-clay interaction. For example, if we can decrease the oxygen permeation of PET by 50% which corresponding to a barrier factor of 2. In another words, if we use these improved nanocomposites as beer or beverage package, the shelf time of those product could be doubledincreasing shelf life, and decreasing waste.

1.4.3 Other potential applications

Beside the improved barrier property and potential food packaging applications, polymer/clay nanocomposites with improved dispersion and polymer-clay interaction could also exhibit other superior physical properties and potential applications.

For example, in 1985 the Toyota Central R&D Labs firstly invented polymer/clay nanocomposites and reported significant improvements in the tensile modulus of nanoclay reinforced composite [96-98]. A 69% increase in tensile modulus from 1.11 GPa for pure Nylon-6 to 1.87 GPa for the composite was realized in a composite containing 4.7wt% nanoclay by using in-situ polymerization. In their following reports, the tensile modulus of Nylon-6/clay composite was reported to be doubled by modest additions of clay <5 wt%. These significant improvements in mechanical properties were thought to originate from from the existence of an exceptionally high interfacial surface area and the formation of ionic and/or hydrogen bonds between the organic polymer and inorganic silicate. Moreover, passenger cars equipped with a PCN part were launched in 1989, only 4 years after this discovery, and one year later those cars were driven through towns and fields.

Thermal stability of polymer/clay nanocomposites has been analyzed and compared with that of pure polymer under various oxidative (air) or non-oxidative (inert gases) conditions. In general, it has been reported that the polymer/clay nanocomposites are thermally more stable than pure polymers. Blumstein (1965) first reported the improved thermal stability of PMMA/MMT nanocomposites. TGA showed that PMMA intercalated into the Na-MMT has 40-50°C higher decomposition temperature [99]. The effect of clay layers has been more explained as superior insulation and mass transport barrier against the volatile compounds generated during the decomposition of polymer under thermal conditions. Also it has been reported that clays assist in the formation of layered carbonaceous char during degradation of polymer/clay nanocomposites [100].

Because of the large use of polymers especially in domestic applications, there is need to reduce their potential for ignition or burn in order to make them safe. Enhanced flame retardancy is found for polymer/clay composites with improved clay dispersion and interfacial interactions [101, 102]. Investigations on the polymer/clay nanocomposites have demonstrated that clay minerals represent some degree of flame retardancy along with the improvement in the physical and mechanical properties for polymers. [103, 104].

CHAPTER 2: SUPERCRITICAL CARBON DIOXIDE PROCESSING OF COMERCIAL NANOCLAYS

2.1 Introduction

The supercritical critical carbon dioxide ($scCO_2$) processing method, as mentioned above, was utilized to pre-disperse commercial clays. The effects of chemically and physically intrinsic properties of clay particles and $scCO_2$ processing on pre-dispersion of clay particles were investigated by using scanning electron microscopy, wide angle X-ray diffraction, thermal gravimetric analysis [45] and packing volume/density change measurement.

Previous studies on Cloisite® 10A indicated that after $scCO_2$ processing, 10A clay particles lost their long region ordered layer structure, associated with reduction in particle size. Moreover, $scCO_2$ processing expanded 10A clay particles displayed flexible and puffy structures which result in exposing more available surface area to the polymeric matrix. Subsequently, the effects of processing conditions on the structure and properties of polystyrene/10A nanocomposites were studied and significant improvements in melting rheology of nanocomposites have been achieved by improving clay dispersion [60]. Our previous study proposed a preliminary hypothesis for the mechanism of processing that during the soaking step, under the selected processing conditions, the liquid-like density and gas-like diffusivity of $scCO_2$ allows it to diffuse into the clay layers and roam between the clay galleries. Upon instantaneous depressurization, the large density change of the $scCO_2$ undergoes between the layers and pushes them apart, resulting in delaminated nanoclays. After the CO_2 is completely removed, a good portion of the nanoclay platelets remain separated thus preventing

reformation of the layered structure [60, 85]. The current study was based on above discoveries, to address the mechanism of scCO$_2$ processing and assessment of dispersion, by applying the process to several commercial clays with different chemical and physical properties.

The chemical and physical properties of natural and commercial clays used in this study are summarized in Table 1 [105]. We chose series of Cloisites® clays because those clays possess significantly different varieties on surface chemistry, which attribute them with unique properties from hydrophilic to hydrophobic that can be applied to reinforce a wide range of different engineering plastics with diverse properties. Also, the significant differences of clay surface chemistry can provide good control group to study the effect of surface modification on improving chemical and physical properties of the final nanocomposites, which could be very helpful for researchers to fundamentally study the relationships between structure (both chemical and physical), processing and properties (both chemical and physical).

Table 1 Physical and chemical properties of clay particles.

Nanoclay name	Organic modifier	d_{001} spacing (nm)	Density (g/ml)	Weight loss on ignition (%)
Cloisite®Na$^+$	None	1.2	2.86	8
Cloisite®10A	H$_3$C—N$^+$—CH$_2$—⬡ (CH$_3$, HT)	1.92	1.9	39
Cloisite®20A	H$_3$C—N$^+$—HT (CH$_3$, HT)	2.42	1.77	38
Cloisite®30B	H$_3$C—N$^+$—T (CH$_2$CH$_2$OH, CH$_2$CH$_2$OH)	1.85	1.98	30

Compared with commercial clay, natural clays possesses remarkable thermal stability without decomposition up to 600°C, while organic modified clays normally start decomposition around 220-310°C [74]. Therefore, it could be a breakthrough for high temperature melting compounding of polymer/clay nanocomposites, if superior dispersion can be achieved for natural clay. In addition, the using of exfoliated natural clay could improve the high temperature stability and reduce discoloration. However, previous research on natural clays found that the particles were largely unchanged by quiescent scCO$_2$ processing at comparable conditions [85]. The large particles remained after processing and appeared well ordered like those of the as-received clay. In our current upgrade processing, we introduced a mechanical stirring paddle to the processing system, expecting that stirring system will let all of the natural clay to fully contact supercritical phase, which will allow the supercritical phase to diffuse into inter gallery spaces of the clays, so upon depressurization, the trapped carbon dioxide molecule will escape and lead to dispersion of natural clay, these possibility will be discussed in the sixth chapter.

2.2 Experimental

2.2.1 Materials

Organically modified Cloisite$^®$ 10A 20A and 30B, with reported aspect ratios ranging from 10 to 300 [45] were obtained from Southern Clay Products and their composition and physical properties were summarized in Table 1.

2.2.2 scCO$_2$ processing

The scCO$_2$ processing method exposed certain amount of clay (~15-20g) to CO$_2$ in a high pressure vessel (256ml) equipped with a mechanical stirrer; the system was then

raised above the critical point for CO_2 (50°C and 17.2MPa) and the clay was allowed to soak with intensive stirring over a relatively short processing period (~2-4h). The system was then rapidly depressurized to atmospheric pressure. The processed clay particles were collected by using a sealed stainless steel drum (200L).

2.2.3 Wide-angle X-ray diffraction (WAXD)

A Rigaku Rotaflex Powder Diffractometer with a Cu Kα X-ray source λ=1.54 Å (accelerating voltage=44 kV, current=120 mA) was used to assess the clay intergallery spacing. Clay powder or composite films samples were placed in a custom-made, zero-background quartz sample holder that is 0.9 mm in depth. Several scans were obtained from different locations in the sample and verified to be reproducible when diffraction patterns were superimposed on one another. The 2θ angle was determined using the JADE software that accompanies the diffractometer, and the d_{001} spacing for the clays was calculated using Braggs' Law of diffraction.

2.2.4 Scanning electron microscopy (SEM)

Clay images were collected using a Hitachi S-2400 scanning electron microscope with an electron potential of 25 kV. The samples were sputter coated with gold, and several (10-20) images per sample were collected for all samples to ensure accurate representation of the clays morphology.

2.2.5 Thermal Gravimetric Analysis (TGA)

A Perkin Elmer Pyris 1 thermal gravimetric analyzer with thermal analysis gas station was used to monitor the change of clay's surficial chemical modification before and after scCO$_2$ processing. Thermal gravimetric data were collected from 20 to 650 ^{o}C

with a heating rate of $10^{\circ}C/min$, and whole test under dry air atmosphere with an air flow rate of 20ml/min.

2.2.6 Compact volume/density change measurement

Centrifuge tubes (50ml) were used to measure the volume of nano-clay following scCO2 processing to determine the extent of volume change that the clay undergoes after processing. The measurement was done by measuring the volume it takes for 10 grams of sample. The tubes were repeatedly taped until no further change of volume was seen upon tapping. After the compact volume was obtained the density was calculated based on the following equation. Similar measurements also conducted on as-received clays to serve as control.

$$\rho_C = \frac{10g}{V_C}$$

2.3 Results and discussion

2.3.1 scCO$_2$ processing of Cloisite$^{\textregistered}$ 10A

WAXD was used to determine how the spacing between clay platelets changed upon scCO$_2$ processing. The as-received 10A showed a clear and sharp diffraction peak at $2\theta=4.3°$ corresponding to its equilibrium platelet spacing of 1.05nm (basal spacing minus 1 nm for platelet thickness). In contrast, the scCO$_2$ processed clay displayed a broad diffraction peak around $2\theta=3.8°$ (Figure 17). The shift and broadening indicated an increase of equilibrium platelet spacing to 1.32nm and a significant reduction in parallel registry, where exfoliated morphologies could be present. Similar results also reported by Manitiu et al. [60] and published for 93A using quiescent scCO$_2$ processing [85].
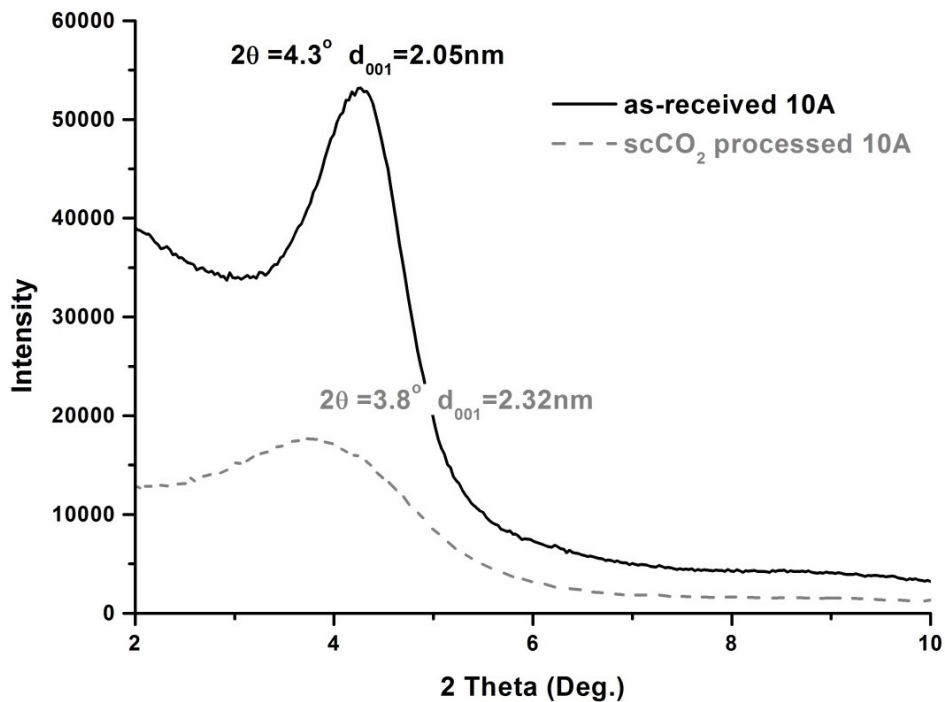
Figure 17 WAXD patterns of as-received and scCO$_2$ processed 10A.

Representative SEM images along with a conceptualized cross section of typical as-received and scCO$_2$ processed 10A are displayed in Figure 18. The as-received clay was composed of cluster of tactoids and particles consisting of a large number of tightly bound tactoids with lateral dimensions of 3-25 μm. It was reported that these tactoids contained a number of highly ordered stacked platelets held together by van der Waals forces [60]. Upon examination of a large number of SEM images in higher magnification (Figure 18 C), it was concluded that the tactoids were closely bound into particles and very few dispersed platelets were observed in the as-received samples [60, 78, 85].
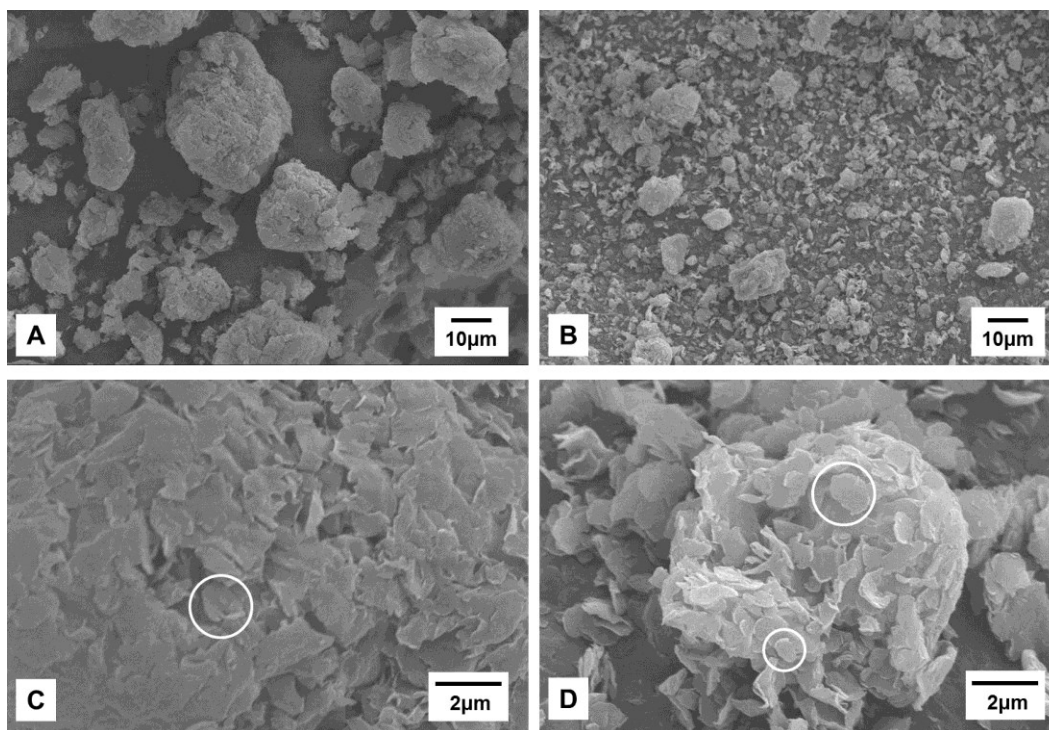
Figure 18 SEM images of as-received and scCO$_2$ processed 10A.

In contrast, the representative images of scCO$_2$ processed 10A displayed a significant change of morphology (Figure 18 B). Even though few fraction particles were found with a lateral size of 3-15 μm, the number of tactoids per particle and the tightness of packing were remarkably reduced (Figure 18 D). Individual tactoids had been delaminated from each other and lost their parallel registry, leaving large spaces into the center of the aggregated particles for polymer to penetrate. Measuring the size of tactoids across multiple images of both materials (a few of which) were indicated by white circles in the figures, we found that although the average particle size had been reduced significantly, the tactoids diameter remained in the range from 0.5-2 μm which indicated that scCO$_2$ processing did not affect the aspect ratio of palettes which is a key factor for improving physical properties [106-108]. Upon depressurization, it appeared that a fraction of the outermost layers was delaminated from the tactoids during CO$_2$ expansion

44

while the much less mobile inner layers just lost the coherent parallel registry. The expanded flexible structure of the $scCO_2$ processed particles/ tactoids exposed more of the available surface area, and should be easier to disperse into a polymer matrix than the as-received clay [60, 85].
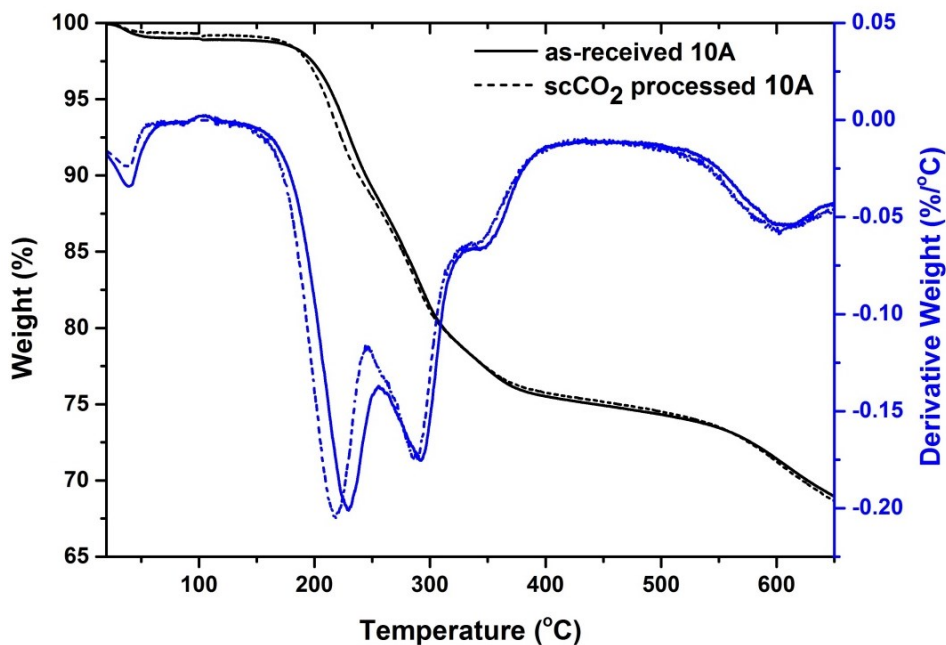
Figure 19 TGA curves of as-received and scCO$_2$ processed 10A.

Clay-polymer interaction plays a significant role on enhancing polymer/clay nanocomposites' physical properties, therefore small organic modifiers are attached on the clays surface to improve their compatibility to polymeric matrix [40, 43, 109, 110]. TGA (Figure 19) was used to monitor surface chemistry change after $scCO_2$ processing. Both as-received and $scCO_2$ processed 10A showed a five stages weight loss curve in temperature range from 20 to 650°C. The first stage was below 100°C, which was related with the release of free water on clay surface or inter gallery space. $scCO_2$ processed 10A possessed less free water may because free water tend to be trapped in the inter gallery space rather than absorbing on the hydrophobic clay surface. Three consecutive stages

were observed between 180 to $400^{\circ}C$, which were attributed to the decomposition of organic modifiers. $scCO_2$ processed clay demonstrated a significant shift of those peaks to lower temperature. We speculated that the puffy structure of processed clay exposed modifiers more accessible to air and facilitated their decomposition. Finally, the last peak around $600^{\circ}C$ was expected to be decomposition of structural water [74]. Additionally, no significant difference in weight loss at $650^{\circ}C$ after processing was observed, which indicated processing expand clay structure without removing modifiers.

Furthermore, the 'loose packed' volume and densities of 10A were measured and given in Figure 20. As we can see that the volume (based on 10g) of 10A increased from 28.5ml to 37ml upon $scCO_2$ processing which corresponding to an decrease of density by 23%. The structures of the pre-dispersed clays remained preserved over 6 months storage at room temperature. Therefore, the pre-dispersion of the nanoclays could enable significantly better dispersion of these clays into the polymer matrix through traditional processing methods.
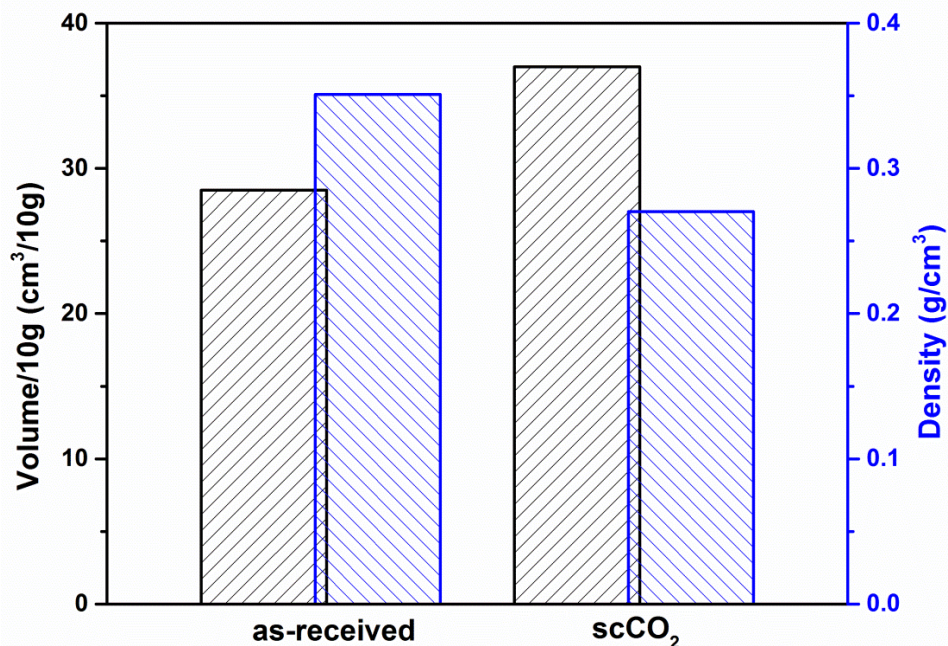
Figure 20 Pack volume/density of as-received and scCO$_2$ processed 10A.

2.3.2 scCO$_2$ processing of Cloisite$^®$ 20A

The changing of spacing between clay platelets upon scCO$_2$ processing was monitored by WAXD. Based on Figure 21, both as-received and scCO$_2$ processed 20A showed a clear diffraction peak at $2\theta=3.2°$ corresponding to an equilibrium platelet spacing of 1.77nm (basal spacing minus 1 nm for platelet thickness) [89]. In comparison, the scCO$_2$ processed clay displayed a sharper and narrow peak which indicated a changing of parallel registry and decrease of the crystal size. Moreover, compared with as-received 20A having a d$_{002}$ diffraction peak around $2\theta=6.8°$ corresponding to a d$_{002}$=2.6nm , scCO$_2$ processed 20A presented a shifted d$_{002}$ peak to lower 2θ, which suggested that long range parallel registered tactoids were broken as a result of scCO$_2$ processing. However, strong interactions between modifiers inside 20A appeared to prevent more substantial dispersion.
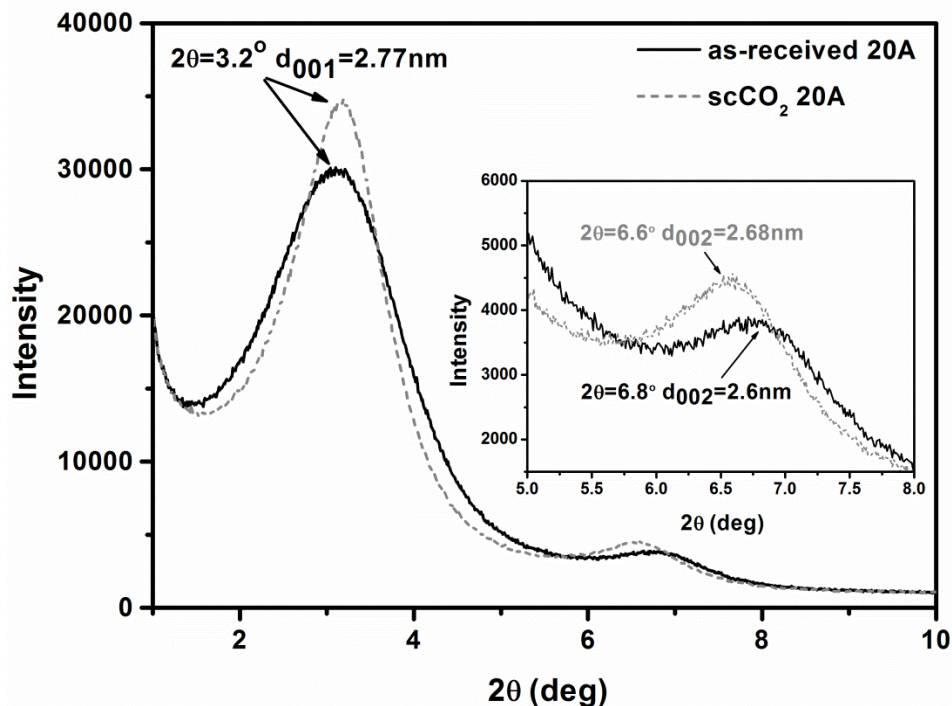
Figure 21 WAXD patterns of as-received and scCO$_2$ processed 20A.

Representative SEM images along a conceptualized cross section were taken to compare the morphological change of clay upon scCO$_2$ processing. As shown in Figure 22, most as-received clay were found in the form of solid particles consisting of a large number of tightly bound tactoids, in which a number of highly ordered stacking platelets held together by van der Waals forces. Upon examination of a large number of SEM images of as-received sample, it was concluded that most of the closely bound particles had a size of 7-24µm and only very few dispersed tactoids were observed. In contrast, the representative images of scCO$_2$ processed clay demonstrated a significant change on morphology. Even though few fraction particles were still found with a lateral size of 3-12 µm, the number of tactoids per particle and the tightness of packing were significantly reduced. Upon depressurization, it appeared that individual tactoids were delaminated from each other leading to a breakdown of particle size. Moreover, a fraction of the

outermost platelets were peeled from the tactoids during CO_2 expansion while the much less mobile inner layers just lost the coherent parallel registry. By measuring the lateral size of tactoids across multiple images (both as-received and $scCO_2$ processed), we also found that although the average particle size had been reduced significantly, the lateral dimension of tactoids remained in the same range (1-3μm), which indicated that $scCO_2$ processing might not affect the aspect ratio of palettes which is a key factor for improving physical properties [26, 30].

Figure 22 SEM images of as-received and $scCO_2$ processed 20A.

TGA (Figure 23) was employed to monitor the thermal decomposition and surficial chemistry change upon $scCO_2$ processing. Both as-received and $scCO_2$ processed 20A showed a three stages weight loss curve in temperature range from 20 to 700 ^{o}C [74]. The first stage was below 100 ^{o}C, which was related with the release of free

water on clay surface or inter gallery space. scCO$_2$ processed clay display less weight loss in this phase might because that free water tend to be trapped in the inter gallery space rather than absorbing on the hydrophobic clay surface. Two separated stages were observed around 310 and 600°C, which were attributed to the decomposition of organic modifiers and decomposition of structural water (reference). scCO$_2$ processed clay demonstrated identical differential curve as the as-received clay. We speculated that although expanded and exfoliated structure of processed clay exposure more modifiers to air, the chemical decomposition of surface modifier on 20A were not highly depended on air. Additionally, no significant difference in weight loss at 700°C after processing was observed, which indicated processing did not remove surface modifiers. The pre-dispersion of the nanoclays could enable significantly better dispersion into the matrix, because the kinetic limitation of clay dispersion no longer is an issue.
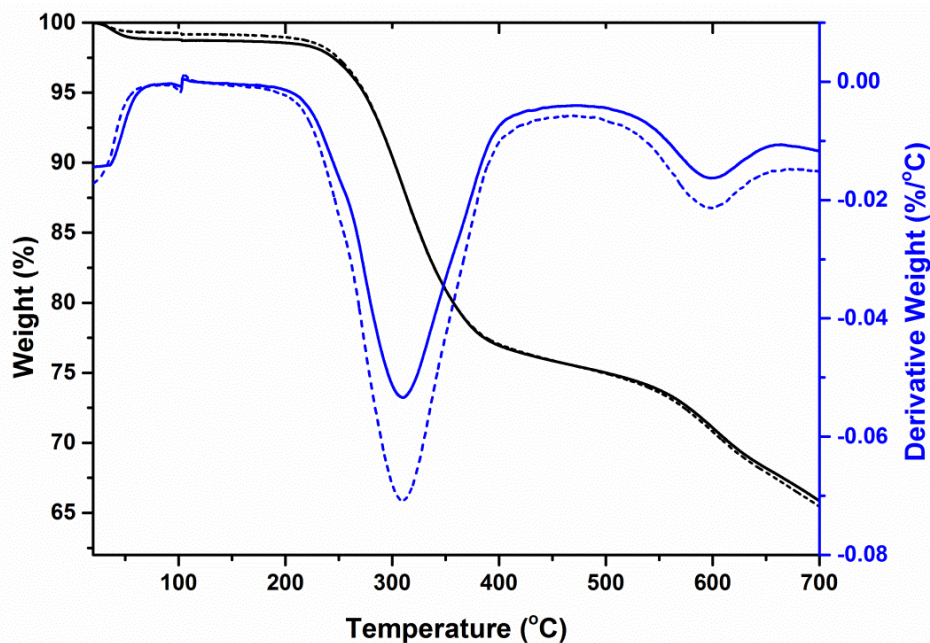
Figure 23 TGA curves of as-received and scCO$_2$ processed 20A.

Furthermore, the 'loose packed' volume and densities of 20A were measured and given in Figure 24. As we can see that the volume (based on 10g) of 20A increased from 17ml to 22.5ml upon scCO$_2$ processing that corresponding to an decrease of density by 24.4%, and the structures of the pre-dispersed clays remained preserved over 6 months storage at room temperature. The pre-dispersion of the nanoclays could enable significantly better dispersion of these clays into the polymer matrix.
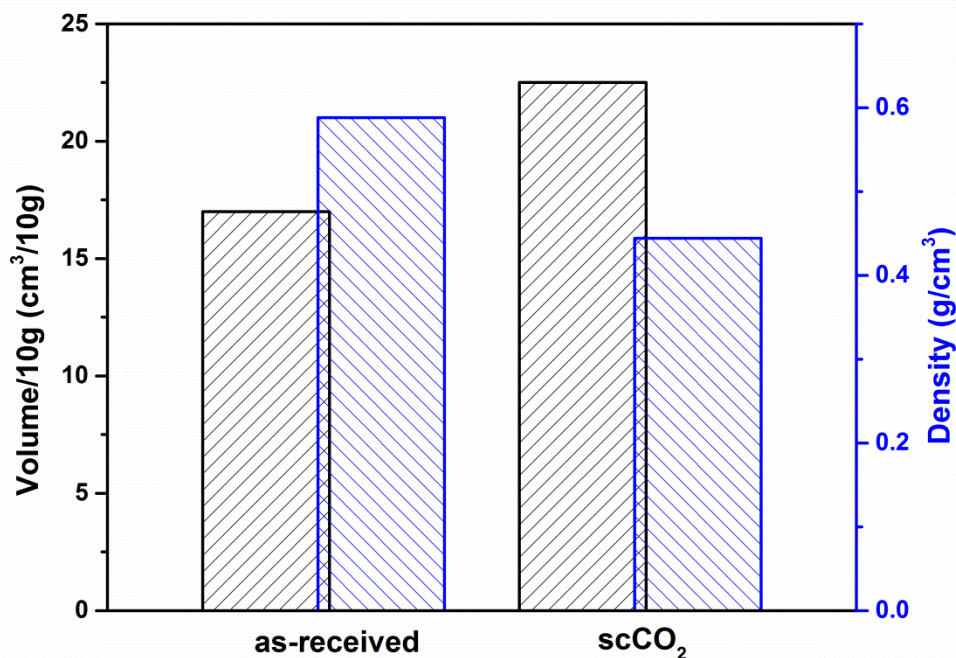
Figure 24 Pack volume/density of as-received and scCO$_2$ processed 20A.

2.3.3 scCO$_2$ processing of Cloisite[®] 30B

The changing of spacing between clay platelets upon scCO$_2$ processing was monitored by WAXD. Based on Figure 25, both as-received and scCO$_2$ processed 30B showed a clear diffraction peak at $2\theta=4.45°$ corresponding to an equilibrium platelet spacing of 1.88nm (basal spacing minus 1 nm for platelet thickness) [89]. In comparison, the scCO$_2$ processed clay displayed a broader peak which indicated a reduction in parallel registry. Moreover, compared with as-received 30B having a d_{002} diffraction peak around

$2\theta=9.2°$ corresponding to a $d_{002}=1.92nm$, scCO$_2$ processed 30B presented a diminished d_{002} peak, which suggested that long range parallel registry between platelets inside tactoids were reduced as a result of scCO$_2$ processing.
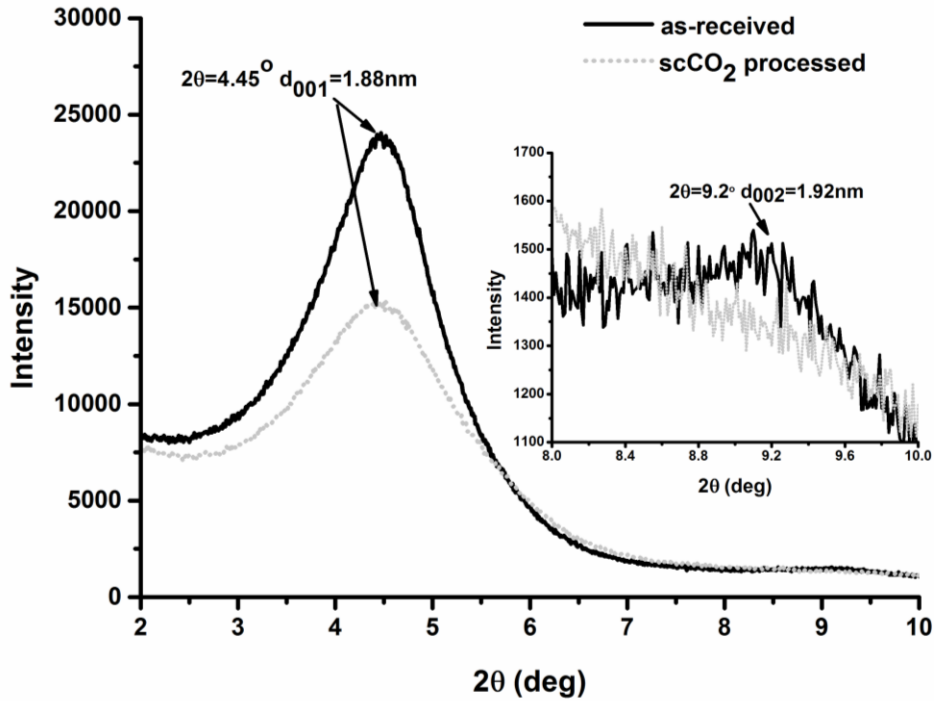
Figure 25 WAXD patterns of as-received and scCO$_2$ processed 30B.

Representative SEM images along a conceptualized cross section were taken to compare the morphological change of clay upon scCO$_2$ processing. As shown in Figure 26, most as-received clay were found in the form of solid particles consisting of a large number of tightly bound tactoids, in which a number of highly ordered stacking platelets held together by van der Waals forces. Upon examination of a large number of SEM images of as-received sample, it was concluded that most of the closely bound particles had a size of 7-24μm and only very few dispersed tactoids were observed. In contrast, the representative images of scCO$_2$ processed clay demonstrated a significant change on morphology. Even though few fraction particles were still found with a lateral size of 3-

15 μm, the number of tactoids per particle and the tightness of packing were significantly reduced. Upon depressurization, it appeared that individual tactoids were delaminated from each other leading to a breakdown of particle size. Moreover, a fraction of the outermost platelets were peeled from the tactoids during CO_2 expansion while the much less mobile inner layers just lost the coherent parallel registry. By measuring the lateral size of tactoids across multiple images (both as-received and $scCO_2$ processed), we also found that although the average particle size had been reduced significantly, the lateral dimension of tactoids remained in the same range, which indicated that $scCO_2$ processing might not affect the aspect ratio of palettes which is a key factor for improving physical properties [26, 30].
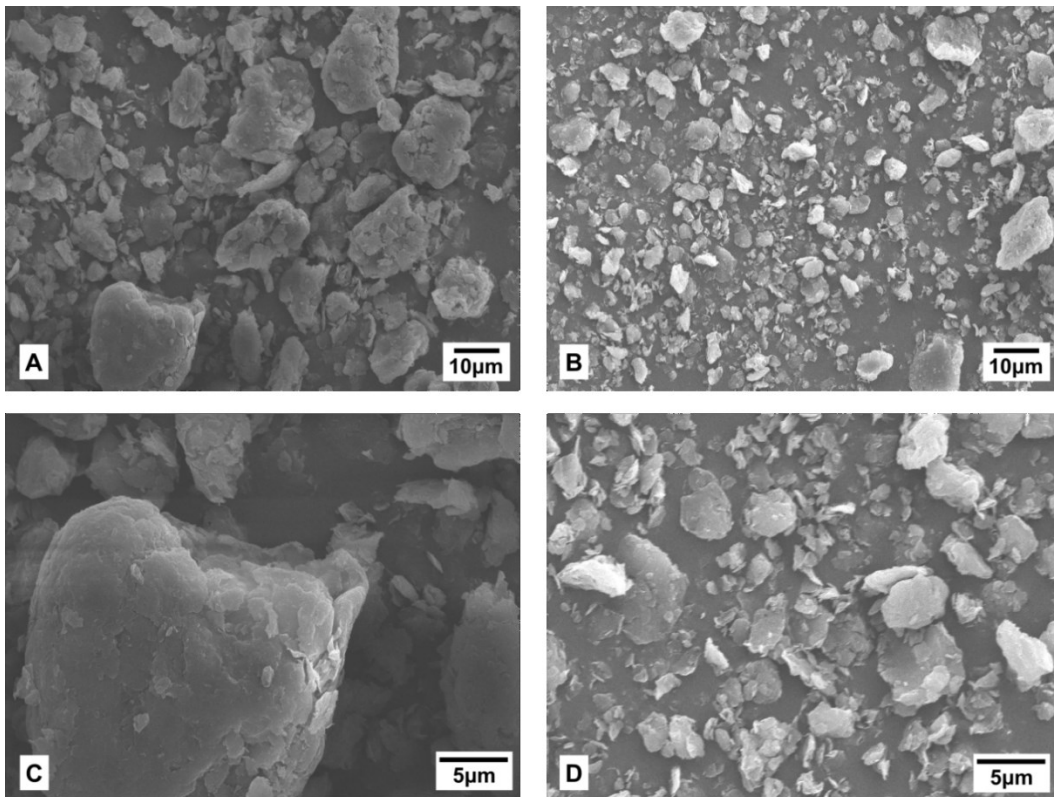
Figure 26 SEM images of as-received and scCO$_2$ processed 30B.

TGA (Figure 27.) was employed to monitor the thermal decomposition and surficial chemistry change upon $scCO_2$ processing. Both as-received and $scCO_2$ processed 30B showed a four stages weight loss curve in temperature range from 20 to 650^oC [74]. The first stage was below 100^oC, which was related with the release of free water on clay surface or inter gallery space. $scCO_2$ processed clay display less weight loss in this phase might because that free water tend to be trapped in the inter gallery space rather than absorbing on the clay surface. Two consecutive stages were observed around 274 and 350^oC, which were attributed to the decomposition of organic modifiers. Finally, the fourth peak showed around 600^oC was expected to be decomposition of structural water (reference). $scCO_2$ processed clay demonstrated a slight shift of the differential curve to lower temperature. We speculated that expanded and exfoliated structure of processed clay exposure more modifiers to air making the decomposition of the modifiers much easier. Additionally, no significant difference in weight loss at 700^oC after processing was observed, which indicated processing did not remove surficial modifiers. The pre-dispersion of the nanoclays could enable significantly better dispersion into the matrix during melting extrusion, because the kinetic limitation of clay dispersion no longer is an issue.
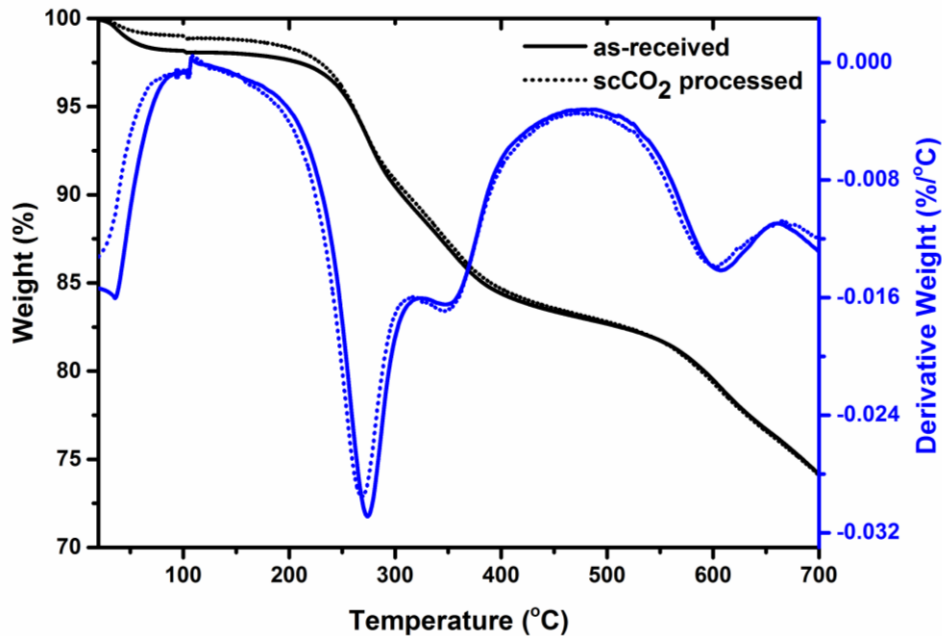
Figure 27 TGA curves of as-received and scCO₂ processed 30B.

Furthermore, the 'loose packed' volume and densities of 30B were measured and given in Figure 28. As we can see that the volume (based on 10g) of 30B increased from 15ml to 25ml upon scCO₂ processing that corresponding to an decrease of density by 40%, and the structures of the pre-dispersed clays remained preserved over 6 months storage at room temperature. The pre-dispersion of the nanoclays could enable significantly better dispersion of these clays into the polymer matrix.
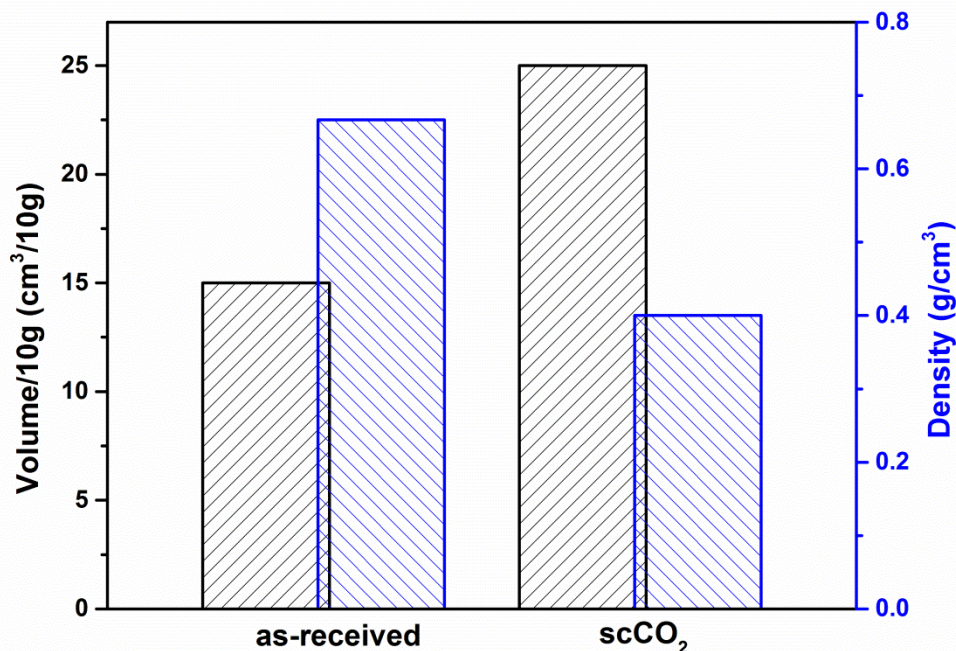
Figure 28 Pack volume/density of as-received and scCO$_2$ processed 30B.

2.4 Conclusion

Based on SEM and WAXD analysis, the novel scCO$_2$ processing method was regarded to be a green, effective and universal method to pre-disperse organic modified clays. Generally, the scCO$_2$ processing result in pre-dispersion of organic modified clays regardless what kind of modifier on them. The degree of dispersion of different kind of clays actually is a competitive result between carbon dioxide-philicity and modifiers interaction, which means stronger carbon dioxide-philicity and weaker modifier interaction result in better pre-dispersion. In addition, TGA data prove that the scCO$_2$ processing did not remove surface modifiers from nano-clays [60] which kept the good solubility of clay in organic solvent and the compatibility to organic phase. Moreover, the loose packed densities of 10A, 20A and 30B have decreased by 23%, 24.4% and 40% respectively, and all properties of the pre-dispersed clay keep unchanged even after 6

56

months storage at room temperature, which indicate that the resultant pre-dispersed clays preserved as-received clay's organic modifier and the expanded structure is thermodynamic stable under room temperature. We believe the expanded flexible and puffy structure of the $scCO_2$ processed clays decreased the average particle size, weakened compact of clay particles and exposed more of the available surface area and should be easier to disperse into a polymer matrix than the as-received clay, moreover the thermodynamic stable structure will make them be easily compatible to many traditional compounding methods such as melting mixing, solution and in-situ polymerization and to overcome kinetic limitation caused by short processing time. In the following two chapters, an easily accessible solution compounding method was used to produce PS/clay nanocomposites and a melting extrusion method was used to fabricate PET/clay and HDPE/clay nanocomposites to provide further evidence to support above assumption.

CHAPTER 3: AMORPHOUS POLYMER/CLAY NANOCOMPOSITES: STRUCTURE AND PROPERTIES

3.1 Introduction

Due to the week inter and intra molecular interactions and irregular steric structure, amorphous polymers show lack of ability to organize into crystals, therefore, no crystallinity is observed in amorphous polymers. Basically, as the temperature increases, the amorphous polymer will soften gradually. The defining temperature for amorphous polymers is the glass transition temperature. Below this temperature, the amorphous chains become immobilized and rigid and behave like glass.

Normally, amorphous polymers experience viscous flow under relatively low temperature which makes them easier to be processed and handled. Moreover, they also have a decreased chance of warping and shrink during processing than semi-crystalline or crystalline plastics, which means they possess comparatively higher free volume than semi-crystalline or crystalline plastics. In other words, amorphous polymers will show relatively poor barrier property than crystalline polymers, assuming the same chemical structure of the repeat units.
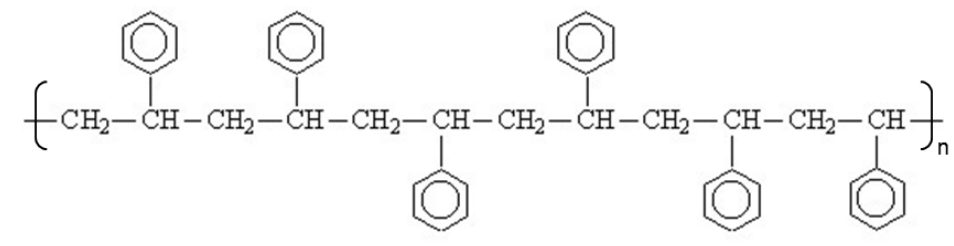
Figure 29 Chemical structure of atactic polystyrene.

In this chapter, atactic polystyrene (Figure 29) which is amorphous was used as matrix and the as-received and pre-dispersed commercial clays as reinforcements to study the effect of clay dispersion, modification and fraction, and $scCO_2$ processing on structural and physical properties of nanocomposites. TEM and WAXD will be employed to study the complex structure of the system. Then, several physical properties will be evaluated and structure-property-application relationship will be set up based on several phenomenological models study. The established relationship will be used as benchmark and guideline for further research.

3.2 Experimental

3.2.1 Materials

Organically modified Cloisite® 10A 20A and 30B, with reported aspect ratios ranging from 10 to 300 [39] were obtained from Southern Clay Products and their composition and physical properties were summarized in Table 1. The atactic polystyrene used has a molecular weight of 260,000 g/mol, density of $1.05g/cm^3$ and solubility parameter of 9.1, was purchased from Scientific Polymer Products, Inc. Toluene (99% purity) used as a solvent was purchased from Alfa Aesar, and was used as received.

3.2.2 Nanocomposites formation

Appropriate amounts of nano-clays, required for the desired final weight fraction (based on 10g polystyrene), were loaded in a 250ml flask, and followed by the addition of 50ml toluene. The clay/toluene solution was vigorously stirred to allow the clay to be homogeneously dispersed into the solvent, after which 10g of polystyrene was added. The solution was vigorously stirred at room temperature for 24h. The mixture was placed in a Teflon plate for 24h to pre-remove the solvent, after that the pre-dried

nanocomposites sheet was put into a vacuum oven at 80°C for 24h to remove residual solvent. Finally, the dry nanocomposites were finely crushed into powder by using pestle and mortar.

3.2.3 Wide-angle X-ray diffraction (WAXD)

A Rigaku Rotaflex Powder Diffractometer with a Cu Kα X-ray source $\lambda = 1.54$ Å (accelerating voltage=44 kV, current=120 mA) was used to assess the clay intergallery spacing. Composite films samples were placed in a custom-made, zero-background quartz sample holder that is 0.9 mm in depth. Several scans were obtained from different locations in the sample and verified to be reproducible when diffraction patterns were superimposed on one another. The 2θ angle was determined using the JADE software that accompanies the diffractometer, and the d_{001} spacing for the clays was calculated using Braggs' Law of diffraction.

3.2.4 Transmission electron microscopy (TEM)

Thin sections (70 nm) of the nanocomposites were prepared using a Leica Ultramicrotome with a diamond knife and placed on 200 mesh copper grids coated with carbon. All samples were examined with a Hitachi H7600 Transmission Electron Microscope operated at 80 kV. Numerous (10-20) images were collected for all samples to ensure accurate representation of the clay morphology and dispersion in the polymer matrix.

3.2.5 Rheology

A Rheometric Scientific RSA II rheometer (shear sandwich geometry 15.98 mm × 12.7 mm × 0.55 mm) was used to perform melt rheological measurements under oscillatory shear. The measurements were made under ambient air at 200 $^{\circ}\text{C}$ for all

samples. Rheology measured before and after annealing at 200°C for 2 h showed no discernible change. Samples were prepared by melt pressing finely crushed pure polystyrene or nanocomposite powder into a mold at 180°C between Kapton films. The materials were loaded and allowed to equilibrate for 15mins at the desired temperature. Strain sweeps were performed to ensure that the dynamic moduli were independent of the strains utilized, and the linear viscoelastic measurements were made at low strains (< 0.10) to minimize microstructure destruction. The frequency range used was 0.01-100 rad/s.

3.2.6 Oxygen permeation

Oxygen transmission rates (OTR) was measured using MOCON OX-TRAN 2/20 instrument at standard mode with 10 cycles and active individual zero. Film samples were prepared by melt pressing finely crushed pure polystyrene or nanocomposite powder into a mold at 180°C between Kapton films and then masked with aluminum foil masks to expose a measurement area of 5cm^{2} and mounted between two chambers at ambient atmospheric pressure. Masks provide support and a uniform area of measurement for small sample sizes. One hundred percent oxygen was continuously admitted at 10 SCCM to the outer chamber and a carrier gas which was a mixture of 98% nitrogen and 2% hydrogen was continuously admitted at 10 SCCM to the inner chamber. As oxygen permeates through the film samples, it was picked up by the carrier gas and carried through an electrochemical oxygen sensor. The environmental test conditions used in the diffusion cells of the instrument were 0% relative humidity and 23 ^{o}C. Finally, obtained OTR was multiplied with average thickness of films to calculate

permeation of oxygen. Duplicate specimens were analyzed for each sample to get an average.

3.2.7 Nonlinear Regression Method

Origin Lab Pro 8 was used to perform all nonlinear regression analysis of the data using the various permeation models, where the inorganic content (in vol %) as the independent variable and the oxygen permeation rate (in cc-mm/m^2-day) as the dependent variable. The fitting procedures used allow for variations in the oxygen permeation of the pure polymer and the aspect ratio of the platelets, but only within physically reasonable bounds. The bounds for pure polymer were 126 to 134cc-mm/m^2-day based on the measured value for pure polystyrene film prepared in the same way as the nanocomposites described here and accounting for the standard deviation of the measurement. For aspect ratio the lower and upper bounds were set to 10 and 300 as mentioned [39], respectively. As it is often assumed in literature, the formation of aggregation would result in a reduction in effective aspect ratio. A Levenberg-Marquardt algorithm was used to adjust the parameters to maximize the fit. All coefficients of determination (r^2) were adjusted to compensate for the number of terms within the models [24].

3.3 Result and discussion

3.3.1 Effects of scCO$_2$ processing and clay modifications on structural, mechanical and barrier properties of PS/clay nanocomposites

WAXD patterns of all of the PS/clay nanocomposites in this study are shown in Figure 30. The nanocomposites exhibited well-defined diffraction peaks regardless of the clays, suggesting the presence of some ordered clay structures after processing. Although

scCO$_2$ processed 10A displayed a broad diffraction peak upon pre-dispersion (figure 17), upon addition to solution it regained some of its parallel registry, as seen before [60]. Both 10A and 20A nanocomposites showed a shift of the d$_{001}$ peak to a lower 2θ compared with pristine clays, 10A nanocomposites display 2θ=2.4° corresponding to an increase of inter gallery spacing from 1.05 to 2.68 nm. 20A nanocomposites presented a peak at 2θ=2.4°, corresponding to an increase of inter gallery spacing from 1.77 to 2.68 nm, suggesting that polymer had been intercalated into the clay galleries. Although scCO$_2$ processed clay did not show further shift of the diffraction peak, the decrease of intensity might indicate a decrease of ordered structure inside those composites. Conversely, 30B nanocomposites showed significantly different diffraction peaks compared to as-received and scCO$_2$ processed clays. Finally, for scCO$_2$ processed clays, the presence of polymer in the solution may deter reorganization of clay platelets, resulting in a composite with a bimodal population of small ordered tactoids and dispersed platelets pairs. WAXD is not sensitive to dispersed platelets and therefore may not be representative of the true dispersion state of the system.
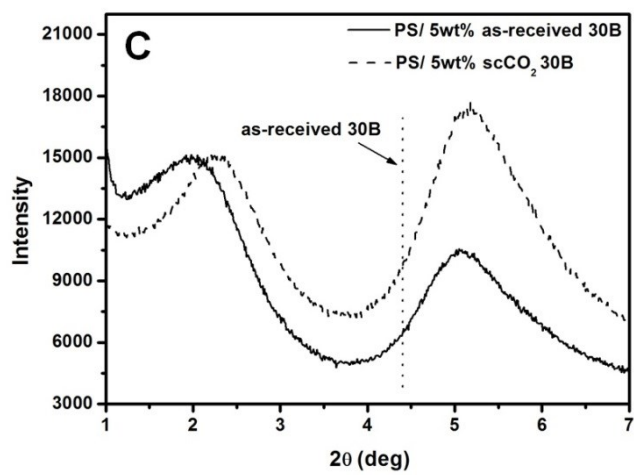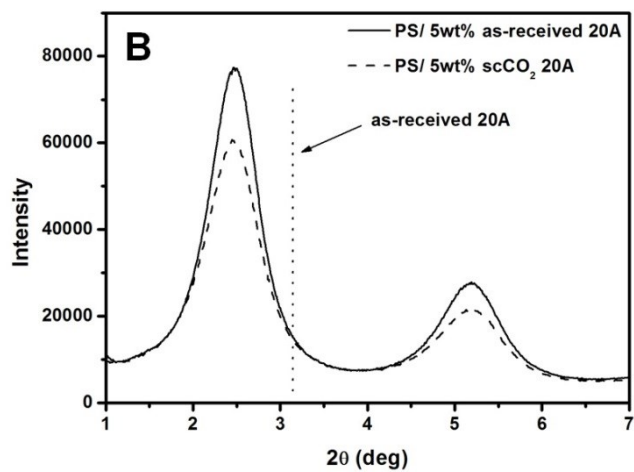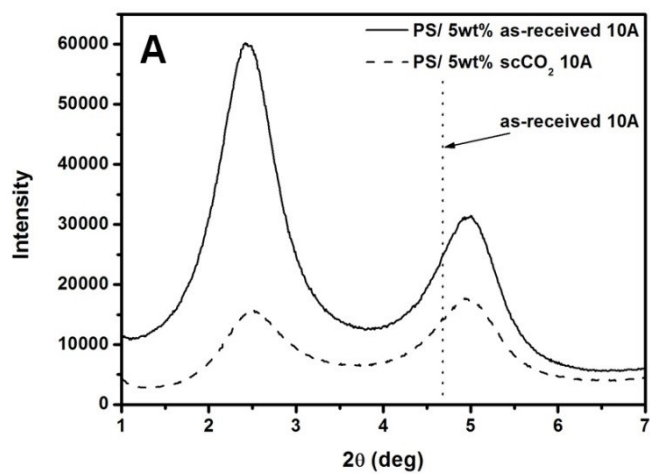
Figure 30 WAXD patterns of PS/5wt% clay (A) 10A, (B) 20A and (C) 30B nanocomposites.

Electron microscopy was used to complement X-ray diffraction studies. With the sub nanometer resolution limit of the TEM, individual platelets and tactoids can be directly visualized. Figure 31 presents representative low magnification TEM images of all nanocomposites in this study. Among the as-received clay-nanocomposites, 20A presented the best dispersion where no obvious aggregations were observed, 10A showed moderate aggregation (highlighted by black circles), whereas serious aggregation was observed in 30B. This was consistent with the results of a coarse-grained molecular dynamics simulation done by Liu et al., who suggested that by tuning the polymer filler interaction in a wide range at both low and high filler loadings, homogeneous filler dispersion exists just at the intermediate interfacial interaction which is in contrast with traditional viewpoints. Strong or weak particles-polymer interactions both could lead to aggregation, due to an entropic depletion effect or local bridging of filler via polymer chains [111]. The $scCO_2$ reinforced nanocomposites showed improved clay dispersion in all cases. The fraction of big tactoids decreased, and the partial interface between the polymer and $scCO_2$-processed clay become diffuse compared with the clear and sharp boundaries between polymer and as-received clays. This will be discussed later.
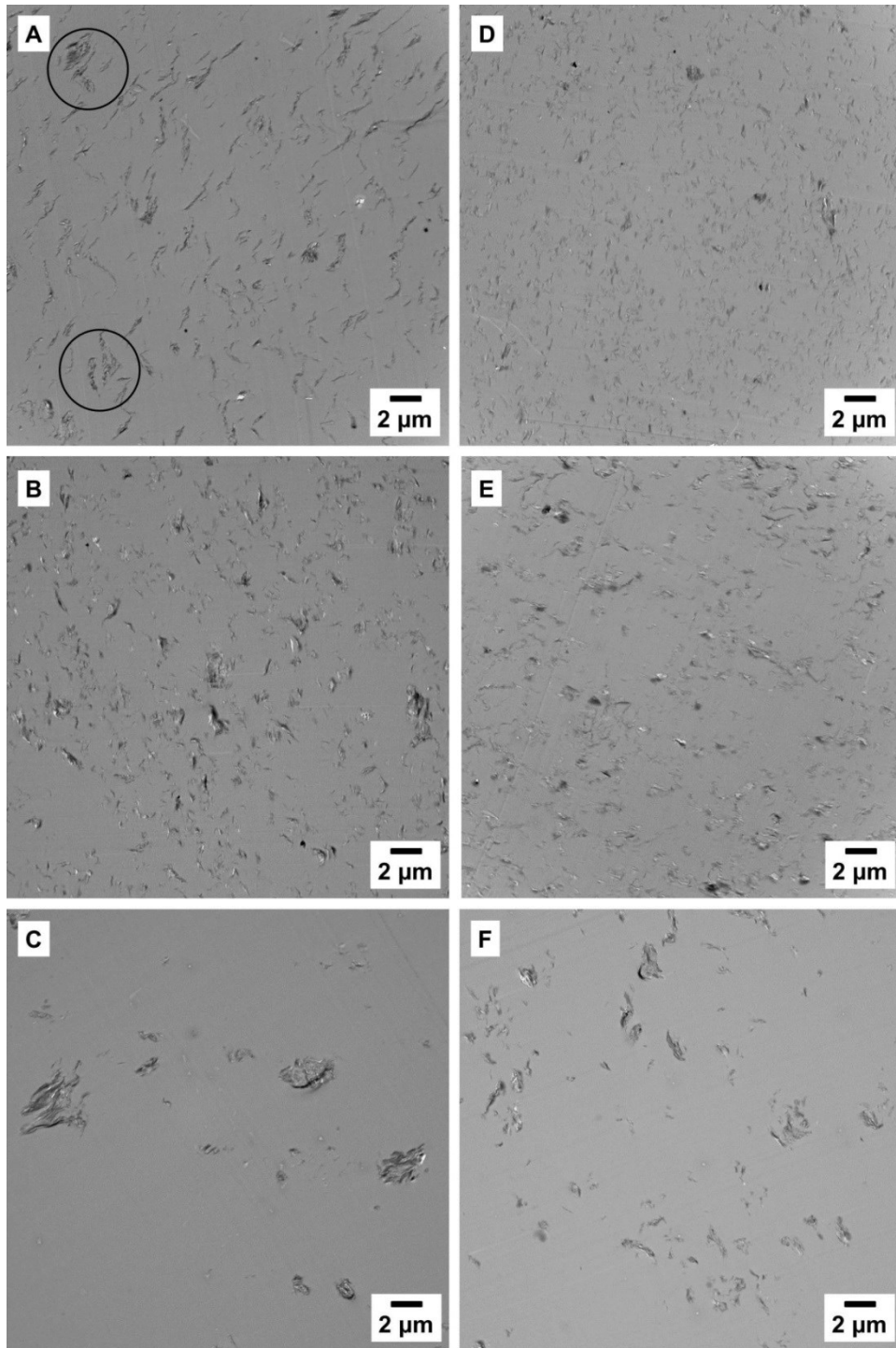
Figure 31 TEM images of PS/ 5wt% as-received clay (A) 10A, (B) 20A and (C) 30B nanocomposites. And TEM images of PS/ 5wt% scCO$_2$-processed clay (D) 10A, (E) 20A and (F) 30B nanocomposites.

High magnification images of PS/ clay nanocomposites revealed more insights into the dispersion and interface between matrix and filler (Figure 32). Upon investigation of many images, highly ordered and stacked tactoids are observed in all of PS/ as-received clay nanocomposites. In contrast, a large number of 'single' platelets could be seen in both $scCO_2$ processed 10A and 20A composites. Moreover the size of tactoids decreased in both $scCO_2$ processed composites; and more ordered tactoids could be seen in $scCO_2$-20A composites rather than $scCO_2$-10A composites. Although a statistical average size of tactoids is hard to measure due to irregular shapes, these observations support the change in X-ray diffraction patterns with various types of clays upon $scCO_2$ processing. In addition, changes of interface futures are observed through $scCO_2$ processing. Nanocomposites with as-received clay displayed clear and sharp interfaces, moreover, non-wetting surfaces are observed (highlighted by black arrow). In contrast, more obscure and diffusive boundaries were found (highlighted by white arrow) after $scCO_2$ processing indicating an improved polymer-clay interaction. For PS/ 30B nanocomposites, the $scCO_2$ processing did not produce significantly dispersed structure of clays, even though significant break down of tactoids was observed corresponding to an increase of aspect ratio. In addition, with $scCO_2$ processed clays, more homogeneous dispersion was seen [60, 85]. By examining numerous images of nanocomposites, the lateral dimension of single platelets was in the range from 100 to 150nm. Considering the thickness of the clay platelet (1 nm) this suggests an aspect ratio of 100-150 in the processed clays. The aspect ratio of platelets has been shown to be an important factor for improving barrier property of nanocomposites [24, 30].
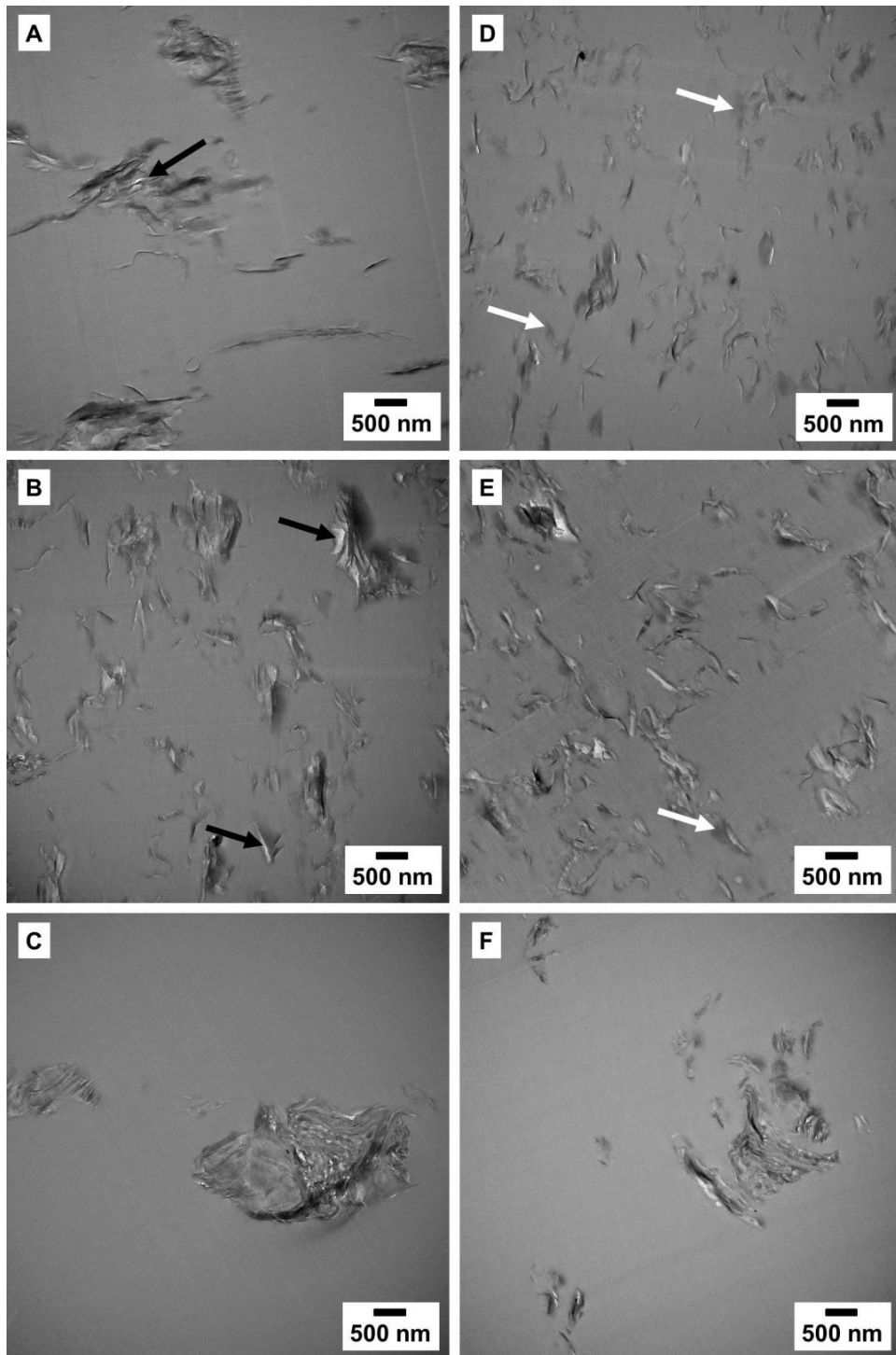
Figure 32 TEM images of PS/ as-received clay nano composites (A) 5 wt% 10A, (B) 5 wt% 20A and (C) 5 wt% 30B. And TEM images of PS/scCO$_2$ processed clay nano composites (D) 5 wt% 10A, (E) 5 wt% 20A and (F) 5 wt% 30B.

Rheology is sensitive to clay dispersion and polymer-clay interactions. In this section, we study the effect of different clays on the rheological behavior of the different nanocomposites melts. The storage modulus (G') and complex viscosity (η^*) of the nanocomposites melts with different clays are compared in figure 33 and 34, respectively. Typically, it has been shown that when the nanoclays are highly dispersed, a plateau in the storage modulus, G', versus frequency is observed at low frequencies. However, Nguyen et al. reported that the plateau could be a result of networks formed due to strong interaction between modifiers and matrix or large agglomerates of clays formed due to very high clay loading [90]. In our case, the loadings of clays are relatively low in all cases. Therefore, the observed low-frequency plateau was attributed to a network of polymer-clay, where both clay dispersion and polymer-clay interactions play very important roles. Figure 33 suggests that 30B-reinforced nanocomposites had no improvements of storage modulus when compared with pure PS, however 10A and 20A nanocomposites showed plateau at low frequency, and 10A nanocomposites showed better improvements than 20A nanocomposites. Even though TEM images suggested that 20A was better dispersed than 10A, the modulus improvements within low frequency range were better for 10A, indicating that polymer-clay interactions may be playing an important factor for rheology the same as clay dispersion does [89]. The complex viscosity (Figure 34) increased in all nanocomposites compared to the based polymer, with higher increases in clays with stronger matrix interactions. We note that the as-received 30B-PS nanocomposite showed slightly higher complex viscosity than $scCO_2$ processed 30B nanocomposite. We speculate that this may be due to the large agglomerates of clays which block the movements of matrix polymer chains, whereas the

improved dispersion of scCO₂ processed 30B made polymer chains movement easier. Rheology suggests that PS/10A nanocomposites had the strongest interface and scCO₂ processed improved clays dispersion, which are consistent with what we have observed in TEM images.
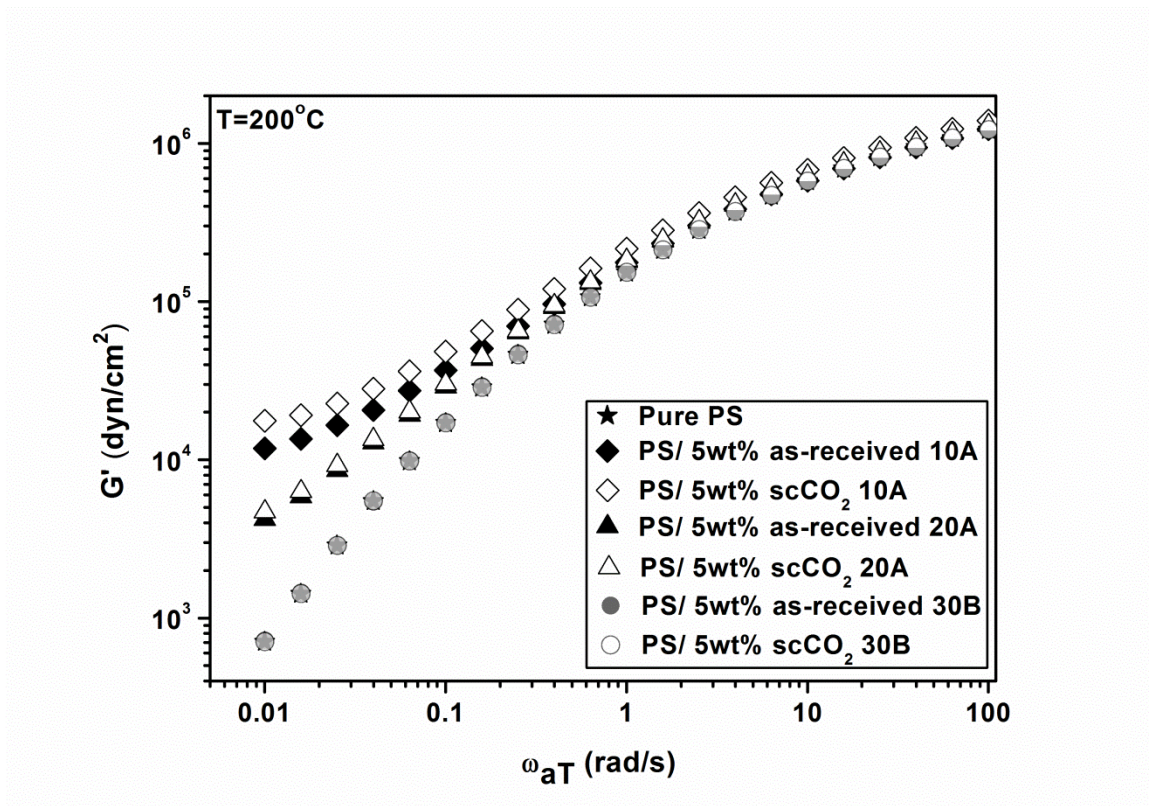
Figure 33 Storage modulus of pure PS and PS/ 5wt% clay nanocomposites.
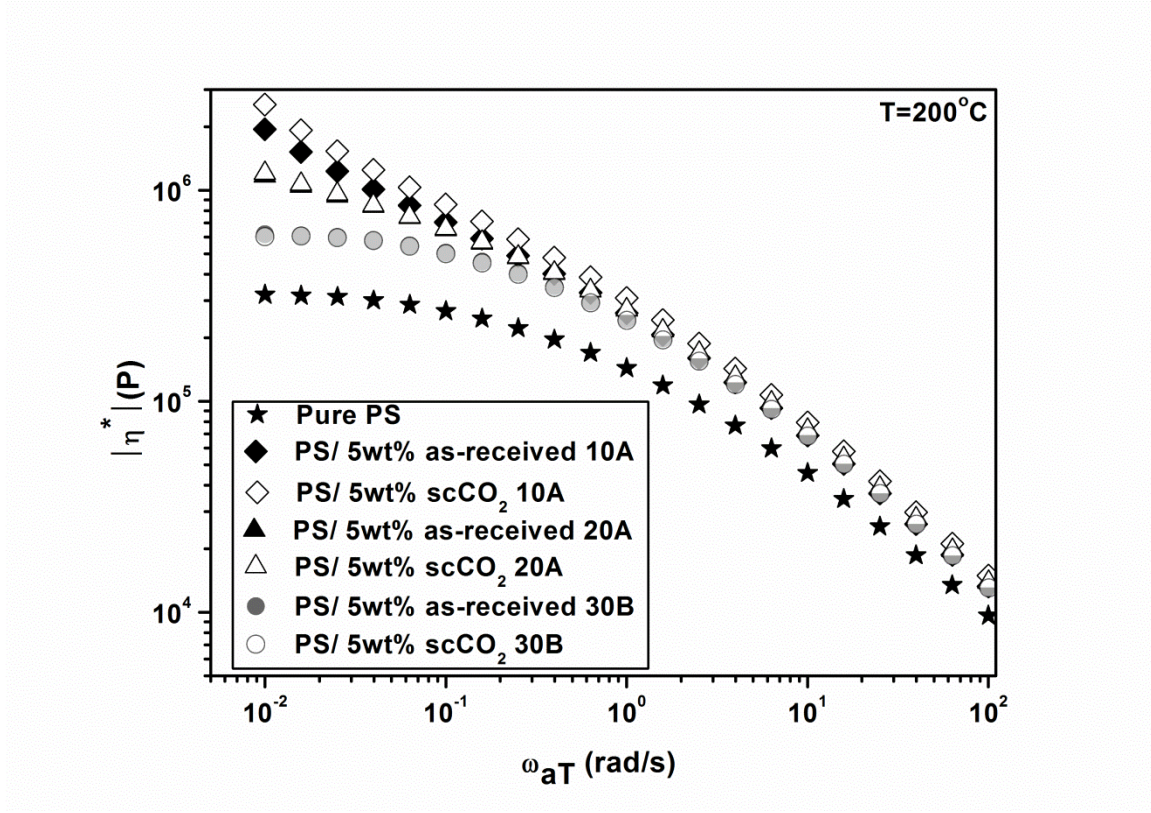
Figure 34 Complex viscosity of pure PS and PS/ 5wt% clay nanocomposites.

Gas permeation has also been shown to be sensitive to the dispersion of filler and the polymer-clay interface. Figure 35 shows the permeations of oxygen of pure polymer and clays reinforced composites, all composites show a decrease of permeation of oxygen compared with pure polymer, even the as-received 30B reinforced composites show a 14.6% decrease of permeation. Although PS/20A nanocomposites appeared to show better dispersion than PS/10A composites, PS/10A composites showed better barrier property improvements at the same weight fraction. When comparing all of scCO$_2$-processed clay reinforced composites with as-received clay composites, the scCO2 processing led to further improvements in barrier properties. The scCO$_2$ 30B, 20A and 10A composites showed a decrease in permeation of 29.4%, 38% and 48.6%

respectively. Although scCO$_2$ processing resulted in best improvement in 30B barrier, scCO$_2$-processed 10A lead to a significant reduction (~49%) of permeation with only a 1.09% volume fraction of inorganic clay (detailed calculation of volume fraction will be given in following section).
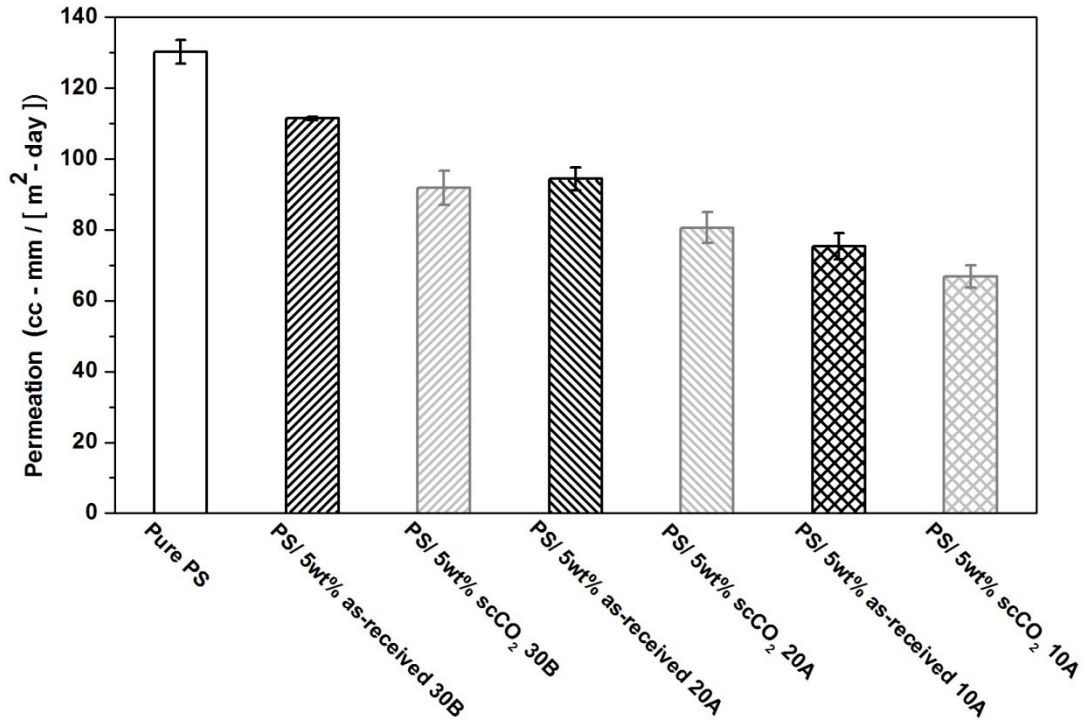
Figure 35 Oxygen permeations of pure PS and PS/ 5wt% clay nanocomposites.

When clay layers are dispersed in polymer films, a penetrant has to bypass clay layers and move through amorphous region of polymer, result in a decrease in permeability. Therefore, the detour ratio, can be defined as the ratio of the film thickness d, in nominal diffusion flow direction, to the average length of the diffusion tortuous distance between silicate layers for the permeability reduction [17]. Based on these ideas, different phenomenological models have been used to predict gas permeation properties of polymer/clay nanocomposites. One of the first barrier membrane models was that of Nielsen [31]. This classic model assumes that the ordered array of barrier

layers consist of ribbons contained within the polymer matrix. The ribbons have a width w, thickness t, and infinite length and are assumed to be perfectly dispersed and aligned in the polymer matrix. Based on the analysis of detours, they reported the relative permeation in the following equation:

$$R_P = \frac{P}{P_0} = \frac{1 - \phi_V}{1 + \frac{\alpha \phi_V}{2}}$$

Where R_p is relative permeation, P and P_0 are permeations of composites and pure polymer respectively, ϕ_V is volume fraction of inorganic clay and α is the aspect ratio of inorganic clay. Cussler and coworkers proposed phenomenological models to better predict gas permeation of polymer/clay nanocomposites [32, 112], using a random array of clay ribbons contained within the polymer matrix, suggesting the equation below [113]:

$$R_P = \frac{P}{P_0} = \frac{1 - \phi_V}{1 + \frac{2\alpha \phi_V}{3} + \frac{(\alpha \phi_V)^2}{9}}$$

Where, all of the parameters have the same physical meanings as previous Nielsen model. In our study, the volume fraction of inorganic clay inside composites can be calculated from:

$$\phi_V = \frac{\phi_W \times (1 - W_{WLI}) / \rho_C}{\phi_W / \rho_{OC} + 1 / \rho_P}$$

Where ρ_{OC}, ρ_C and ρ_P are the density of organic clay, inorganic clay and polymer matrix, ϕ_W is weight fraction of organic clay and W_{WLI} is weight loss of organic clay on ignition. The relative permeation and inorganic clay volume fraction are calculated and given in Table 2. The experimental relative permeation in this research will be substitute

73

into the mentioned models to calculate the effective aspect ratio, and the effects of $scCO_2$

process and polymer-clay interaction on effective aspect ratio will be discussed.
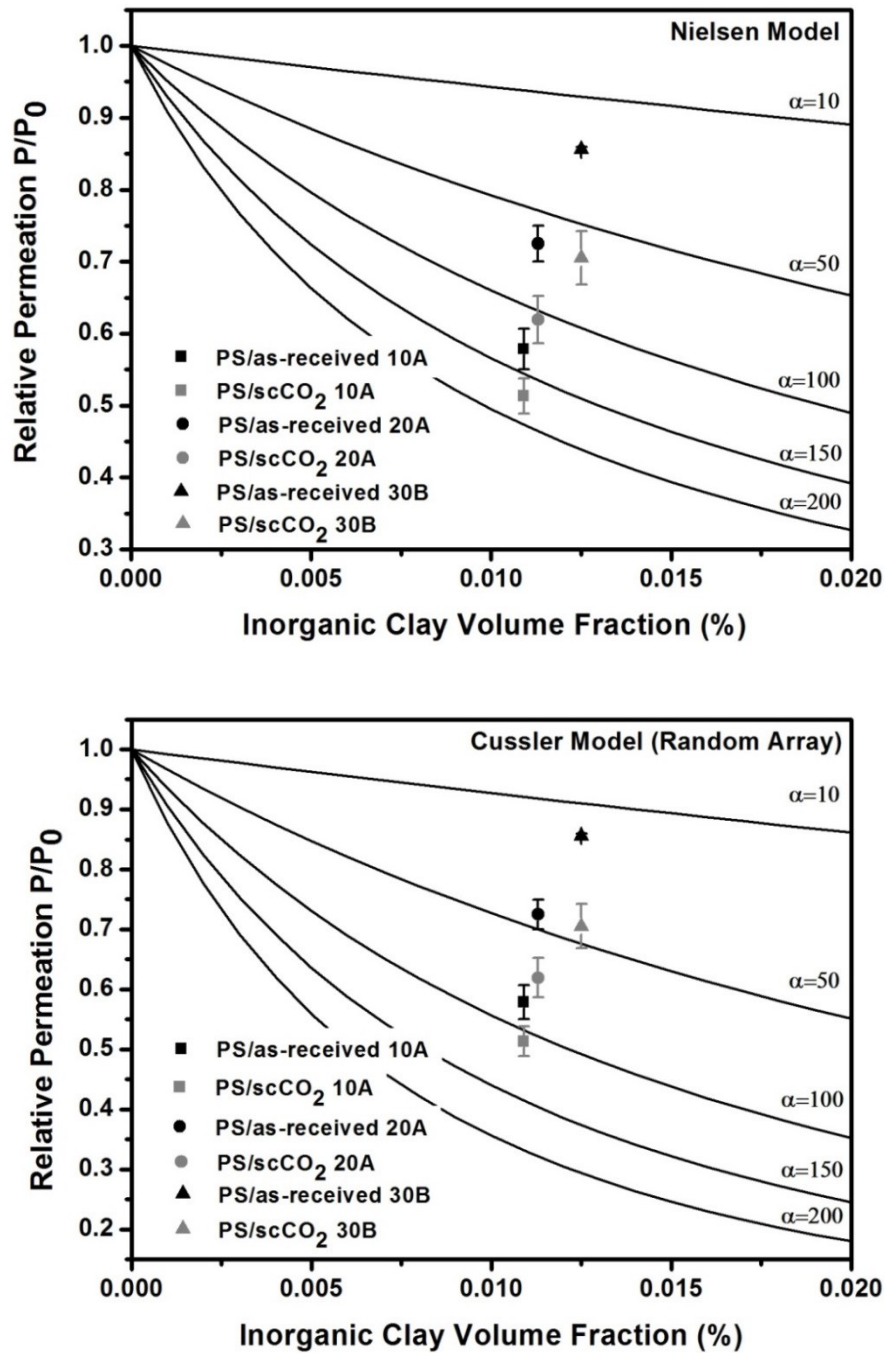
Figure 36 Relative permeation versus inorganic clay volume fraction with different aspect ratios: (Top) Nielson Model; (Bottom) Cussler Model (model predictions and experimental data).

Figure 36 presents theoretical relationship between relative permeation and volume fraction of inorganic clay based on Nielsen and Cussler models. Both models show a decrease of relative permeation with increase of inorganic clay volume fraction or aspect ratio. The experimental data were also given in figure 36, where all of $scCO_2$-processed samples showed further decrease of relative permeation when compared with as-received samples, which correspond to an increase of the effective aspect ratio of clay. The experimental relative permeations were substituted into Nielsen and Cussler models to calculate the corresponding effective aspect ratio which were summarized in Table 2. The calculated effective aspect ratios of clay fall into ranges from 20 to 200 (Nielson) and 10 to 150 (Cussler). The maximum calculated effective aspect ratio is 170.1 in $scCO_2$ processed 10A samples based on Nielsen model where corresponding calculated effective aspect ratio based on Cussler models is 106.8. The TEM images of the $scCO_2$ processed platelets suggested a lateral dimension between 100 to 150nm corresponding to an aspect ratio of 100-150 (the thickness of single layer is 1nm), whereas aggregation or poor polymer-clay interaction could led to a decrease in effective aspect ratio. Accordingly, Cussler's random array model may be a more realistic phenomenological model for those nanocomposites systems.

Table 2 Volume faction of inorganic clay, relative permeation and calculated effective aspect ratios of different PS/clays nanocomposites. The clay volume fractions are the inorganic fractions, excluding the organic modifier content. The standard deviation in relative permeation is based on 4-5 measurements for each value.

Samples	clay (vol%)	Relative permeation	Calculated aspect ratio from Nielsen Model	Calculated aspect ratio from Cussler Model
Pure PS	-	1±0.03	-	-
PS/ 5wt% as-received 10A	1.09	0.58±0.03	130.2	84.7
PS/ 5wt% scCO$_2$ 10A	1.09	0.51±0.03	170.1	106.8
PS/ 5wt% as-received 20A	1.13	0.73±0.03	65.6	45.4
PS/ 5wt% scCO$_2$ 20A	1.13	0.62±0.03	107.5	71.2
PS/ 5wt% as-received 30B	1.25	0.86±0.003	24.6	17.8
PS/ 5wt% scCO$_2$ 30B	1.25	0.71±0.04	64.0	44.0

3.3.2 Effects of scCO$_2$ processing and composition on structural, mechanical and barrier properties of PS/clay nanocomposites
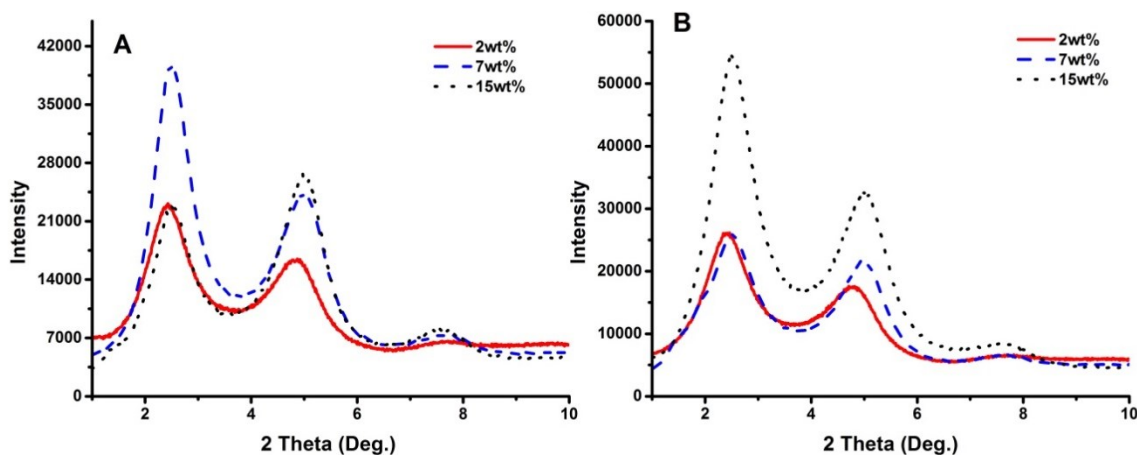
Figure 37 WAXD patterns of PS/10A nanocomposites with different clay type and fraction (A) as-received clay, (B) scCO$_2$ processed clay.

WAXD patterns of the PS/10A nanocomposites are shown in Figure 37. All of nanocomposites exhibited distinct diffraction peaks regardless of variations on clay type and fraction indicating all nanocomposites still contain some highly ordered clay structures. Although $scCO_2$ processed 10A illustrated significantly broadening and shift of diffraction peak (figure 17), upon addition to solution it regained some of its parallel registry. Similar phenomena had been observed by Manitiu et al. [60]. All of nanocomposites showed similar shift of the d_{001} peak to lower 2θ compared with pristine clay, where nanocomposites displayed $2\theta=2.4°$ corresponding to an increase of inter gallery spacing from 1.05 to 2.68 nm, suggesting that polymer had been intercalated into the clay galleries, nevertheless $scCO_2$ processed clay did not lead further expansion of d-space. Interestingly, 15wt% as-received 10A reinforced nanocomposites demonstrated a relatively stronger d_{002} peak than d_{001} peak, whereas, $scCO_2$ processed clay did not. V. A. Richard et al. previously modeled the intercalation behavior of clay in the presence of polymer and pointed out there was an entropic compensation that matrix polymer do not want to be confined between the platelets; and for typical polymers, motion was restricted even when occupying the maximum space between platelets [66]. Dunkerley et al. observed an decrease of interlayer spacing in the polymer-starved samples, which indicated exclusion of polymer chains from intercalation structure due to strong inter platelets interaction during reorganization [24]; nevertheless, the improved spatial distribution of $scCO_2$ processed clay may suppress inter platelets interaction and prevent expelling of polymer chain.
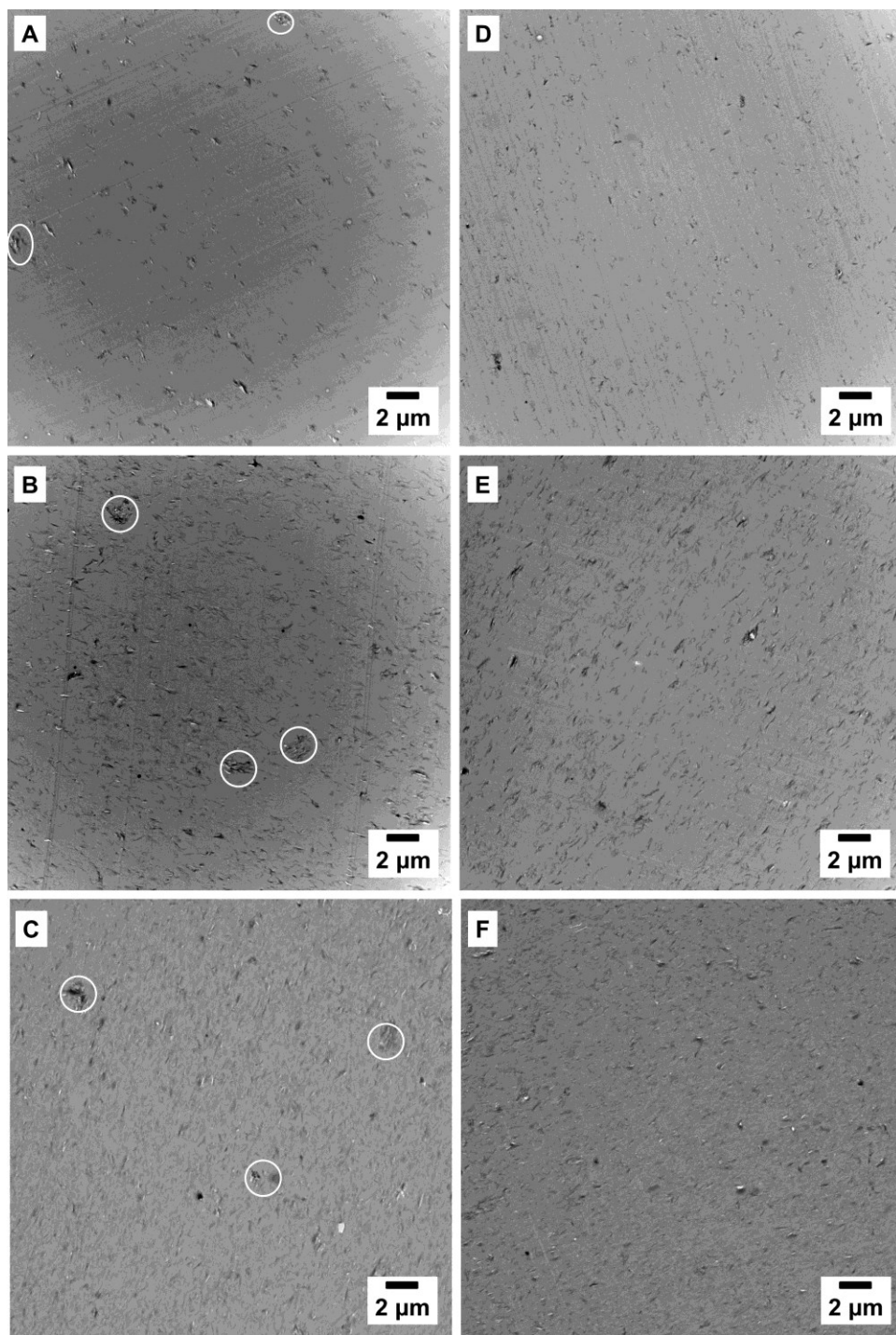
Figure 38 TEM images of PS/10A nanocomposites with different clay loadings 2wt% (A and D), 7wt% (B and E), and 15wt% (C and F) at 5000× magnification, left column is as-received clay and right column is scCO$_2$ processed clay.

Transmission electron microscopy was used as a technique to complement X-ray diffraction data to better visualize the spatial dispersion and morphology of the nano-clay in the nanocomposites. With the sub-nanometer resolution limit of the TEM, individual tactoids and platelets can be directly visualized. Figure 38 presents representative TEM images of nanocomposites without/with $scCO_2$ processing and different clay fractions at 5000× magnification. The relatively low magnification allowed us mapping spatial clay dispersion in a relatively large area making it more accurate. By comparing TEM images with different clay fractions, the tactoids number in per unit area increases proportionally as a function of clay fraction, meanwhile, when compared with as-received clay, $scCO_2$ processed clay displayed significant increase of tactoids density. Moreover, partially large agglomerates of tactoids (highlighted by white circle) were observed in all as-received clay reinforced nanocomposites but not presenting in $scCO_2$ processed samples. We attributed those agglomerates coming from two possible sources: firstly, those preserved tightly bounded particles which had been observed in SEM images of as-received clay, secondly, the re-aggregations between highly ordered tactoids due to strong interaction. The existences of those large agglomerates could cause unfavorable heterogamous clay dispersion and significantly decreased the effective aspect ratio, which in turn rendering poor improvement in physical properties [47].
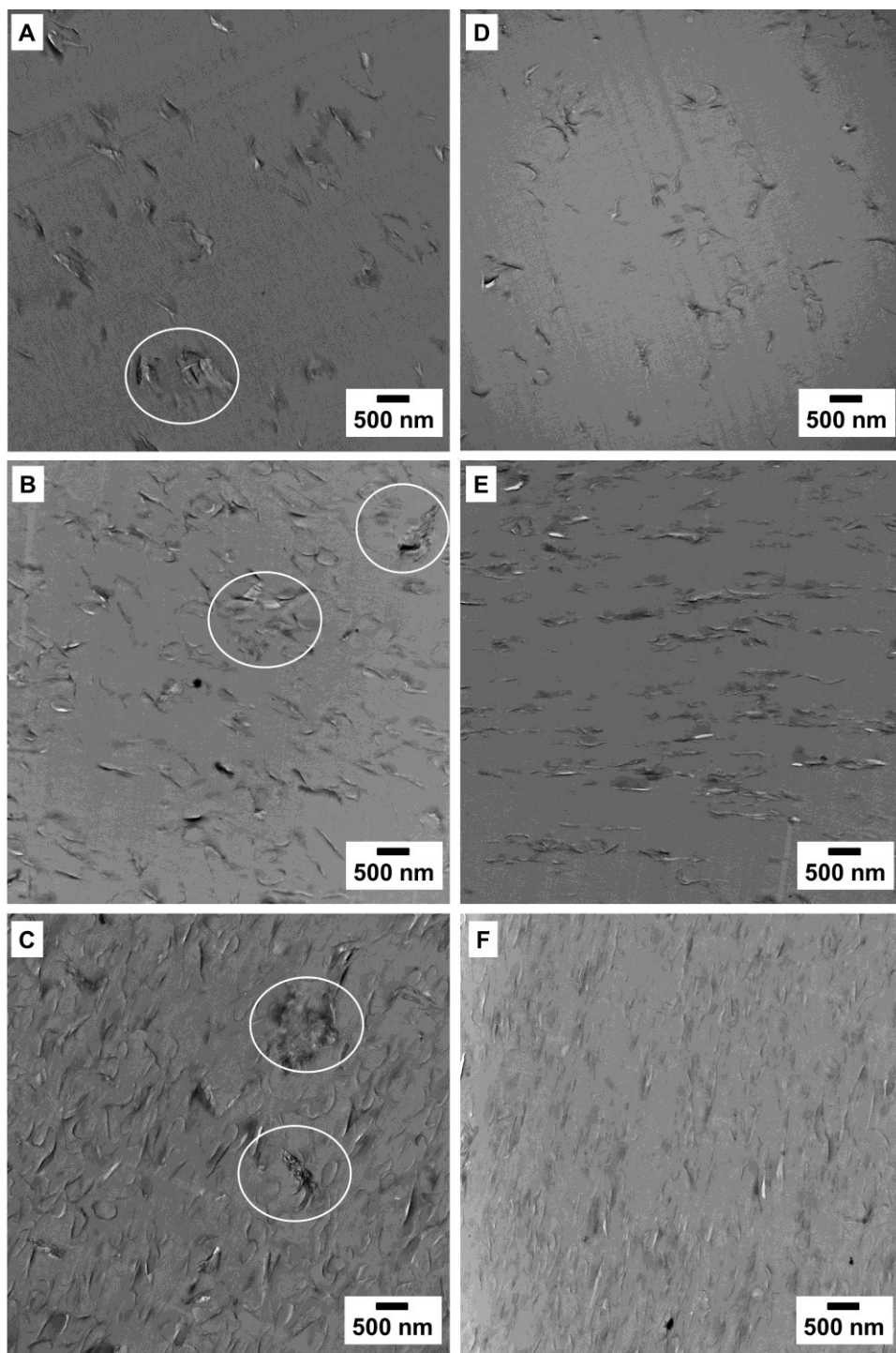
Figure 39 TEM images of PS/10A nanocomposites with different clay loadings 2wt% (A and D), 7wt% (B and E), and 15wt% (C and F) at 20000× magnification, left column is as-received clay and right column is scCO₂ processed clay.

Figure 39 zoomed in (20000×) all nanocomposites to reveal more details of clay dispersion and morphology. Tightly packed particles with transversal dimension over 300nm (highlighted by white circle) were observed in all as-received clay samples. Researchers identified those large agglomerates as one single particle which dramatically decreased the effective aspect ratio [1, 47]. On the other hand, $scCO_2$ processed samples illustrated relatively homogenous dispersion of clay particles with thinner transversal width, nevertheless, a statistical average aspect ratio of tactoids was hard to be measured due to their irregular shapes. Those observations were highly consistent with what we have seen in SEM images. During $scCO_2$ processing, tightly bundled particles were broken down to expose more surface area making them more easily be dispersed in matrix. In additions, various interfacial zone features were observed for samples before-after $scCO_2$ processing. Nanocomposites with as-received clay displayed clear and sharp interface, conversely, more obscure and diffusive boundaries were found for $scCO_2$ processed clay. We speculated the changes arisen from both improved dispersion and polymer-clay interaction.
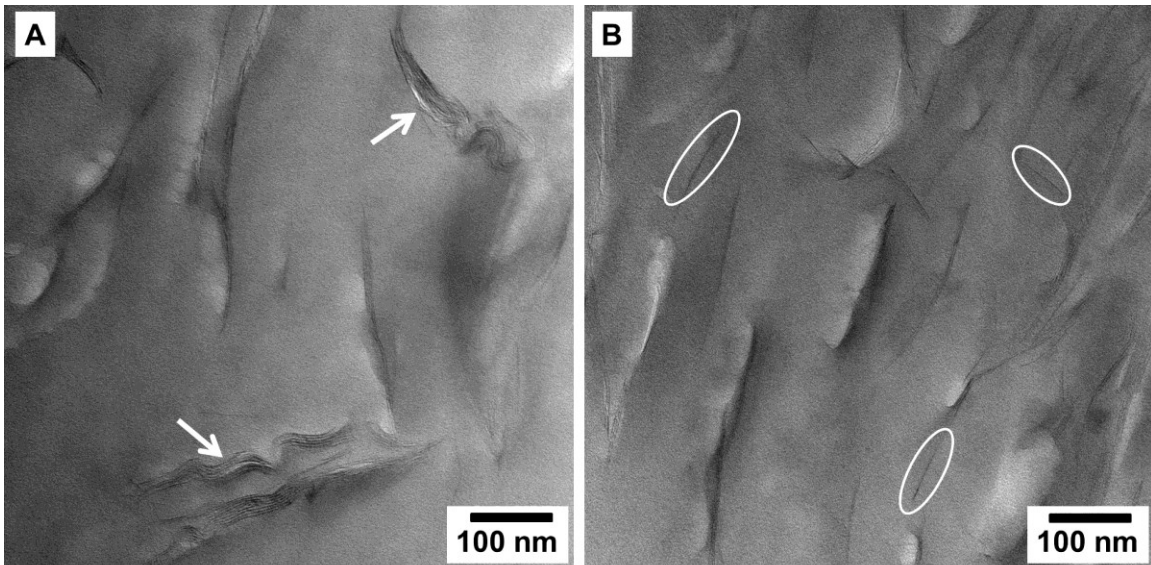
Figure 40 TEM images of PS/ 15wt% as-received (A), scCO₂ processed (B) 10A nanocomposites at 200000× magnification.

Figure 40 focused to a sub-nanometer resolution level to visualize detail morphology of the platelets and interface in nanocompsoites. More fractions of exfoliated single platelets (highlighted by white circle) were observed in scCO$_2$ processed sample, in contrast, closely stacked tactoids presented in as-received clay samples (highlighted by white arrow). Interactions between phenyl group of 10A and polystyrene could be favorable; therefore, the increase of interfacial surface can directly translate to improved physical properties [10]. In addition, the aspect ratio of platelet is an important factor for improving physical property of nanocomposites. By examining numerous images, both as-received and scCO$_2$ processed samples showed similar lateral dimension of single platelet which is around 100 to 150nm. With the knowing thickness of platelet to be 1nm [1], the aspect ratio of platelet is about 100 to 150. However, inhomogeneous dispersion and serious stacking could decrease the effective aspect ratio. Based on above

structural study, we believed that scCO$_2$ processing produced a more homogeneous dispersion with more intimate interfaces.

Rheology is an effective tool to quantify the improvements in mechanical response that result from attempting to maximize clay dispersion and/or interactions [89]. In this section, we investigated the effects of clay fraction and scCO$_2$ processing on the rheological behavior of different nanocomposites melts. The storage modulus, G' and complex viscosity, η* of the nanocomposites melts were compared in figure 41 and 42, respectively. It was generally reported that when the nano-clays were exfoliated to form a network due to either strong polymer-clay or clay-clay interaction, a plateau in the storage modulus versus angular frequency presented at low frequencies [60, 90, 114]. In our work, the dynamic frequency scan measurements successfully picked up the morphology differences by revealing significant dependency of the plateau at low frequency on clay fraction and dispersion. Similar results were reported by Jin Zhao et al., they concluded that pure polystyrene and nanocomposites with low fraction of clay particles gave typical terminal relaxation behavior (G'~ω^2) as pure polymer. With the level of dispersion increased, spectrum showed more solid like behavior, especially at low frequencies, indicating a percolated network structure [114]. As shown in Figure 41, storage modulus at low frequency increased dramatically as increase of clay fraction. With 2wt% clay, nanocomposites expressed similar relaxation behavior as pure polymer. As the clay fraction increased to 7wt%, a solid like response at low frequency were achieved, indicating passing the percolation of forming network structure. Further increase of clay fraction, nanocomposites exhibited a 3 order of magnitude improvement of storage modules with nearly independent response behavior on frequency. This

observation was highly consistent with TEM images observation. In the nanocomposites with clay loading of 2wt%, the viscosities were slightly higher than that of pure PS at low frequency and decreases sharply with the increase of the frequency to reach a value equal to that of pure PS. This indicates a fluid rather than filler dominating fluid dynamics. The nanocomposites with higher clay loading than 2wt% were orders of magnitude more viscous than that of the pure PS at lower frequency and exhibited stronger shear thinning behavior. As the clay loading exceeded 7wt%, the viscosities of nanocomposites were higher than that of pure PS in whole frequency range.
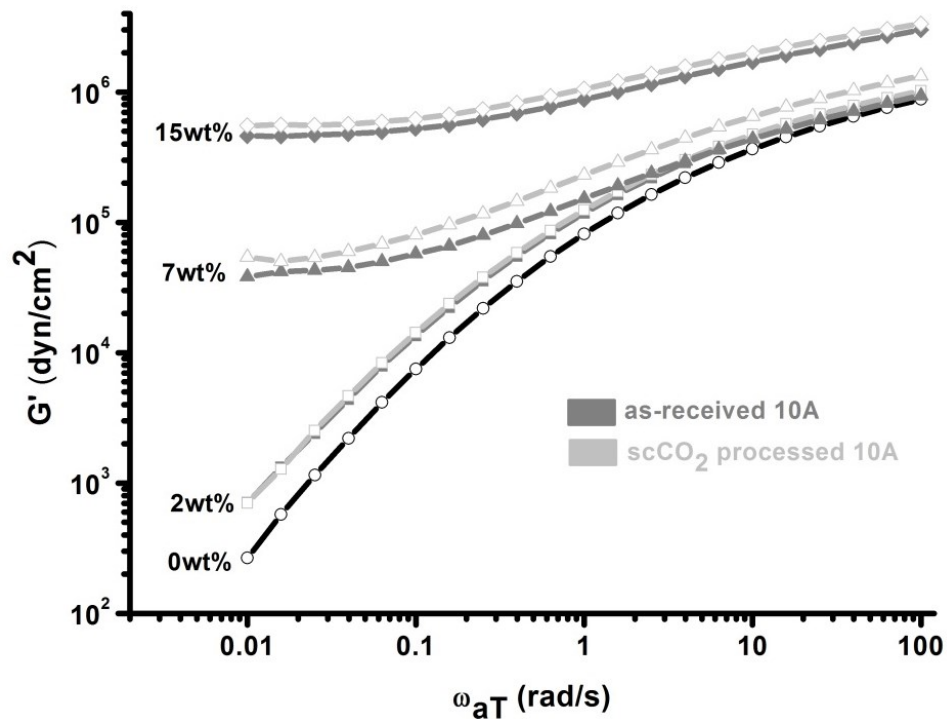
Figure 41 Storage modulus of PS and PS/10A nanocomposites with different clay type and fraction.
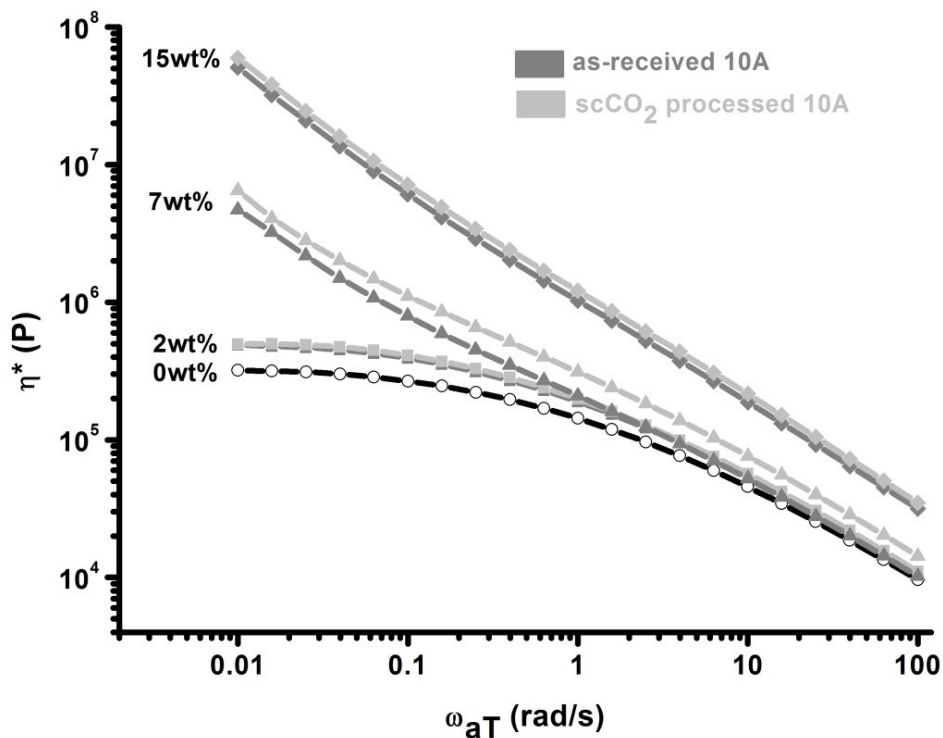
Figure 42 Complex viscosity of PS and PS/10A nanocomposites with different clay type and fraction.

Since the interactions between the 10A and polystyrene could be favorable and scCO$_2$ processing did not remove modifiers from the clay surface, improved exfoliated dispersion should further improve the interaction in the network structure. However, as can be seen in Figure 41 and 42, the scCO$_2$ processing only had slightly improvement on the nanocomposites rheological behavior with relative higher clay loading. Repeated rheological measurements on the same sample prepared multiple times proved that storage modulus and complex viscosity were accurate to about 5-10% [12]. The storage modulus and viscosity of the 2wt% samples with/without scCO$_2$ processing overlapped with each other right within experimental error. Nevertheless, with 7wt% and 15wt% clay fractions, the magnitude of storage modules at low frequency (ω=0.025) increased by 25.4% and 18.7% respectively. The facts confirmed the recognized standpoint that

terminal relaxation behavior is highly sensitive to formation of network structure with a threshold limitation, in another word, low clay loading may be failed to exceed the threshold even with dispersed clays. In addition, further increase of viscosity with improved dispersion quality by further exfoliation of clay through $scCO_2$ processing were observed both at 7wt% and 15wt% clay loading samples, and were attributed to the further increased confinement/block of polymer chains. We also speculate that even though improved dispersion is helpful for passing threshold limitation to form network structure, the exfoliated single platelets maybe build weaker bridge to transfer stress between matrix and filler when compared with the intercalated clay particles, which could be the reason that $scCO_2$ processing improved nanocomposites rheological behavior more prominent at moderate clay loading.
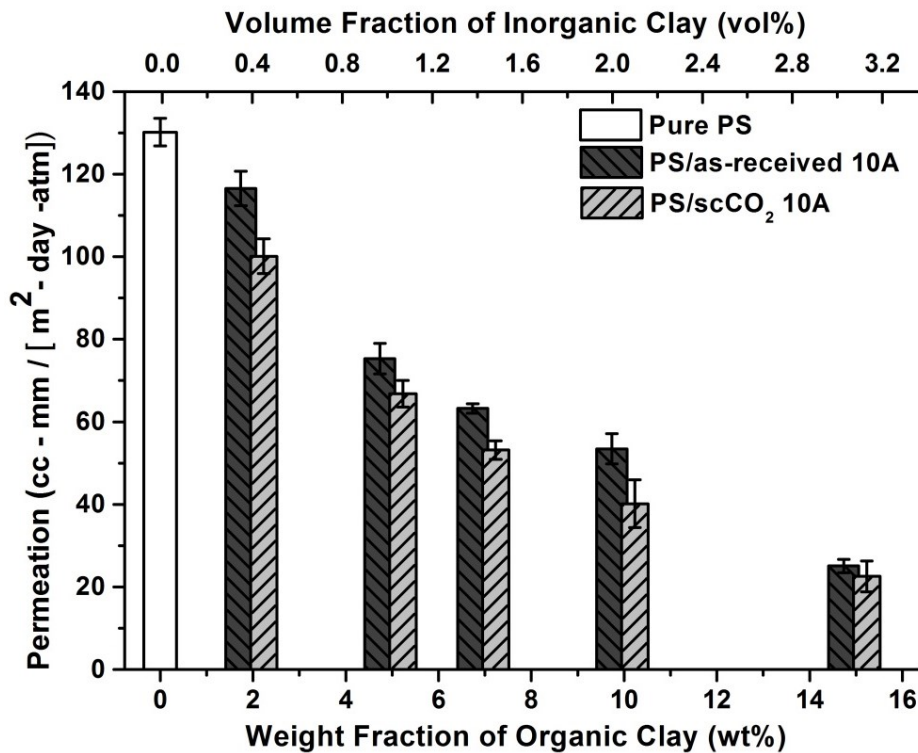
Figure 43 Oxygen permeations of PS and PS/ 10A nanocomposites with different clay type and fraction.

Figure 43 presents the oxygen permeations of pure polymer and clay reinforced nanocomposites as function of clay fraction, where the volume fraction was calculated based on weight fraction and the detail calculation will be discussed in the following section. The Oxygen permeation for the pure PS used in this work was measured to be ~130cc • mm/(m^2 • day • atm), similar to the literature value of 166cc • mm/(m^2 • day • atm) [115] with the discrepancy aroused from different resin grade. Permeation data reported here demonstrated that nanoclay with high aspect ratio could produce substantial improvements in barrier properties over the full studied range. As shown in Figure 43, adding nanoclay resulted an exponential reduction in oxygen permeation, with ~83% of magnitude decreases achieved by 15wt% of $scCO_2$ processed 10A.

Table 3 Calculated inorganic clay volume fraction, relative permeation and corresponding decrease for different nanocomposites with/without $scCO_2$ processing.

Organic clay weight fraction (wt%)	Calculated inorganic clay volume fraction (vol%)	Relative permeation		
		as-received	$scCO_2$	Decrease (%)
2	0.44	0.91±0.04	0.77±0.04	15.2
5	1.09	0.58±0.04	0.51±0.05	11.3
7	1.51	0.49±0.01	0.41±0.02	16.0
10	2.12	0.41±0.03	0.31±0.04	24.9
15	3.1	0.19±0.01	0.17±0.03	10.0

The inorganic clay volume fraction, relative permeation and corresponding decrease for $scCO_2$ processed samples compared with as-received samples were calculated and given in table 3. The data indicated that with help of $scCO_2$ processing,

nanocomposites achieve further decrease of permeation (10-24%) compared with corresponding as-received clay sample. Although there are ample evidences that the interphase will act differently than the bulk polymer in terms of its relaxation temperature, the analysis temperature of $23^{o}C$ is below any thermal transitions in the materials. In terms of overall segmental mobility, then, we can say that all organic components are below their lowest measurable thermal transition temperatures for the purposes of permeation analysis [21]. So we speculated the further decrease of oxygen permeation was mainly aroused by improved dispersion and interfacial interaction.

Mathematical models based on a number of approaches are often used to describe permeation in nanocomposites. The simplest are the series and parallel coupling rule of-mixtures approaches, which represented the upper and lower bounds in terms of barrier properties but are not applicable to materials containing discrete clay particles [116]. The next level of models relevant to nanocomposites systems take into consideration of discrete clay particles with particular cross-sectional geometry, spatial distributions and orientation. Such approaches describe the clay as either ribbons or flakes. And when clay platelets are dispersed in the polymer, a penetrant has to bypass clay platelets and moves through amorphous polymeric region, result in a decrease in permeability. Thereby, usually researches consider the factor of the detour ratio which can be defined as the ratio of the film thickness d, in nominal diffusion flow direction to average length of the diffusion tortuous distance between silicate layers for the permeability reduction. Based on the ideas, different phenomenological models have been used to predict gas permeation properties of polymer/clay nanocomposite. As mentioned previously, method,

assumption, formula and tortuosity factor applied by Nielsen [31], Cussler [32, 112], Fredrickson and Bicerano [33], and Gusev and Lusti [34] are summarized in table 4. In general, gas permeation in nanocomposites is given by the following equation [17],

$$\frac{P_0}{P}(1-\varphi_V)=1+\tau$$

Where P_0 and P are gas permeation of pure matrix and nanocomposites respectively. ϕ_V is volume fraction of inorganic clay, τ is the tortuosity factor which is phenomenologically calculated as a function of both volume fraction of inorganic clay and aspect ratio of the clay particle. In our study, the volume fraction of inorganic clay of composites can be calculated from:

$$\phi_V = \frac{\phi_W \times (1-W_{WLI})/\rho_C}{\phi_W/\rho_{OC}+1/\rho_P}$$

Where ρ_{OC}, ρ_C and ρ_P are the density of organic clay, inorganic clay and polymer matrix, ϕ_W is weight fraction of organic clay and W_{WLI} is weight loss of organic clay on ignition which for Cloisite 10A is 0.39 [44]. The experimental permeation data in this research were fit into the mentioned models to reveal the relationship between structure and barrier properties [24, 30].

Table 4 Published method, assumption, formula and tortuosity factor for various phenomenological models.

Model	Filler Type	Array/orientation (Cross-section)		Dimension	Aspect ratio	Original Formula	Tortuosity Factor
Nielsen	Ribbon	Regular array, oriented		2D	w/t	$\frac{P_0}{P}(1-\phi)=1+\frac{\alpha\phi}{2}$	$\tau=\frac{\alpha\phi}{2}$
Cussler (Regular array)	Ribbon	Regular array, oriented		2D	w/t	$\frac{P_0}{P}(1-\phi)=1+\frac{(\alpha\phi)^2}{2}$	$\tau=\frac{(\alpha\phi)^2}{2}$
Cussler (Random array)	Ribbon	Random array, oriented		2D	w/t	$\frac{P_0}{P}(1-\phi)=1+\frac{2\alpha\phi}{3}+\frac{(\alpha\phi)^2}{9}$	$\tau=\frac{2\alpha\phi}{3}+\frac{(\alpha\phi)^2}{9}$
Gusev and Lusti	Disk	Random array, oriented		3D	d/t	$\frac{P_0}{P}(1-\phi)=e^{\left(\frac{\alpha\phi}{3.47}\right)^{0.71}}$	$\tau=e^{\left(\frac{\alpha\phi}{3.47}\right)^{0.71}}-1$
Fredrickson and Bicerano	Disk	Random array, oriented		3D	d/t	$\frac{P_0}{P}(1-\phi)=4\left[\frac{(1+\chi+0.1245\chi^2)}{2+\chi}\right]^2$ where $\chi=\pi\alpha\phi/2\ln(\alpha/2)$	$\tau=\left[\frac{-1.01(2\chi+3)}{(\chi+2)^2+0.062\chi^2+0.748\chi+0.756}\right]$

The results of the application of these models to our experimental data are shown in Figure 44. Interestingly, most of models were able to match the data over at least part of the composition range explored here, except for the Cussler's regular array model which does not account for variations in particle spacing [32], nevertheless, Nielsen model also ignores the variations, and it still fits the data very well. Compared with scCO$_2$ processed samples, as-received samples displayed more discrepancies with the theoretical value. A summary of calculated r^2, P$_0$ and effective aspect ratio for different nanocomposites based different models were given in table 5. Nearly in all applied models, scCO$_2$ processed samples demonstrated better fitting than as-received sample, among these models, Cussler's random array model illustrated the best fitting to scCO$_2$ processed sample with r^2=0.9959. Although as-received sample displayed better fitting value by using Cussler's Regular array model, we emphasized the calculated value was invalid due to the intrinsic unrealistic assumption of the model as we have mentioned above, therefore, for the following discussion we would like to skip this model. With a close exanimating of all calculated P$_0$ values, we found the calculated value for as-received clay always approached the boundary limitations for pure polymer which was set to be between 126 to 134cc • mm/(m^2 • day • atm) based on the measured value, in contrast, all of scCO$_2$ samples presented valid values within physically reasonable bounds. Since the difference between bulk and interface matrix are ignorable, one likely reason for the discrepancies observed in as-received samples is their heterogeneous clay dispersion which have been confirmed by TEM images where unevenly distributed large agglomerates lead to local to local variations.
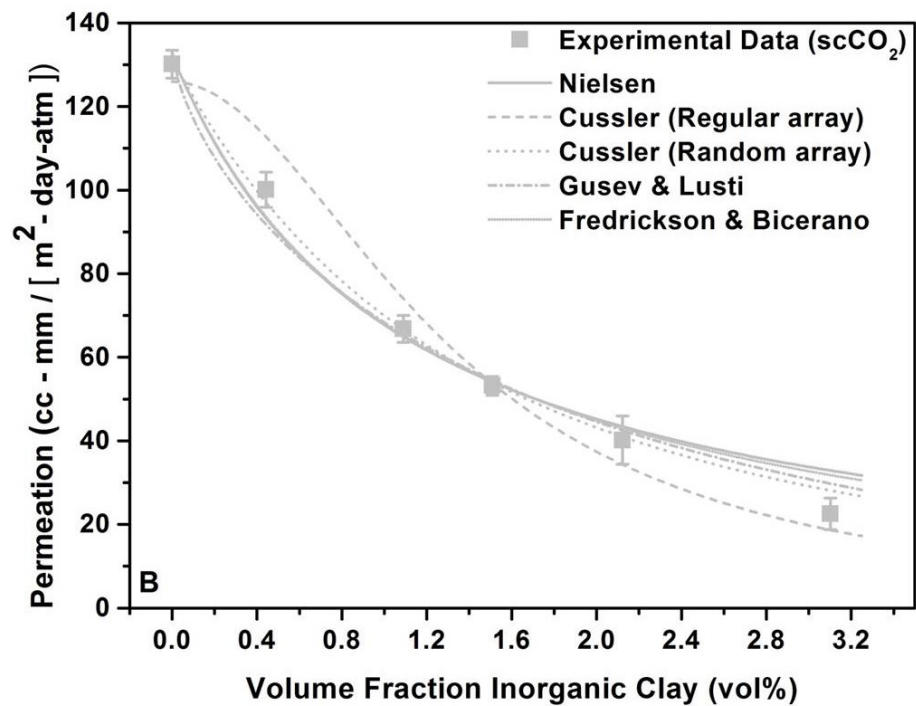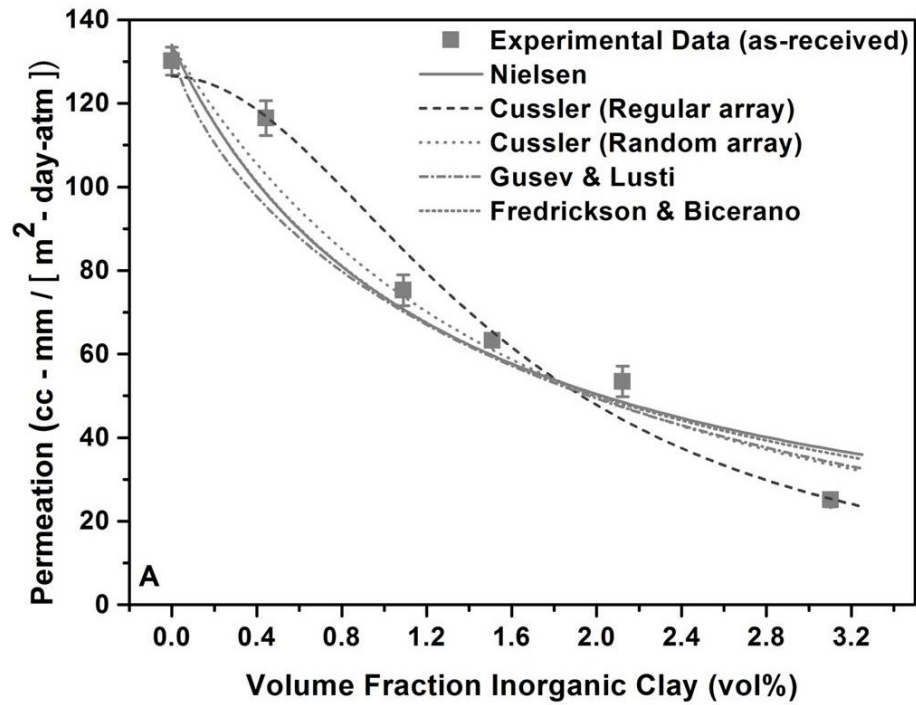
Figure 44 Permeation vs inorganic clay volume fraction (A) as-received clay and (B) scCO₂ processed clay (Both modeling and experimental data).

Beside the more homogenous clay dispersion, $scCO_2$ processing increased the effective aspect ratio. As seen from table 5, all models presented increases of calculated effective aspect ratio by 14-20% for $scCO_2$ sample with respect to as-received sample. Clearly, stacked layered structure decreased the effective aspect ratio which have been reported by other researchers [106]. In addition, the absolutely calculated effective aspect ratio varied from 89 to 293, however, as we have observed in TEM images, the aspect ratio for platelets should be around 100 to 150, therefore, Cussler's random array model probably is more valid and gives more realistic phenomenological fitting for those complex systems with an calculated effective aspect ratio of 109 for $scCO_2$ processed clay, which is the largest effective aspect ratio had been reported so far [24].

Table 5 Calculated r^2, P_0 and effective aspect ratios for different nanocomposites based different models.

Model	r^2		P_0		α		
	as-received	scCO$_2$	as-received	scCO$_2$	as-received	scCO$_2$	Increase (%)
Nielsen	0.91	0.98	134±14.5	132.4±5.1	160.5±37.4	186.8±20.0	16.4
Cussler (Regular array)	0.98	0.96	126.6±5.6	126±6.1	89.3±5.0	107.3±8.4	20.1
Cussler (Random array)	0.95	0.99	134±9.7	131.5±2.2	93.5±12.3	109.1±4.4	16.7
Gusev and Lusti	0.92	0.98	134±12.8	133.2±4.4	168.1±31.8	191.8±16.3	14.1
Fredrickson and Bicerano	0.91	0.98	134±13.6	132.5±4.6	243.7±66.2	293.1±34.0	20.3

3.3.3 Discussion

As we can see from the results, it seems a limited improvement of dispersion, rheological and barrier property is observed, as compared with that of composites obtained by adding as-received clay. However, detailed analysis showed that for the dispersion, it is clearly showed in our WAXD that the fraction of particles with long range ordered structure has been significantly decreased and TEM images illustrated that upon $scCO_2$ processing, the density of particle per unit area increased, especially for the case of 10A, and based on our statistical analysis, the particle density increased by over 200%. For the rheological test, the storage modulus of PS/as-received 10A (5wt%) at frequency of 0.01rad/s is 19000 dyn/cm^2 while the corresponding value for as-received 10A is about 15000 dyn/cm^2, here we got a 26.7% of increase. For the permeation, compared with as-received clay, all of the $scCO_2$ processed clay showed improvement on barrier property, especially in the term of effective aspect ratio, the increases are in the range of 26-147%. In addition, our relative improvements in permeation with respect to as-received clay are comparable to those published data for improving barrier properties by using sonication in solution blending [23] or additives in melting extrusion [95].

From experimental aspect, we believe the potential reason for us only getting so-called 'limited' improvement of dispersion, and rheological and barrier property is that in this work we applied solution blending method to prepare nanocomposites. During the solvent removal phase, the pre-dispersed clay may reorganize platelets into order structure which has been reported by M. Manitiu et al [60]. In this way, our $scCO_2$ pre-dispersion effect was offset by the easily kinetic reconstruction.
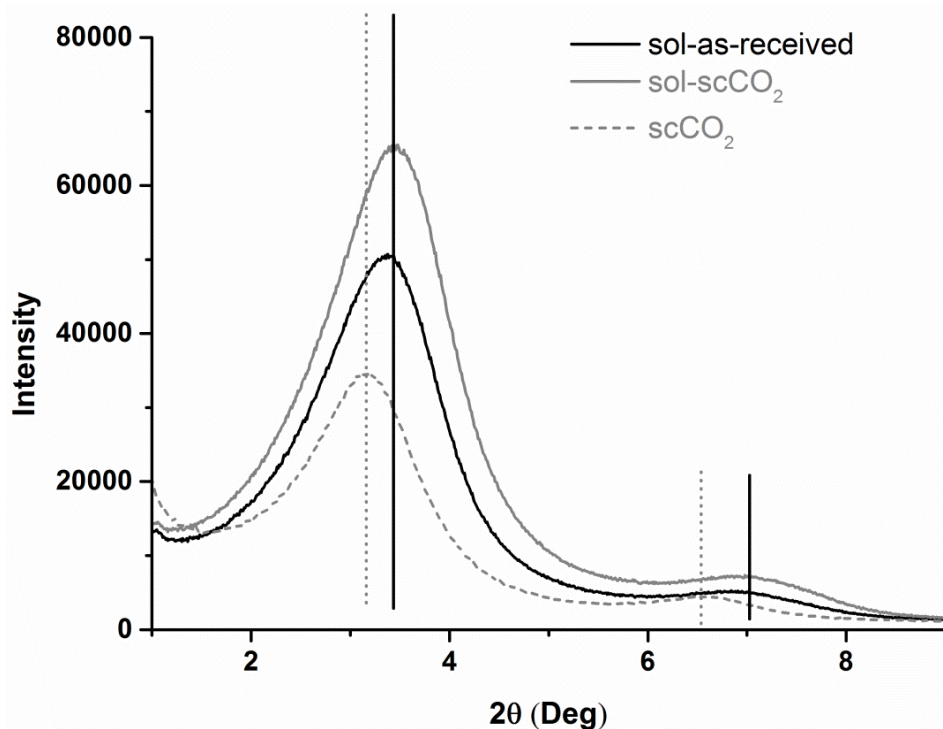
Figure 45 as-received and scCO$_2$ processed 20A recovered by using solvent (toluene).

In order to confirm the effects of the solvent on clay's reconstruction, we dissolved as-received and scCO$_2$ processed 20A with toluene and then evaporated the solvent gradually to precipitate the clay particles. The obtained solvent recovered clay samples were subject to WAXD analysis and the new diffraction patterns were compared with original ones as shown in figure 45. We found that both solvent recovered as-received and scCO$_2$ processed clay displayed similar diffraction patterns with identical diffraction peaks position which further confirmed that scCO$_2$ processing does not remove clay's surface modifiers. In addition, compared with the diffraction pattern before solvent recover, the diffraction peaks shifted to higher 2θ corresponding to a decrease of d-space, indicating that as-received and processed clays possess larger equilibrium d-spaces however, the large kinetic energy gained from solvent could re-construct the clay

96

to a much more stable state, which has a smaller d-space. We speculated that the observed phenomena are the main reason that we achieved limited improvement of dispersion, rheological and barrier property by using solvent blending. In fact, our research in next chapter by using melting extrusion displayed better improvements in dispersion, especially with low clay loading, because the kinetic limitation of clay dispersion no longer is an issue in the short times.

3.4 Conclusion

A series of polystyrene-clay nanocomposites with various types of clays were prepared by solution mixing, and the effects of modifiers and $scCO_2$ processing on nanocomposites were investigated by WAXD, TEM, rheology and permeability. Microstructural characterization revealed that, for $scCO_2$-processed clays, the presence of polymer between the dispersed platelets may prevent reorganization of platelets that were not in close proximity, resulting in a composite with a bimodal population of small ordered tactoids and dispersed platelets. Rheology suggested that $scCO_2$ processing improved clay dispersion and polymer-clay nanocomposites, resulting in low-frequency plateau in G', and increases in complex viscosities. With the increase of clay dispersion and interfacial interactions, gas permeation decreased. In this study, nearly 49% reduction in oxygen permeation could be achieved with only 1.09% volume fraction of $scCO_2$ processed Cloisite 10A clay. By substituted the relative permeations into two phenomenological models, we estimated the effective aspect ratio of the nano-clays, which compared well with the estimates from TEM images, and could be described by Cussler's random array model.

10A as the best reinforced candidate for PS was identified through preliminary study and a series of polystyrene/10A nanocomposites with various clay types (w/o scCO$_2$ process) and fraction were prepared by solution blending. The effects of scCO2 processing and composition on structure and properties of nanocomposites were investigated by WAXD, TEM, rheology and oxygen permeability. Microstructural characterization revealed that scCO$_2$ processed clays may prevented reorganization of platelets that are not in close proximity, resulting in a more homogenous dispersion with a bimodal population of small ordered tactoids and dispersed platelets, meanwhile, the increase surface area caused more intimate interfaces. Rheological behavior illustrated that formation of network structure lead to a plateau of storage modules in low-frequency and increase of complex viscosity. Additionally, scCO$_2$ processing displayed further improved dispersion of nanoclay. With the increase of clay fraction and dispersion, gas permeation decreased continuously, in this study nearly 83% reduction of permeation had been achieved with only 3.1 vol% volume fraction of scCO$_2$ processed clays. By fitting the experimental permeation data into several phenomenological models, scCO$_2$ samples exhibited more homogenous dispersion that was consistent with our TEM observation. Moreover, we found that Cussler's random array model was more valid and gave more realistic phenomenological fitting for those complex systems with the largest effective aspect ratio of 109 reported so far.

CHAPTER 4: SEMI-CRYSTALLINE POLYMER/CLAY NANOCOMPOSITES: STRUCTURE AND PROPERTIES

4.1 Introduction

Compared with amorphous polystyrene mentioned above, semi-crystalline or crystalline polymers possess stronger ability to organize and crystalize due to their regular steric structure or strong inter and intra molecular interactions. In other words, semi-crystalline or crystalline polymers normally show more compact and tough structure and better mechanical and barrier properties than amorphous polymers, which making them widely applied as engineering plastics in packaging industry. Therefore, it will result in tremendously and significantly practical and real-world applications, if we can successfully incorporate and exfoliate nanoclay particles into those more complicated polymeric matrix and improve polymer-clay interaction.
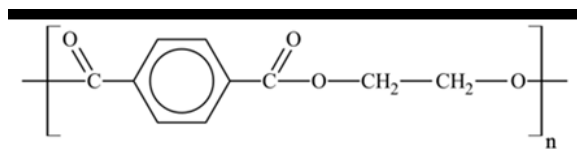
Figure 46 Chemical structure of Polyethylene terephthalate (PET).

Based on our previous research on amorphous polystyrene, this section of my dissertation focused on more complicated semi-crystalline polymeric matrix. Particularly, Polyethylene terephthalate (PET) (Figure 45), a semi-crystalline thermoplastic produced by condensation reaction of either dimethyl terephthalate or terephthalic acid with ethylene glycol, was used as matrix. Moreover, studies on barrier properties of high density polyethylene (HDPE) were also discussed.

Poly (ethylene terephthalate) (PET) is a semi-crystalline thermoplastic polymer, with slowly crystallization rate, that has been widely used in the beverage packaging industry [117-120]. Compared with an equivalent glass container, PET bottles have fairly light weight as well as superior mechanical properties and clarity [95]. However, their limited barrier properties restricted their tremendous applications in packages for beer or carbonated soft beverage which are sensitive to oxygen or lose of carbon dioxide [121, 122]. Several practical techniques, such as barrier coatings [123] and multilayer processing [124, 125], have been developed to improve PET barrier properties [126, 127]; however those methods might simultaneously introduce processing complexity and/or negatively impact mechanical properties and/or clarity [128]. In addition, additives may serve as heterogeneous nucleation sites, such as when $CaCO_3$ [129, 130] and fiber [131] are incorporated to PET to increase the crystallization rate and accommodate typical industrial injection molding processes. Considerable penalties on transparency and mechanical properties are expected with the application of excessive additives [132].

PET/clay nanocomposites have been reported to possess the potential of improving both barrier properties and crystallization rate of PET with limited negative effects on transparency and mechanical properties [133-137]. Well-dispersed clay in PET could create a tortuous pathway for permeants and serve as heterogeneous nucleation sites. S. Li, et al., used in situ polymerization to prepare PET/modified montmorillonite nanocomposites, whose water barrier improvement showed good agreements with previously published oxygen barrier results and can be rationalized in terms of tortuous path models [138]. M. Dini, et al., prepared PET/ Cloisite[®]30B nanocomposites by using

two different processes: conventional melt mixing and water-assisted melt mixing with solid state polymerization (SSP). The nanocomposites exhibited higher tensile modulus and lower oxygen permeability after SSP, and moreover the elongation at break was significantly higher than nanocomposites processed by conventional melt mixing [139] alone. A. Ghanbari, et al., compounded two different types of modified clay with PET in the presence of a multifunctional epoxy-based chain extender; and the finial composites displayed a significant decrease in oxygen permeation and increase of modulus [95]. C.I. W. Calcagno, et al., reported crystalline properties of PET/clay nanocomposites with different commercial clays where they found that clay nucleated the PET crystallization process and as the improvement of dispersion the nucleating effect was enhanced [120, 140]. H Ghasemi, et al., reported PET/ 3wt% Cloisite$^{®}$ 30B films had higher crystallinity than neat PET films due to the nucleating role of the silicate layers and the transparency of nanocomposites films remained in the acceptable range. Moreover, both oxygen barrier and modulus were enhanced [141]. However, aggregation and poor polymer-clay interaction are still significant obstacles on manufacturing superior PET/clay nanocomposites and limited success have been achieved on clay dispersion in PET through melting extrusion without help of additives or post-processing treatment [142, 143].

Recently, several scCO$_2$ based processing techniques have been reported to effectively disperse clay and form polymer/clay nanocomposites with superior properties [78, 86, 87, 92, 144]. Mihai Manitiu, et al., studied the effects of scCO$_2$ processing conditions on clay dispersion and polymer-clay interactions in polystyrene

(PS)/Cloisite® 10A system, where significant dispersion and rheological enhancement have been reported by using $scCO_2$ process and a co-solvent [60]. Quang T. Nguyen, et al., developed a $scCO_2$ aided extruder method by using a pressurized CO_2 chamber to assist exfoliation and deliver the clay directly into a stream of polymer melt in the extruder, where the resultant nanocomposites shows significant improvements in mechanical and rheological properties when compared with direct melt blending in single or twin-screw extruders [90]. Subsequently, Chen Chen, et al., modified Nguyen's processing method into a semi-continuous process by using a collecting chamber and compounded polypropylene (PP) /clay nanocomposites with help of maleic anhydride grafted polypropylene to enhance the $scCO_2$ processing. They reported remarkable improvements on modulus and tensile strength by 88 % and 12%, respectively compared to the pure polymer matrix, but limited improvements in rheology were reported [93, 94]. Up to now, limited research has been conducted on pre-dispersion of clay by $scCO_2$ processing and melting extrusion of polymer/$scCO_2$ pre-dispersed clay nanocomposite without the use of additives [85].

In this chapter, PET/clay nanocomposites were prepared by $scCO_2$ processing reinforced melt extrusion without the use of additives and post-processing treatment. The pre-dispersion of clay possessed a fluffy, low bulk density structure and exposed more available surface for the polymer to penetrate which could decrease kinetic limitation of clay dispersion during melting extrusion leading to improved clay dispersion. Subsequently, structural, mechanical, thermal and barrier properties and transparency of the melt compounded PET/clay nanocomposite with different clay modification (10A,

20A and 30B) and low clay fraction (≤5wt%) were investigated by using WAXD, TEM, rheometer, Instron mechanical testing, DSC and O_2 permeation to assess the effects of scCO$_2$ processing and clay modification and fraction on improving clay dispersion and physical properties of nanocomposites.

4.2 Experimental

4.2.1 Materials

Organically modified Cloisite® 10A 20A and 30B, with reported aspect ratios ranging from 10 to 300 [39] were obtained from Southern Clay Products and their composition and physical properties were summarized in Table 1. Bottle grade PET powder, with intrinsic viscosity of 0.8dL/g, glass transition temperature of 80°C and melting temperature of 245°C, were supplied by The Coca-Cola Company.

4.2.2 Nanocomposites preparation

PET powder and organic clays were firstly vacuum dried at 90°C for 12h before handling. Then PET resins with various types of clay (as-received or scCO$_2$ processed), modification (10A, 20A and 30B) and fraction (1, 3 and 5 wt%) were sealed in an aluminum foil bag and mechanically blended by using a Thumler's tumbler for 12h before extrusion. PET/clay nanocomposites were compounded by using a laboratory scale micro-compounder (Thermo Haake Minilab) with a recirculation channel which allows the processing of batches of typically 5–40 g, twin counter-rotating screws at a speed of 50rpm and a barrel temperature of 265°C. Finally, the extruded strands were cooled down to room temperature and chopped into pellets. Pure PET sample was

prepared following the same procedures as control. Thin film (~0.2mm) samples of pure PET and nanocomposites were prepared by melt pressing pellets into a custom-made cupper mold (diameter=56mm) between Teflon coated foil sheets. The films were allowed under a pressure of 4000psi at $268^{\circ}C$ with a purge of nitrogen for 10min, and then were instantaneously quenched by ice water to form quasi-fully amorphous film samples [95, 145]. The obtained thin film samples were vacuum dried at room temperature and kept in a vacuum desiccator before being subjected to WAXD, mechanical properties and permeation tests.

4.2.3 Digital optical pictures

A Fuji F30 digital camera was use to capture digital optical images of thin film (~0.2mm) samples of pure PET and nanocomposites prepared by above method. A Nikon TS100 microscope equipped with a digital camera was use to image the monopoly of fracture of tensile specimens.

4.2.4 Wide-angle X-ray diffraction (WAXD)

A Rigaku Rotaflex Powder Diffractometer with a Cu Kα X-ray source λ=1.54 Å (accelerating voltage= 44 kV, current=120 mA) was used to assess the clay intergallery spacing. Composite films samples were placed in a custom-made, zero-background quartz sample holder that is 0.9 mm in depth. Several scans were obtained from different locations in the sample and verified to be reproducible when diffraction patterns were superimposed on one another. The 2θ angle was determined using the JADE software

that accompanies the diffractometer, and the d_{001} spacing for the clays was calculated using Braggs' Law of diffraction.

4.2.5 Thermal gravimetric analysis (TGA)

A Perkin Elmer Pyris 1 thermal gravimetric analyzer with thermal analysis gas station was used to monitor the change of clay's surficial chemical modification before and after $scCO_2$ processing. Thermal gravimetric data were collected from 20 to 650 ^{o}C with a heating rate of 10°C/min, and whole test under dry air atmosphere with an air flow rate of 20ml/min.

4.2.6 Transmission electron microscopy (TEM)

Thin sections (70-100nm) of the nanocomposites were prepared using a Leica Ultramicrotome with a diamond knife (knife angle=35°) and placed on 200 mesh copper grids coated with carbon. All samples were examined with a Hitachi H7600 Transmission Electron Microscope operated at 80 kV. Numerous (10-15) images were collected for all samples to ensure accurate representation of the clay morphology and dispersion in the polymer matrix.

4.2.7 Rheology

An ARES rehometer was used to measure rheological properties of pure PET and PET/clay nanocomposites. Disk shape specimens of approximately 2 mm thickness and 25 mm diameter were prepared by employing a Carver laboratory press and customized model at 268 ^{o}C for 9 min at a pressure of 27.6MPa under a purge of nitrogen, followed

105

by quenching in 50°C vacuum oven for 9 min. The compression molded specimens were vacuum dried at 100 °C for 12 h before being subjected to rheological testing. The tests were conducted under a protection of nitrogen to avoid oxidation of the samples. Parallel plates geometry were used with a gap size of 1 mm and a plate diameter of 25 mm. Strain and frequency sweeps were carried out on the samples at 265 °C. Strain sweeps were performed to ensure that the dynamic moduli were independent of the strains utilized, and the linear viscoelastic measurements were made at low strains (< 0.20) to minimize microstructure destruction. The frequency range used was 0.1-100 rad/s.

4.2.8 Mechanical properties

An Instron 5966 mode universal mechanical tester was used to measure mechanical properties of thin films (~0.2mm) of pure PET and nanocomposites prepared by above method. The tensile specimens were cut into dog bone shape by using a customized stamp cutter with a 10mm length and 7mm width narrow zone and were stretched at a crosshead speed of 1mm/min under room temperature. Duplicate specimens (5~9) were analyzed for each sample to get an average.

4.2.9 Differential scanning calorimetry (DSC)

A TA Q200 Differential Scanning Calorimeter (DSC) with Auto Sampler was used to determine thermal and crystallization behaviors of PET and PET/clay nanocomposites. The samples weights were kept about 5 to 10 mg and were dried at 60°C for 6 h in a vacuum oven before DSC characterization. All measurements were carried out in nitrogen atmosphere. The samples were heated first to 300°C at 10°C/min and hold

for 3 min to remove the thermal history. The samples were then rapidly cooling at 50^oC /min to 30 ^oC and re-heated at 10^oC/min to 300^oC. Both crystallization and melting parameters were obtained from the cooling and re-heating scans. The test was performed on duplicated specimens for each sample to ensure the accuracy.

4.2.10 Oxygen permeation

Oxygen transmission rates (OTR) were measured using MOCON OX-TRAN 2/20 instrument at continuous mode and active individual zero. Film samples prepared by above procedure were masked with aluminum foil masks to expose a measurement area of $5cm^2$ and mounted between two chambers at ambient atmospheric pressure. Masks provide support and a uniform area of measurement for small sample sizes. One hundred percent oxygen was continuously admitted at 10 SCCM to the outer chamber and a carrier gas which was a mixture of 98% nitrogen and 2% hydrogen was continuously admitted at 10 SCCM to the inner chamber. As oxygen permeates through the film samples, it was picked up by the carrier gas and carried through an electrochemical oxygen sensor. The environmental test conditions used in the diffusion cells of the instrument were 0% relative humidity and under three different temperatures (13, 23 and 33^oC). Finally, obtained OTR was multiplied with average thickness of films to calculate permeation of oxygen. Duplicate specimens (3~4) were analyzed for each sample to get an average.

4.3 Result and discussion

4.3.1 Effects of scCO$_2$ processing and clay modifications on structural, mechanical, thermal and barrier properties of PET/clay nanocomposites

WAXD patterns of all of the nanocomposites in this study are shown in Figure 47. All nanocomposites exhibited well-defined both d$_{001}$ and d$_{002}$ diffraction peaks, regardless of their surface chemistry or scCO$_2$ processing, suggesting the presence of certain highly ordered clay structures in all nanocomposites. In addition, all of nanocomposites showed shifts of the d$_{001}$ peaks to relatively lower 2θ compared with corresponding pristine clays, suggesting that polymer had been intercalated into the clay galleries. In particular, 10A, 20A and 30B reinforced PET nanocomposites displayed d$_{001}$ diffraction peaks at 2θ equal to 2.54°, 2.4^o and 2.55^o which corresponding to increases of inter gallery spacing from 1.05 to 2.47 nm, 1.77 to 2.68nm and 0.88 to 2.46nm respectively. The increase of inter gallery spaces for 10A, 20A and 30B reached to 135%, 51.4% and 180% respectively, suggesting that 10A and 30B might possess more favorable polymer-clay interaction than 20A did. Even though scCO$_2$ processed clay did not further shift the diffraction peaks, the decrease of intensity might indicate a decrease of ordered structure inside those composites. We speculate that for scCO$_2$ processed clays, the exfoliated platelets and expanded clay particles structure significantly weakened their reorganizations as the presence of viscous polymer in extrusion, resulting in a composite with a bimodal population of small ordered tactoids and dispersed platelets pairs. However, WAXD is only sensitive to ordered clay structure and could not provide information on exfoliated structure and spatial distribution of clay particles, solo WAXD could not be representatives to structural details of the complex nanocomposites system [45].
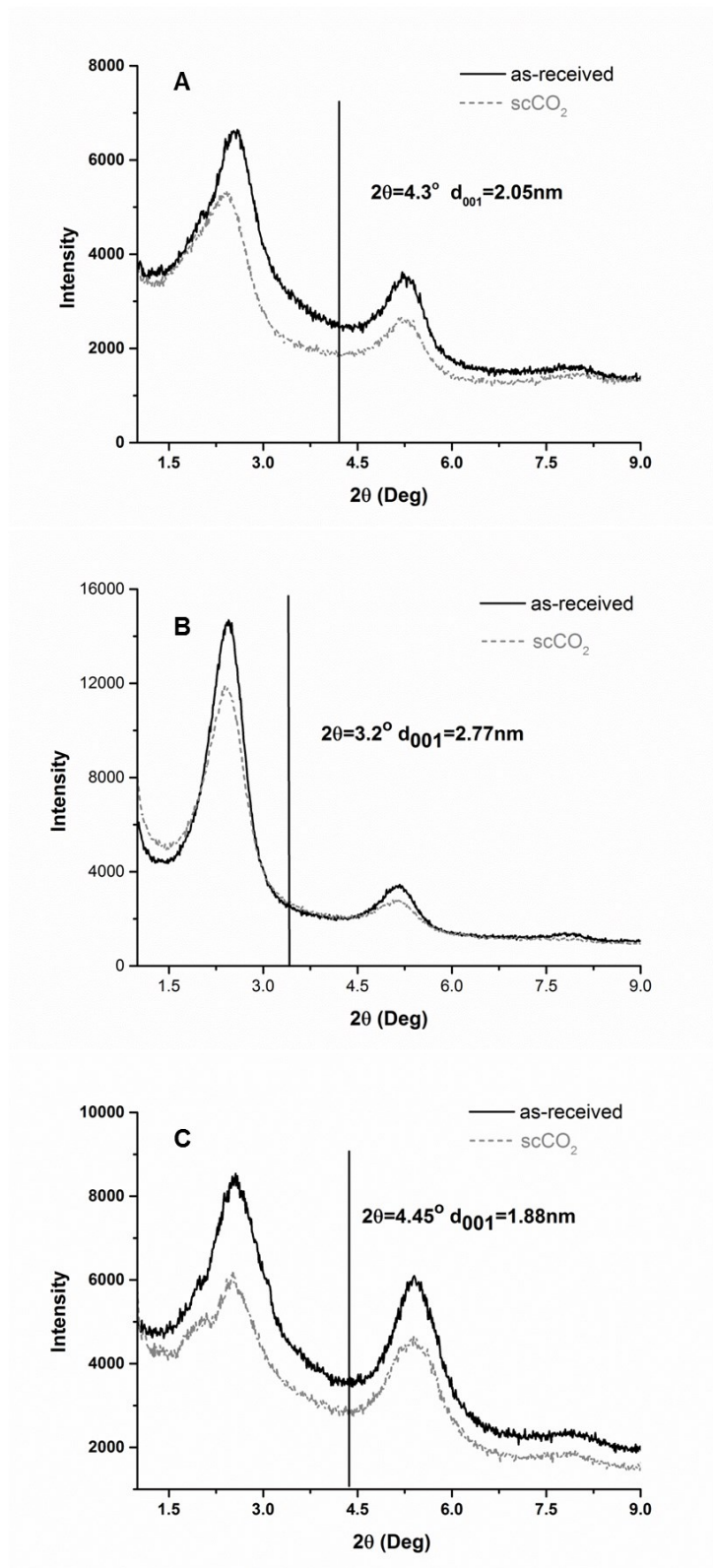
Figure 47 WAXD patterns of PET/clay nanocomposites with 5wt% clay (A) 10A, (B) 20A and (C) 30B.

The morphology and spatial dispersion of the clays in the nanocomposites were visualized by transmission electron microscopy to complement WAXD data. Figure 48 presents representative TEM images of PET/clay nanocomposites with 5wt% of different clays. Both 10A and 20A showed relatively uniform dispersion inside PET, even though as-received 20A displayed certain degree of aggregation. 10A illustrated better dispersion than 20A and the average size of particles in 10A was smaller than that of 20A. In contrast, 30B demonstrated less dispersion, severe aggregation can be observed in as-received clay, although scCO$_2$ processing further improved clay dispersion as significantly decreased the average particle size, aggregation still can be observed. In general, relatively severe and large agglomerates of tactoids and few exfoliated tactoids were observed in as-received clay reinforced sample, which is highly consistent with what we have detected in SEM images for as-received clay, in which most of tactoids were observed in the form of tightly bundled particles and only few of them were exfoliated. Those tight and large particles placed considerable kinetic barriers to be broken down during melting extrusion even with strong shearing stresses; therefore the original structural characters of the as-received clay were preserved and transferred to the nanocomposites. In contrast, significant improvement on clay dispersion was observed in scCO$_2$ processed samples, nevertheless partially aggregations still exist. Most of the tactoids were in the dispersed form, which increased clay density (number of particles per unit area) and improved homogenous distribution of clay particles in comparison of as-received clay. In fact, the relatively low content of severe agglomerates in scCO$_2$ processed sample in turn leaded to an increase of the effective aspect ratio. Moreover, the average size of the particles and the tightness of packing were significantly reduced, there

results are in good agreement with WAXD patterns as the peaks broadened and their densities decreased. It is reasonable to speculate 10A could render best improvement in barrier properties since best dispersion were obtained in this case, however further investigation revealed the importance of polymer-clay interaction in improving barrier properties and details will be discussed in the following sections.
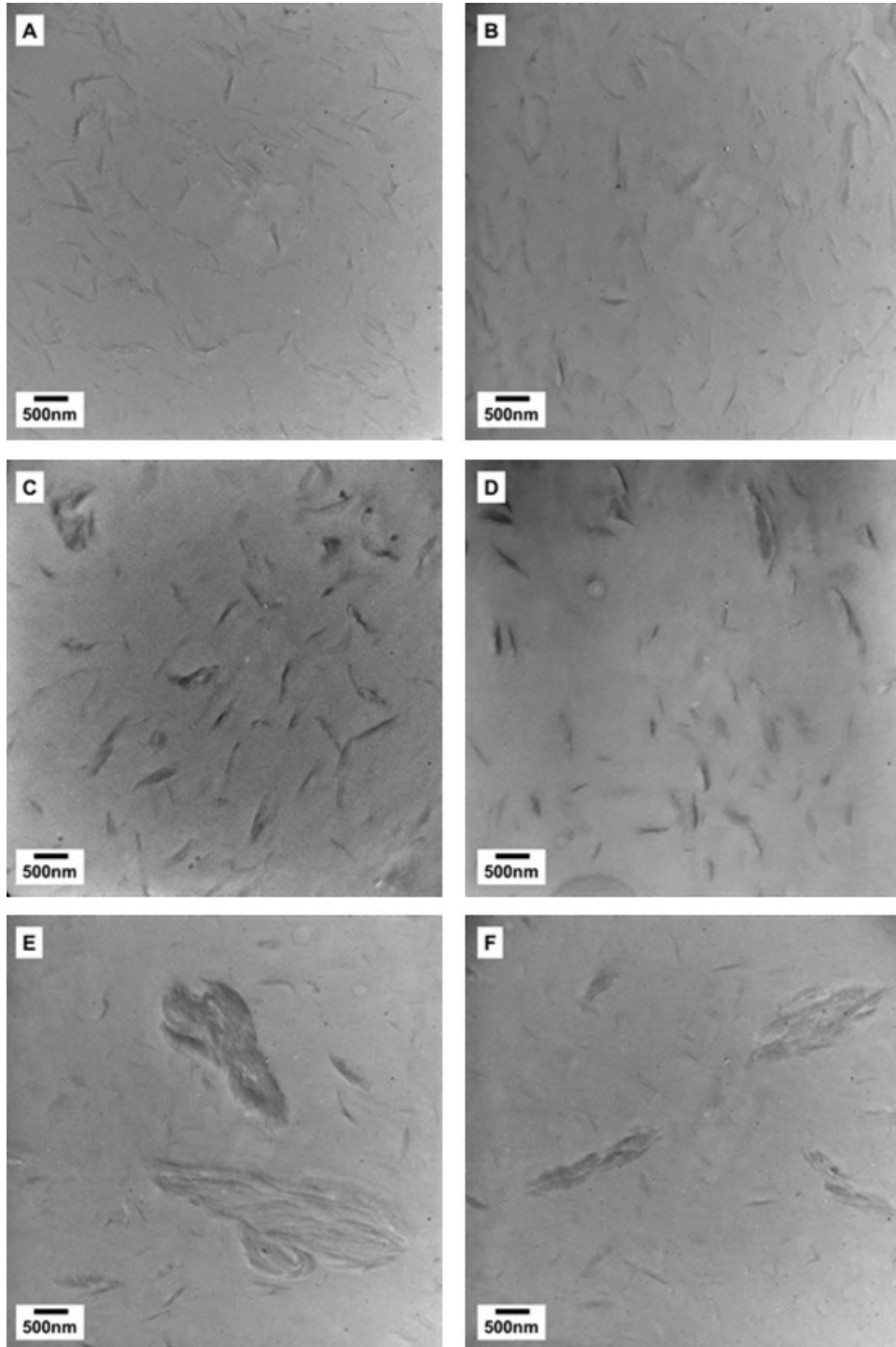
Figure 48 TEM images of PET/clay nanocomposites (5 wt%) (A) as-received 10A, (B) scCO$_2$ processed 10A, (C) as-received 20A, (D) scCO$_2$ processed 20A, (E) as-received 30B and (F) scCO$_2$ processed 30B.

Rheology is sensitive to clay dispersion and polymer-clay interactions. In this section, we investigate the effects of clay modification and $scCO_2$ processing on the rheological behavior of nanocomposites melts. The storage modulus (G') and complex viscosity (η^*) of PET/clay nanocomposites melts are compared in figure 49 (A) and (B), respectively. Typically, it is reported that with incorporation of clay, a plateau in the storage modulus, G', versus frequency is observed at low frequencies due to either forming of networks between modifiers and matrix or presenting of large agglomerates [90]. Figure 49 (A) suggests that all of nanocomposites exhibited improvements of storage modulus at low frequency when compared with pure PET. In the cases of 10A and 20A reinforced nanocomposites, the observed low-frequency plateaus were attributed to the formation of network between polymer and clay as have been detected in TEM images, where clay dispersion plays very important role in improving storage modules, 10A nanocomposites demonstrated better improvement in modules than 20A did because of the improved clay dispersion which is consistent with TEM observation. However, $scCO_2$ processing failed to further improve storage modulus, because the strong network structure formed by high clay loading suppressed the effect of improved dispersion by $scCO_2$ processing.   In contrast, for 30B reinforced nanocomposites, the increase of modulus at low frequency was due to presenting of large agglomerates since severe aggregations were observed. It is worth to emphasis that it was hard for rheometer to detect stable relaxation in nanocomposites with as-received 30B due to ununiformed distribution of clays, whereas $scCO_2$ processed clay presented more homogeneous dispersion as shown in TEM images. Nevertheless, the storage modulus seems to be more

113

sensitive to the formation of network structure rather than presenting of large agglomerates.

The complex viscosities of all nanocomposites are compared with the pure PET in figure 49 (B). We note that the pure PET displayed a Newtonian flow behavior in the testing frequency range, whereas both 10A and 20A samples demonstrated shear thinning flow behavior with significant increased viscosities at low frequency. We speculate the network structure dominated the melting flow behavior at low and decreased the mobility of PET macromolecules. With increase of frequency, however, the network structure was destroyed due to the orientation of clay and the flow behavior was dominated by the polymer chains. In contrast, 30B exhibit decrease of viscosity in the full frequency range, this may be due to lack of network structure and the large agglomerates of clays failed to effectively block the movements of PET chains. As goes to higher frequency, the dispersed clay might play as plasticizer to increase mobility of polymer chains due to increase the slip or inhomogeneous flow [146, 147]. All of three types of clays exhibited reduction of viscosities at high frequency, which is consistent with the observation of decreasing torque during extrusion. Interestingly, the decrease of viscosity follows the trend of 30B>10A>20A, which indicating stronger polymer-clay interaction could enhance the plasticizing effect by facilitate movement of inhomogeneous flow [147]. Similarly, viscosities characterization also failed to capture the effect of $scCO_2$ on improving clay dispersion due to high clay loading.

.
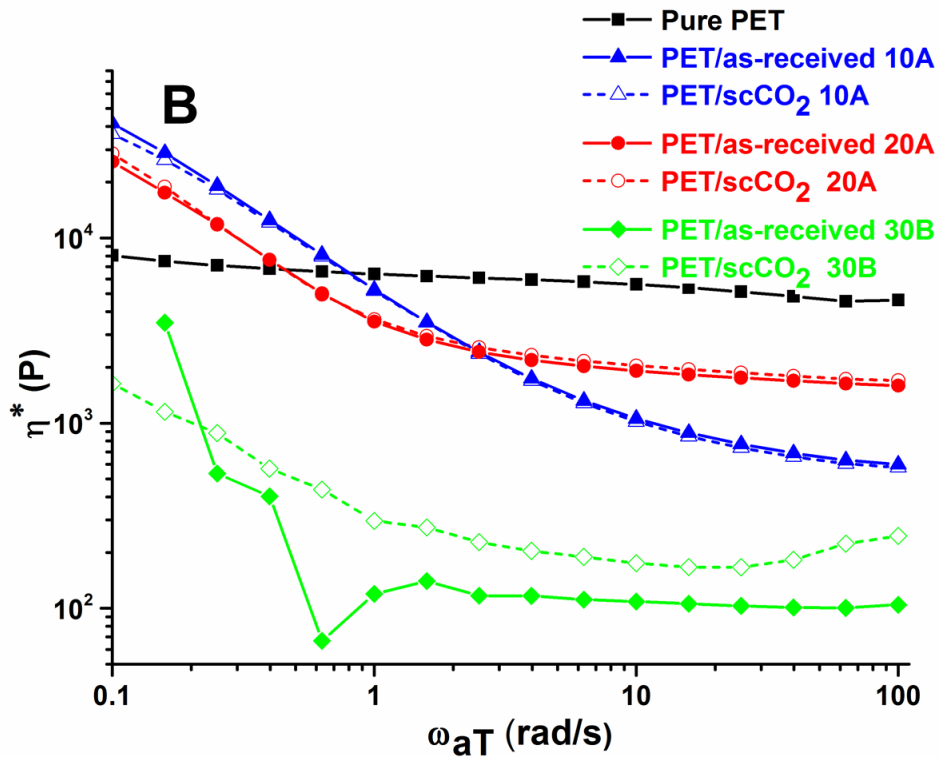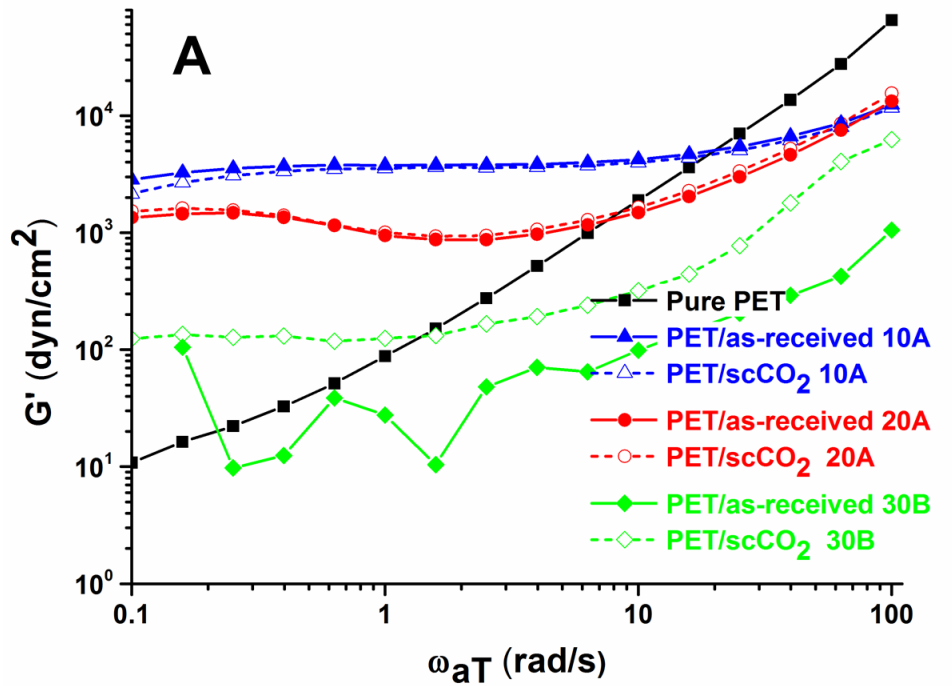
Figure 49 Rheology of pure PET and PET/clay nanocomposites (5 wt%) at 265°C (A) storage modulus vs. frequency (B)complex viscosity vs. frequecy.

Typical stress-strain curves up to the full range of recorded strain values for pure PET and PET/clay nanocomposites are shown in Figure 50. The deformation of pure PET followed typical elastic-plastic transition behavior and the elongation at break for pure PET was measured to be about ~370%. In comparison, all of nanocomposites exhibited significantly different deformation behavior from the pure matrix, all of nanocomposites with 5 wt% of clay showed dramatically decrease of ductility and displayed brittle fractures within 4% of strain. Compared with pure PET, all of nanocomposites demonstrated significant decrease of tensile strength and increase of Young's modulus. In particular, the decreases of tensile strengths for all clay samples are comparable since the high loading of clay particles enhanced chance of severe aggregation which could serve as stress raisers, whereas all nanocomposites displayed continuously increase of Young's modulus in the order of improved clay dispersion as 10A>20A>30B. Similar trend was also observed for nanocomposites with $scCO_2$ processed clay, whereas the corresponding Young's modulus was increased when compared to equivalent nanocomposites with as-received clay. We attribute the increase of Young's modulus to improved clay dispersion in $scCO_2$ processed samples, and similar results had been reported by Chen et al that PP/clay nanocomposites with $scCO_2$ processing exhibit further increase in Young's modulus [94].
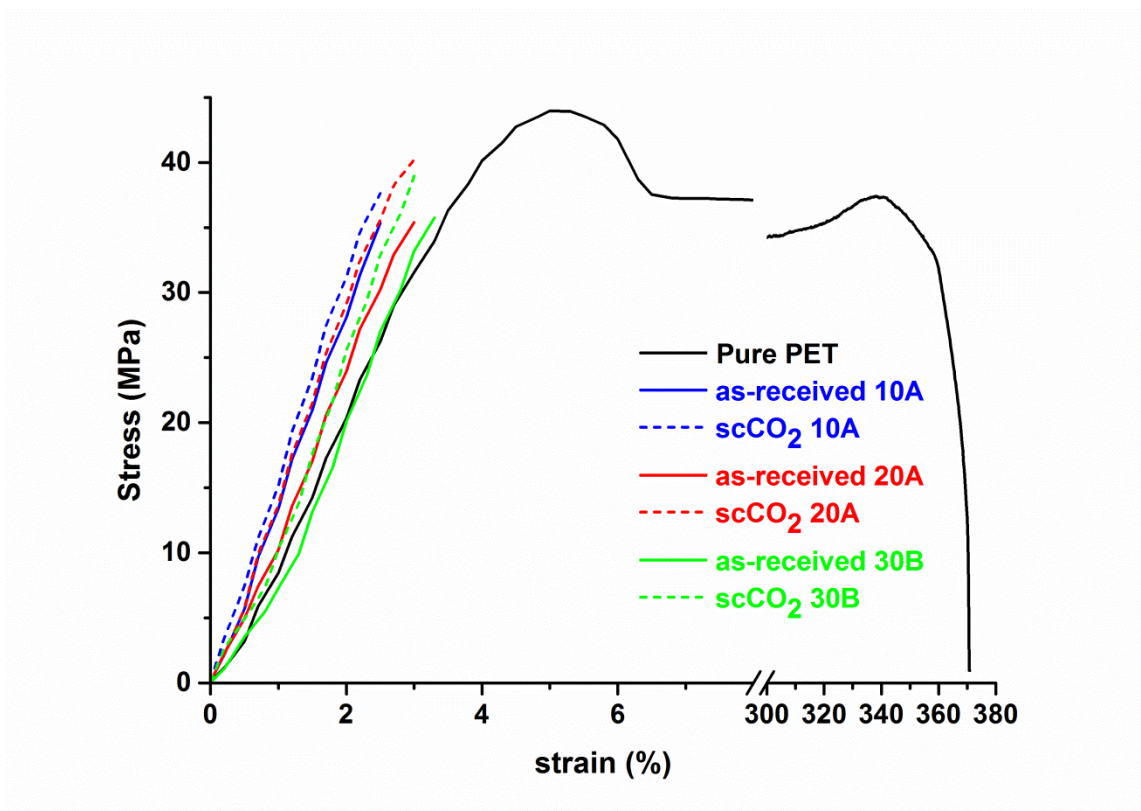
Figure 50 Typical stress-strain curves for PET and PET/clay nanocomposites.

All of mechanical properties of the pure PET and PET/clay nanocomposites are summarized in Table 6. Young's modulus could be improved either by improving clay dispersion through changing clay surface modification or by adding $scCO_2$ processed clay which improved homogenous dispersion of clay. In comparison with as-received clay, $scCO_2$ processed clay displayed significant improvements on Young's Modulus and limited enhancement on tensile strength due to eliminating the large agglomerates of clay particles that could serve as stress concentration site. The best improvement in Young's modulus was achieved by using 5wt% of processed 10A where the Young's modulus was improved by 34.8% compared with pure PET. Moreover, the 10A reinforced nanocomposites exhibited more brittle behavior than 20A and 30B, which was attributed to the good clay dispersion and strong polymer-clay interaction.

117

Table 6 Mechanical properties and inorganic clay volume fraction of pure PET and PET/clay nanocomposites

Sample	Tensile strength (MPa)	Decrease (%)	Young's Modulus (MPa)	Increase (%)	Elongation at break (%)	Inorganic clay volume fraction (%)
Pure PET	43.0±1.7	-	1243±23	-	373±4.6	-
PET/5wt% as-received 10A	35.3±3.1	17.9	1592±41	28.1	2.6±2	1.41
PET/5wt% scCO$_2$ 10A	38.1±2.3	11.4	1675±39	34.8	2.5±0.1	1.41
PET/5wt% as-received 20A	34.5±1.3	19.8	1440±39	15.8	3.2±0.1	1.43
PET/5wt% scCO$_2$ 20A	40.1±1.4	6.7	1570±65	26.3	3.3±0.1	1.43
PET/5wt% as-received 30B	34.5±1.5	19.8	1412±14	13.6	3.1±0.04	1.62
PET/5wt% scCO$_2$ 30B	38.7±1.3	10	1562±27	25.7	3.3±0.15	1.62

The measured moduli were compared with predictions by composite theory models to assess the effect of scCO$_2$ processing and clay modification on improving mechanical properties. One of models that are commonly used to estimate the properties of polymer composites is the Halpin-Tsai [148] model which estimate the composite Young's moduli based on filler and matrix physical properties with different assumptions regarding to dispersion and orientation of the filler particles. Halpin-Tsai model assumes fully exfoliated and unidirectional clay platelets, which was expressed by the following equation:

$$E_C = E_m \left[\frac{1 + \xi \eta \phi_f}{1 - \eta \phi_f} \right]$$

Where,

$$\xi = 2(\frac{l}{t}) \quad \text{and} \quad \eta = \left[\frac{E_f / E_m - 1}{E_f / E_m + \xi} \right]$$

Where, E_f, E_m and E_c are the filler, matrix, and composite modulus, respectively. ϕ_f is the inorganic clay volume fraction and l/t is the aspect ratio of the clay particles. The Young's modulus of inorganic clay E_f was taken as 178 GPa [94] and the Young's modulus of matrix was measured to be 1243±22.6MPa , the aspect ratio of the silicate platelets (l/t) was reported in the range from 10 to 300 [39]. In our study, the volume fraction of inorganic clay of composites can be calculated from:

$$\phi_f = \frac{\phi_W \times (1 - W_{WLI}) / \rho_C}{\phi_W / \rho_{OC} + 1 / \rho_P}$$

Where, ρ_{OC}, ρ_C and ρ_P are the density of organic clay, inorganic clay and polymer matrix, respectively. The densities of clay samples are summarized in Table 1 and the density of matrix is 1.37g/cm^3. ϕ_W is weight fraction of organic clay and W_{WLI} is weight loss of organic clay on ignition (given in table 1). The calculated volume fractions of inorganic clay were given in Table 6.

Figure 51 presents the experimental and modeled results for Young's modulus of PET/clay nanocomposite as a function of clay aspect ratio and fraction based on the Halpin-Tsai model. It showed that the nanocomposites modulus can be dramatically enhanced by increasing clay aspect ratio or inorganic clay fraction. The experimental Young's moduli of 20A and 30B failed to reach the reasonably predicted range by using Halpin–Tsai model, whereas the experimental Young's moduli of 10A fall into the reasonably predicted range but displayed relatively low effective aspect ratio. Those may be due to a lack of complete dispersion of clay as individual palates, lack of strong

interactions between clay and the matrix and lack of complete orientation of the clay particles in the tensile direction. In comparison with nanocomposites reinforced by as-received clay, the corresponding nanocomposites with processed clay showed higher effective aspect ratio due to improved clay dispersion, whereas aggregation of clay particles inside as-received sample could reduce the amount of reinforcement that the clays can provide, resulting in less enhancement of the Young's modulus [93].
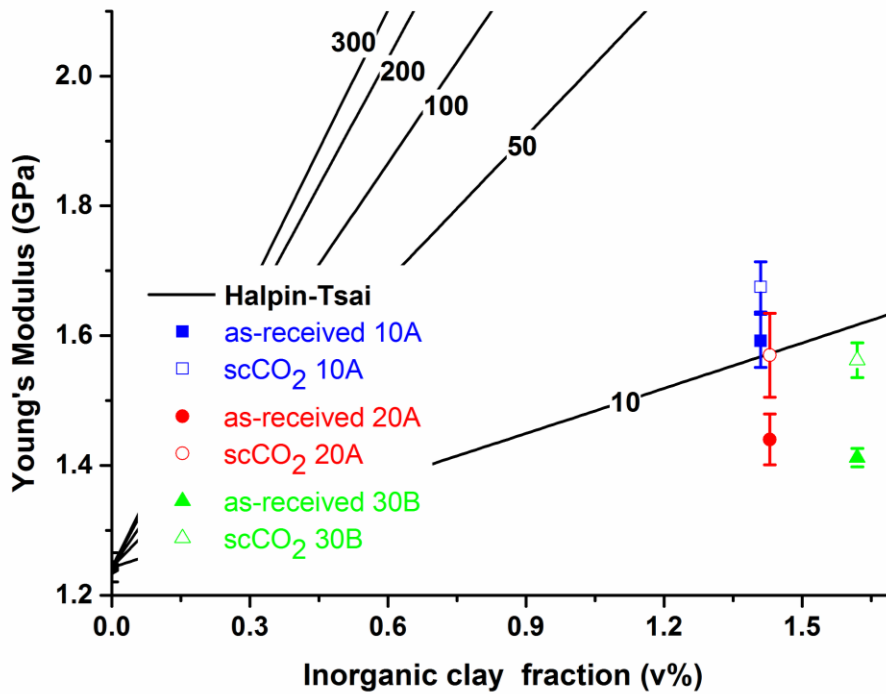
Figure 51 Experimental Young's moduli of PET/clay nanocomposites and comparison with theoretical predictions.

Figure 52 presents the DSC cooling and re-heating cycles for pure PET and PET/clay nanocomposites. In comparison with pure PET, incorporation of clay significantly changed the thermal behaviors of PET matrix. During the rapidly cooling cycle, pure PET displayed a relatively weak crystalline peak around 152.6°C due to its

slowly crystallizing rate, whereas all of the nanocomposites exhibited distinct crystalline peaks with shifting to higher temperature. Reversely, for the re-heating cycle, pure PET demonstrated a notable crystalline peak around 139.4°C, however no distinct crystalline peaks were observed for all nanocomposites and their melting peaks slightly shifted to higher temperature than that of pure PET. The significant changes of crystalline behavior were attributed to the heterogeneous nucleating effect of clay particles. Similar crystallization phenomena have been reported by other researches and further study found that the crystallization rates of PET/clay nanocomposites were increased significantly [149]. The crystallinity of the samples before re-heating could be calculated from the enthalpy of melting ΔH_m and the enthalpy of crystallization ΔH_{hc} obtained from the re-heating cycle by applying the following equation:

$$\chi_c = \frac{(\Delta H_m - \Delta H_{hc})/w_{PET}}{\Delta H^0}$$

where W_{PET} is the PET weight fraction and ΔH^0 is the enthalpy of melting of 100% crystalline PET (140J/g) [150]. Relative higher crystallinities of nanocompsoites were summarized in table 7 confirmed that the presence of clay enhanced crystallization of PET.
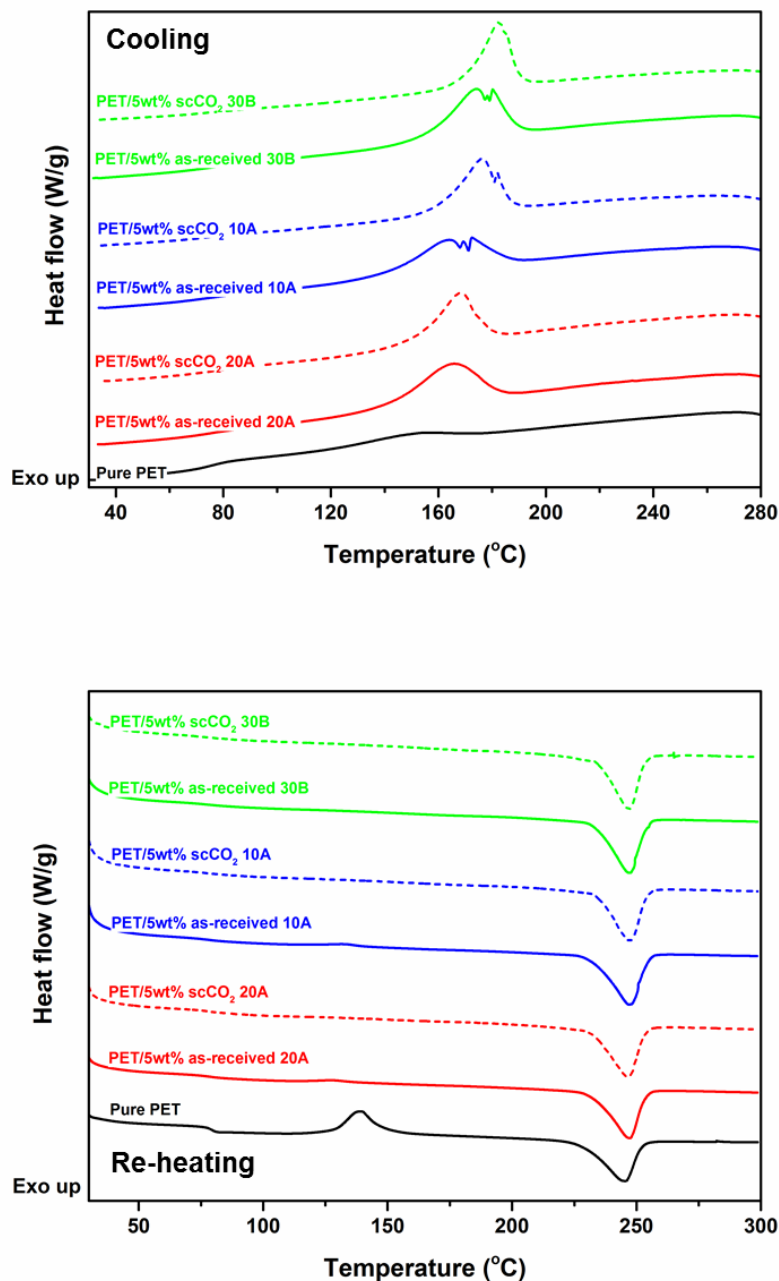
Figure 52 DSC Curves of neat PET and PET/clay nanocomposites

A. cooling, B. re-heating.

Table 7 also reports the effects of $scCO_2$ processing and clay modification on cooling crystallization temperature, T_{cc}, enthalpy of cooling crystallization, ΔH_{cc}, glass transition temperature, T_g, melting temperature, T_m, enthalpy of re-heating crystallization,

ΔH_{hc} and enthalpy of melting, ΔH_m of PET. It has been reported that the heterogeneous nucleating sites could facilitate crystallization by significantly reduce the activation energy for nucleation, in addition strong surface interaction and wetting could further enhance the heterogeneous nucleating effect. As we can see, the T_{cc} of nanocomposites significantly shifted to higher value and corresponding enthalpy increased slightly as function of changing clay modification (30B>10A>20A) or improving clay dispersion by scCO$_2$ processing, those phenomena could attribute to the enhancement of heterogeneous nucleating effect by either improving surface interaction or increasing number of nucleation sites. Moreover, in comparison of nanocomposites with as-received clay, the crystallization peaks of scCO$_2$ processed samples became narrow and sharp, which might be caused by the improved homogenous dispersion of clay.

All of nanocomposites demonstrated slightly increase of T_g as compared with pure PET. In the cases of dispersed nanocomposites (10A and 20A), the movement of polymer chains were blocked by dispersed clay particles, and with the improving of clay dispersion by scCO$_2$ processing, the corresponding T_g increased. In contrast, the slightly higher T_g for as-received 30B reinforce sample can be attributed to large amount of polymer intercalated between platelets and/or the presence of larger clay particles which could confine the movement of polymer chains [50, 151]. In addition, the rest of thermal properties of all nanocomposites failed to reveal any variation as function of clay modification or scCO$_2$ processing, indicating that increase of heterogeneous nucleating effect and improvement of clay uniform distribution have very little effects on re-crystallization and meting process of PET matrix. On the basis of DSC data, scCO$_2$

resulted in improved dispersion of clay with delaminated structure and uniform distribution, which is highly consistent with what we have seen in previously structural characterizations.

Table 7 Thermal properties of pure PET and PET/30B nanocomposites.

Sample	Cooling		Re-heating					
	T_C (°C)	ΔH_C (J/g)	T_g (°C)	T_C (°C)	T_m (°C)	ΔH_C (J/g)	ΔH_m (J/g)	Crystallinity (%)
Pure PET	152.6	NA	79.7	139.4	244.9	16.4	34.8	13.1
PET/ 5wt% asreceived 10A	166.5	26.1	84.9	NA	246.8	0	35.1	26.4
PET/ 5wt% scCO₂ 10A	176.3	30.9	86.3	NA	247.5	0	36.0	27.1
PET/ 5wt% asreceived 20A	166.1	27.1	84.8	NA	247.5	0	33.7	25.3
PET/ 5wt% scCO₂ 20A	168.4	27.8	86.1	NA	246.6	0	33.5	25.2
PET/ 5wt% asreceived 30B	174.2	32.8	86.6	NA	247.3	0	36.1	27.1
PET/ 5wt% scCO₂ 30B	182.7	35.0	85.3	NA	247.1	0	36.3	27.3

Figure 53 presents the oxygen permeations of pure PET and clay reinforced nanocomposites as functions of clay modification and $scCO_2$ processing. Unlike what has been expected that incorporation of impermeable clay particles into PET could both lower the solubility (decreasing organic phase) and effective diffusivity (creating tortuous pathways) of permeant. Permeation data reported here demonstrated highly dependence between barrier properties of PET/clay nanocomposites and clay modification, in the other word polymer-clay interaction. In particularly, the improvements in barrier properties follow the trend of improved polymer-clay interaction (30B>10A>20A).

Interestingly, 30B exhibited the worst clay dispersion but demonstrated the best improvements in barrier properties; a 22.6% reduction of permeation was achieved by adding 5wt% of 30B. On the other hand, although 20A showed moderate clay dispersion, enhanced oxygen permeations were observed when compared with pure PET. Those scenarios illustrated that polymer-clay interaction plays a key role in improving barrier properties in PET/clay nanocomposites. In comparison of sample with as-received clay of same clay loading, although $scCO_2$ processed clay leaded to better clay dispersion and distribution, no significantly further improvements in barrier properties were observed in all nanocomposites samples, which is conflict with what have been reported [144]. In the case of 10A, $scCO_2$ processed clay inversely enhanced oxygen permeation. We attribute the excessive clay loading offset the effect of $scCO_2$ processing on dispersion.
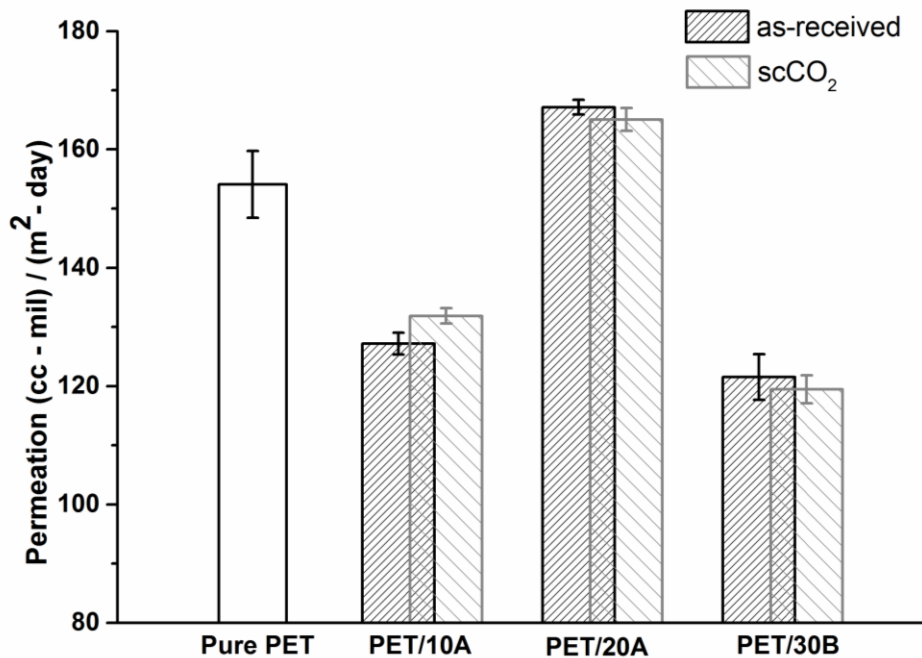
Figure 53 Oxygen permeations of pure PET and PET/clay nanocomposites.

As shown in Figure 54, the pure PET film exhibited high transparency and clarity. Although discolor were observed with the incorporation of clay, all the nanocomposites maintained the high transparency of the pure PET. The reason for discolor could be the degradation of the modifier on the clay surface since the melting extrusion temperature is $265^{o}C$ while the temperature of first maximum weight lose peak for 10A, 20A and 30B are 228.5 ^{o}C, $310^{o}C$ and $274^{o}C$ respectively. 20A with highest thermal stability displayed the least discolor then followed by 10A and 30B. We speculated that although 30B has moderate thermal stability, its decomposition is more complex. In comparison with nanocomposites reinforced by as-received clay, the nanocomposites with processed clay exhibited slightly improvement on optical clarity of the nanocomposites, which might primarily resulted from both the exfoliated structure of the clay layers and the efficient dispersion of the clay particles in the PET matrix as evidenced by the XRD and TEM results.
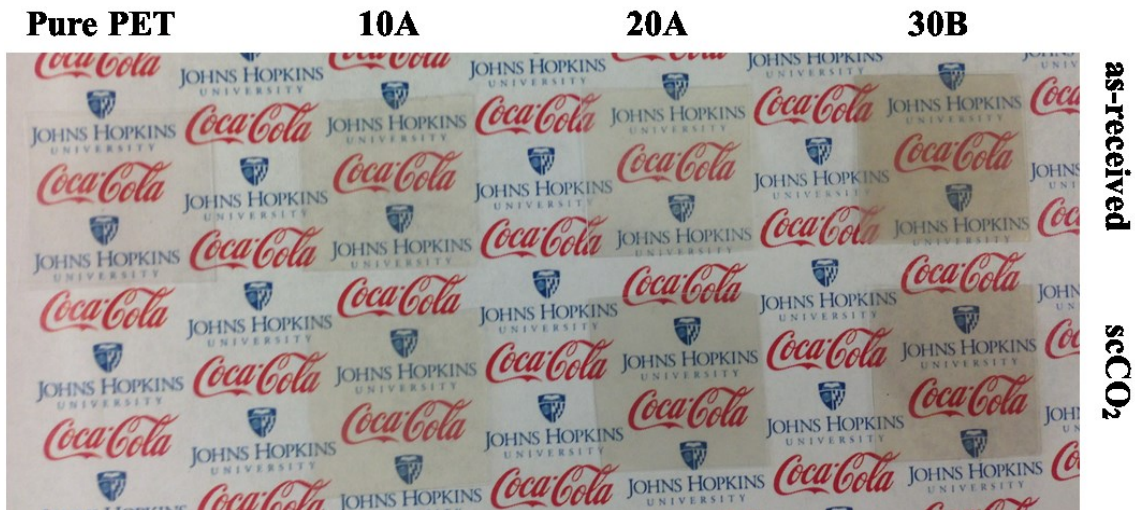
Figure 54 Optical images of pure PET and PET/clay nanocomposites films (thickness ~0.2mm)

4.3.2 Effects of scCO$_2$ processing and composition on structural, mechanical, thermal and barrier properties of PET/clay nanocomposites

As shown in figure 55, most of nanocomposites exhibited both sharp d$_{001}$ and d$_{002}$ diffraction peaks indicating those nanocomposites still contain some highly ordered clay structures. In addition, all of nanocomposites displayed similar shift of the diffraction peaks to lower 2θ when compared with pristine clay. For example, the d$_{001}$ diffraction peaks of all nanocomposites shifted to 2θ=2.4° corresponding to an increase of d-spacing from 1.88 nm for pristine clay to 3.46 nm, suggesting that polymer had been intercalated into the clay galleries, nevertheless scCO$_2$ processed clay did not result in further expansion of d-space. However, as compared with the as-received clay, scCO$_2$ processed clay presented significantly broadening the diffraction peaks and decreasing theirs intensities, which indicate the scCO$_2$ processing weakened the relative content of highly order clay structures. Especially at low clay loading case, the polymer rich sample showed absent of diffraction peaks which probably formed an exfoliated structure. We attribute the difference to improved spatial distribution of scCO$_2$ processed clay which suppresses inter-platelets/particles interactions and prevent orderly arrangment and aggregation of platelets and particles respectively. V. A. Richard, et al., previously modeled the intercalation behavior of clay in the presence of polymer and pointed out that even when the clay galleries are expanded to maximize the surfactant entropy, the separation is still small enough for typical polymers and restricts their motion [66]. Therefore, scCO$_2$ processing exposes moresurface area which leads to more thermodynamically favorable interaction than the intercalation case. WAXD is only sensitive to ordered clay structure and could not provide information on exfoliated

structure and spatial distribution of clay particles, solo WAXD could not reveal structural details of the complex nanocomposites system [45].
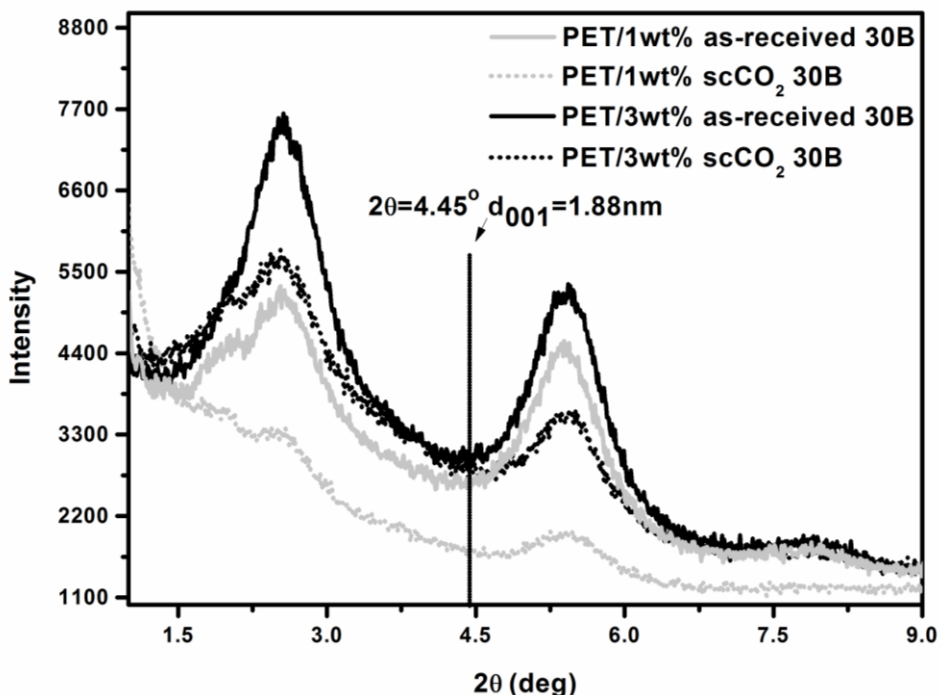
Figure 55 WAXD patterns of PET/clay nanocomposites at different clay fractions.

The morphology and spatial dispersion of the nano-clay in the nanocomposites were visualized by transmission electron microscopy to complement WAXD data. Figure 56 presents representative TEM images of nanocomposites with 3wt% of different clay. Relatively large agglomerates of tactoids (highlighted by white circle) and few exfoliated tactoids (highlighted by black circle) were observed in as-received clay reinforced sample, which is highly consistent with what we have detected in SEM images for as-received clay, in which most of tactoids were observed in the form of tightly bundled particles and only few of them were exfoliated. These tight and large particles placed considerable kinetic barriers that must be overcome during melting extrusion even with high shear stresses; therefore the original structural characteristics of the as-received clay

were preserved and transferred to the nanocomposites. Moreover, the existence of these large agglomerates cause heterogeneous dispersion of the clay and significantly decreases their effective aspect ratio which in turn reduces any enhancement of physical properties. In contrast, significant improvement of clay dispersion was observed in $scCO_2$ processed samples, though partially aggregated tactiods were still observed. Most of the tactoids were in the dispersed form, resulting in higher clay density (number of particles per unit area) and more homogenous distribution of clay particles relative to the as-received clay. Moreover, the relatively low content of large agglomerates in $scCO_2$ processed sample actually leads to an increase of the clay's effective aspect ratio. In addition, the average size of the particles and the tightness of packing were significantly reduced and these results are in good agreement with WAXD patterns as the peaks broadened and their intensities decreased.
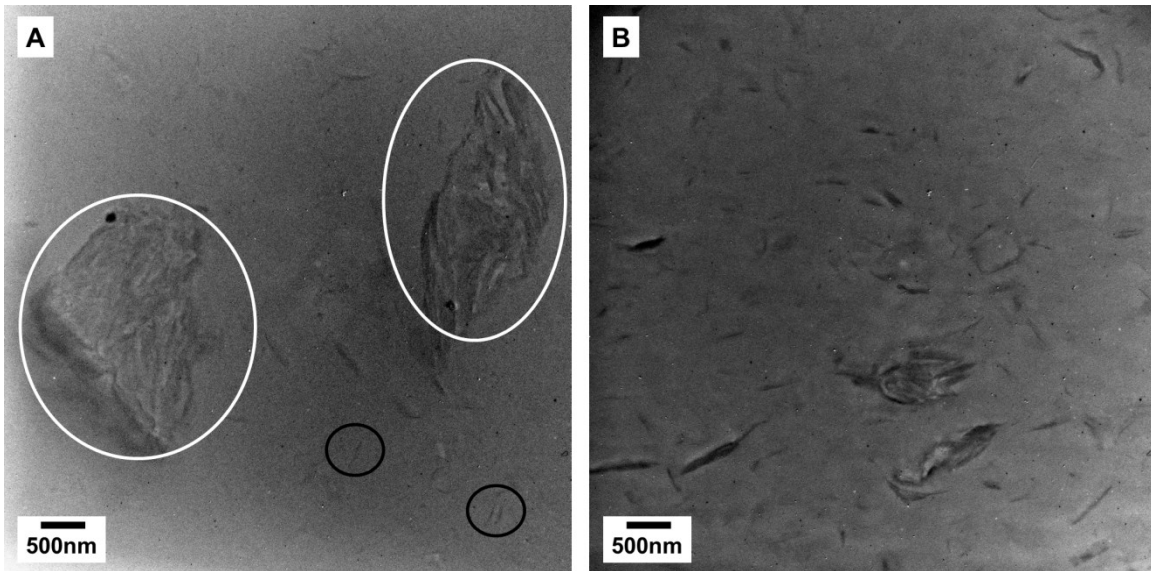
Figure 56 TEM images of PET/30B nanocomposites (3 wt%) A. as-received B. $scCO_2$ processed.

Typical stress-strain curves up to the full range of recorded strain values for the PET matrix and PET/30B nanocomposites with various types and fractions of clay are shown in Figure 57 (A). The deformation of pure PET followed elastic-plastic transition behavior and the elongation at break for pure PET was measured to be about ~370%. In comparison, the deformation behavior of nanocomposites with low clay fraction did not exhibit significant differences from the pure matrix, whereas, with increase of clay fraction, the nanocomposites became more brittle. For example, the specimens with as-received clay demonstrated a decrease of elongation at break from ~360% to ~70% as increasing clay fraction from 1wt% to 3wt%. Similar phenomena were also observed for nanocomposites with $scCO_2$ processed clay, whereas the corresponding elongation at break was decreased when compared to equivalent nanocomposites with same fraction of as-received clay. We attribute the decrease of elongation at break to improved polymer-clay interaction in $scCO_2$ processed samples, and similar results had been reported that PP/clay nanocomposites involving a PP-g-MA compatibilizer usually have a low value of elongation at break [90]. The representative stress–strain curves within elastic-plastic transition reign for pure PET and PET/30B nanocomposites are enlarged in Figure 57 (B). Compared with pure PET, most of the nanocomposites demonstrated improvements in both tensile strength and Young's modulus, except for the sample with 1wt% of as-received clay. In addition, all nanocomposites showed that both tensile strength and Young's modulus increased with increase of filler content.
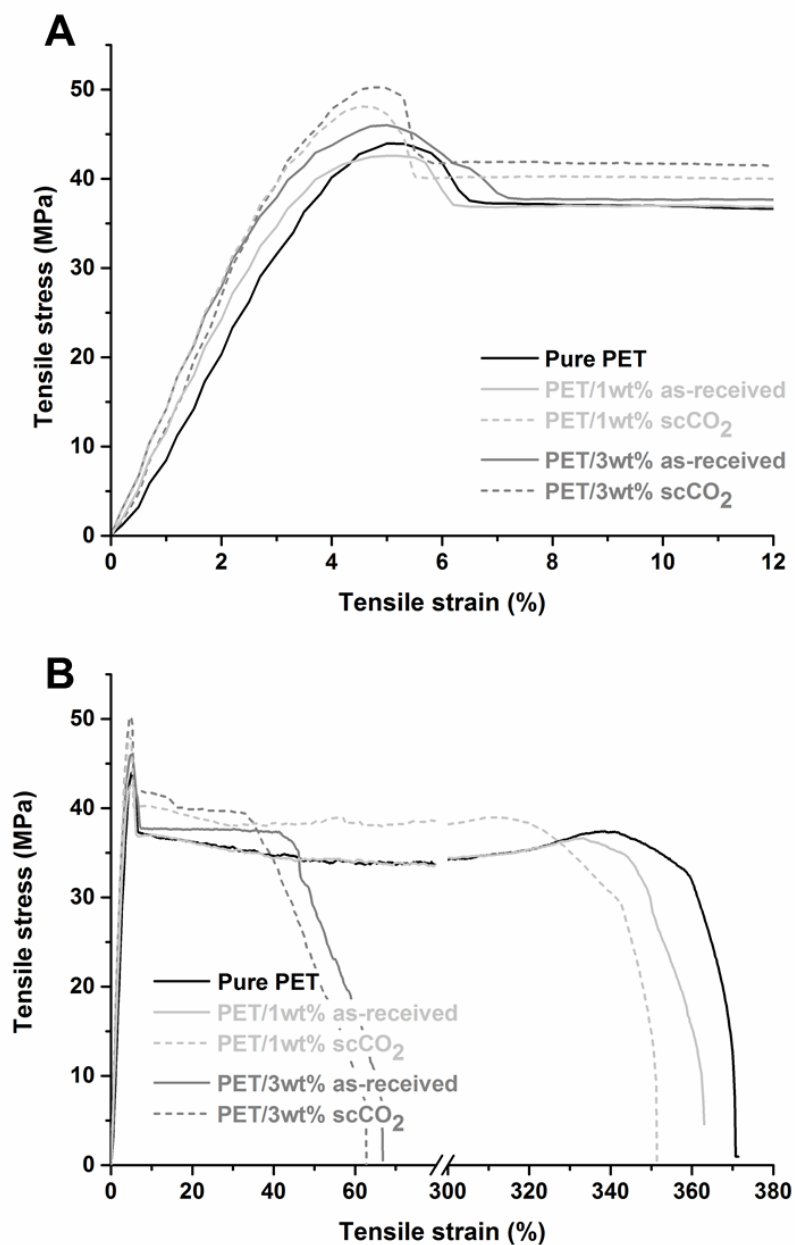
Figure 57 Typical stress-strain curves for PET and PET/30B nanocomposites. (A) Full strain range (B) enlarged for low strain range.

The morphologies of tensile fractures of all samples were obtained after tensile test to provide clues to the toughening mechanisms. The pure PET (Figure 58) displayed a ductile fracture profiles with smooth crack propagation indicating the homogeneous deformation of the matrix phase prior to fracture, in addition, the final shear fracture

displayed a 45° angle relative to the tensile direction. Nanocomposites with low clay fraction exhibited similar fracture profile as pure PET, whereas with increasing clay fraction to 3wt%, nanocomposites presented a brittle fracture profile because high elastic modulus of clay particles decreased the ductile properties. Moreover, the fractures were perpendicular to tensile direction with rough fracture morphology due to the clay particles deflecting crack propagation and offering resistance to the fracture process. Compared with as-received clay, $scCO_2$ processed samples demonstrated relatively greater brittleness, because the polymer-clay interaction was stronger in those cases than as-received clay reinforced samples, where the pull out of clay particles could improve the ductility [152]. Such an observation is well complemented by the enhancements in mechanical properties, as indicted from the increase in tensile strength and Young's modulus.
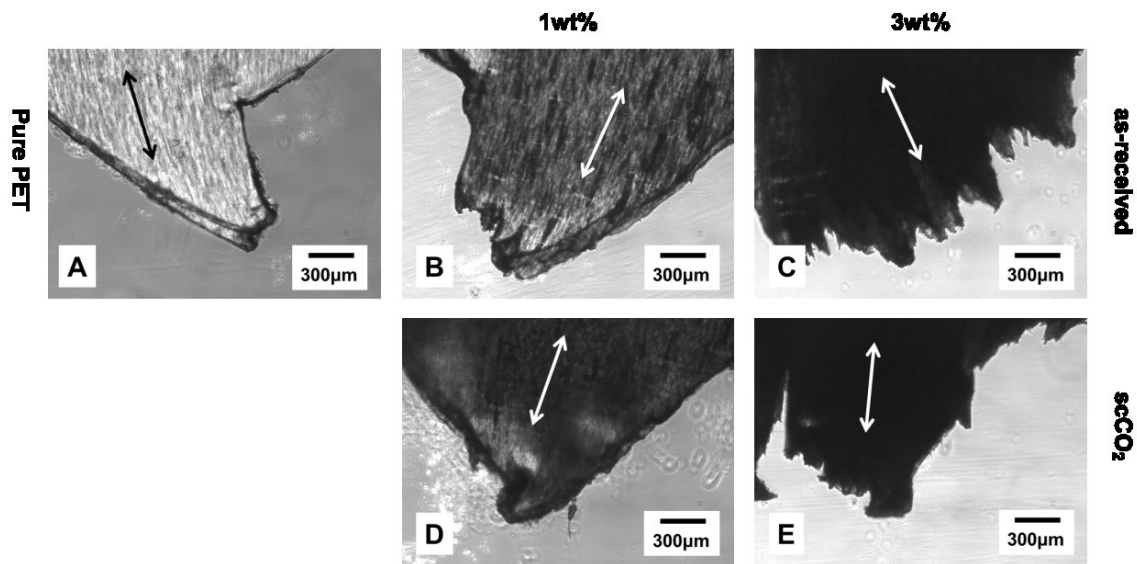
Figure 58 Digital micrographs of the fracture of tensile specimens (arrow indicate the tensile direction).

All of mechanical properties of the pure PET and PET/30B nanocomposites are summarized in Table 8. Both tensile strength and Young's modulus could be improved

132

either by adding scCO$_2$ processed clay which improved polymer-clay interaction and leaded to homogenous clay dispersion or by increasing the clay fraction. In comparison with scCO$_2$ processed clay, as-received clay displayed comparable improvements on Young's Modulus but with limited enhancement on tensile strength due to the large agglomerates of clay particles could serve as stress concentration site. The effects of scCO$_2$ processing on improving of mechanical properties are more significant at low clay fraction. With only 1wt% of processed clay, the tensile strength and Young's modulus were improved by 10.7% and 21.4% respectively. Moreover, the maximum improvements of tensile strength (12.1%) and Young's modulus (24.9%) were achieved by incorporating of 3wt% of processed clay.

Table 8 Mechanical properties and inorganic clay volume fraction of pure PET and PET/30B nanocomposites.

Sample	Tensile strength (MPa)	Increase (%)	Young's Modulus (MPa)	Increase (%)	Elongation at break (%)	Inorganic clay fraction (v%)
Pure PET	43.8±0.2	-	1230±16	-	369±6	-
PET/1wt% as-received 30B	43.2±0.8	-1.4	1357±44	10.3	359±4	0.333
PET/1wt% scCO$_2$ 30B	48.5±1.1	10.7	1493±39	21.4	354±2	0.333
PET/3wt% as-received 30B	46.1±0.7	5.3	1469±33	19.4	71±9	0.986
PET/3wt% scCO$_2$ 30B	49.1±1.4	12.1	1536±21	24.9	66±5	0.986

The measured moduli were compared with predictions by composite theory models to assess the effect of scCO$_2$ processing and clay fraction on improving

133

mechanical properties. Two models that are commonly used to estimate the properties of polymer composites are the Halpin-Tsai [148] and the Ji, et al. [153], models. Both models estimate the composite Young's moduli based on filler and matrix physical properties with different assumptions regarding to dispersion and orientation of the filler particles. Halpin-Tsai model assumes fully exfoliated and unidirectional clay platelets, which was expressed by the following equation:

$$E_C = E_m \left[\frac{1 + \xi \eta \phi_f}{1 - \eta \phi_f} \right]$$

Where,

$$\xi = 2(\frac{l}{t}) \quad \text{and} \quad \eta = \left[\frac{E_f / E_m - 1}{E_f / E_m + \xi} \right]$$

Where, E_f, E_m and E_c are the filler, matrix, and composite modulus, respectively. ϕ_f is the inorganic clay volume fraction and l/t is the aspect ratio of the clay particles. The Young's modulus of inorganic clay E_f was taken as 178 GPa [94] and the Young's modulus of matrix was measured to be 1230.2±16.4MPa , the aspect ratio of the silicate platelets (l/t) was reported in the range from 10 to 300 [39]. In our study, the volume fraction of inorganic clay of composites can be calculated from:

$$\phi_f = \frac{\phi_W \times (1 - W_{WLI}) / \rho_C}{\phi_W / \rho_{OC} + 1 / \rho_P}$$

Where, ρ_{OC}, ρ_C and ρ_P are the density of organic clay, inorganic clay and polymer matrix, respectively. The density of inorganic clay is 2.86g/cm^3 and the density of matrix is 1.37g/cm^3. ϕ_W is weight fraction of organic clay and W_{WLI} is weight loss of organic clay

on ignition which is 0.3 for Cloisite[®] 30B [39]. The calculated volume fractions of inorganic clay were given in Table 8.

The model developed by Ji et al. makes no assumption regarding to clay orientation, so it is valid for randomly oriented systems. Also, the model does not assume fully exfoliated clay particles. Ji's model can be described as follows:

$$\frac{1}{E_C} = \frac{1-\alpha}{E_m} + \frac{\alpha-\beta}{(1-\alpha)E_m + \dfrac{\alpha(k-1)E_m}{\ln k}} + \frac{\beta}{(1-\alpha)E_m + \dfrac{(\alpha-\beta)(k+1)E_m}{2} + E_m\beta}$$

$$\alpha = \sqrt{\left[2\left(\frac{\tau}{t_C}\right)+1\right]\phi_f}$$

$$\beta = \sqrt{\phi_f}$$

$$k = \frac{E_f}{E_m}$$

Where, all parameters have the same physical means as Halpin-Tsai meodel. τ is the thickness of the interphase region, taken to be the d-spacing (3.46 nm, WAXD) for nanocomposites in this study, and t_c is the thickness of individual clay layer, taken to be approximately 1 nm. Ji et al.'s model takes into account the interphase separation between clay particles without assumption about the state of intercalation or exfoliation. However, an exfoliated structure has been reported to be more desirable structure for improving mechanical properties [154].

Figure 59 presents the experimental and modeled results for Young's modulus of PET/30B nanocomposite as a function of clay aspect ratio and fraction based on the Halpin-Tsai model. It showed that the nanocomposites modulus can be dramatically enhanced by increasing clay aspect ratio or inorganic clay fraction. All of experimental

Young's moduli fall into the reasonably predicted range by using Halpin–Tsai model but displayed relatively low effective aspect ratio. This may be due to a lack of complete dispersion of clay as individual palates, lack of strong interactions between clay and the matrix and lack of complete orientation of the clay particles in the tensile direction. In comparison with nanocomposites reinforced by as-received clay, the corresponding nanocomposites with processed clay showed higher effective aspect ratio due to delaminate/exfoliate clay particles, nevertheless aggregation of clay particles inside as-received sample could reduce the amount of reinforcement that the clays can provide, resulting in less enhancement of the Young's modulus [93]. The Ji, et al., model predicted an intercalated structure with an improvement in Young's modulus. Most of the experimental values were lower than the model prediction because clay layers maybe not fully intercalated by the polymer chains due to severe aggregation. However, nanocomposites with 1wt% processed clay showed significantly larger value than the prediction. The reason for this could be forming an exfoliated structure inside this sample and the observation is well consistent with WAXD results.
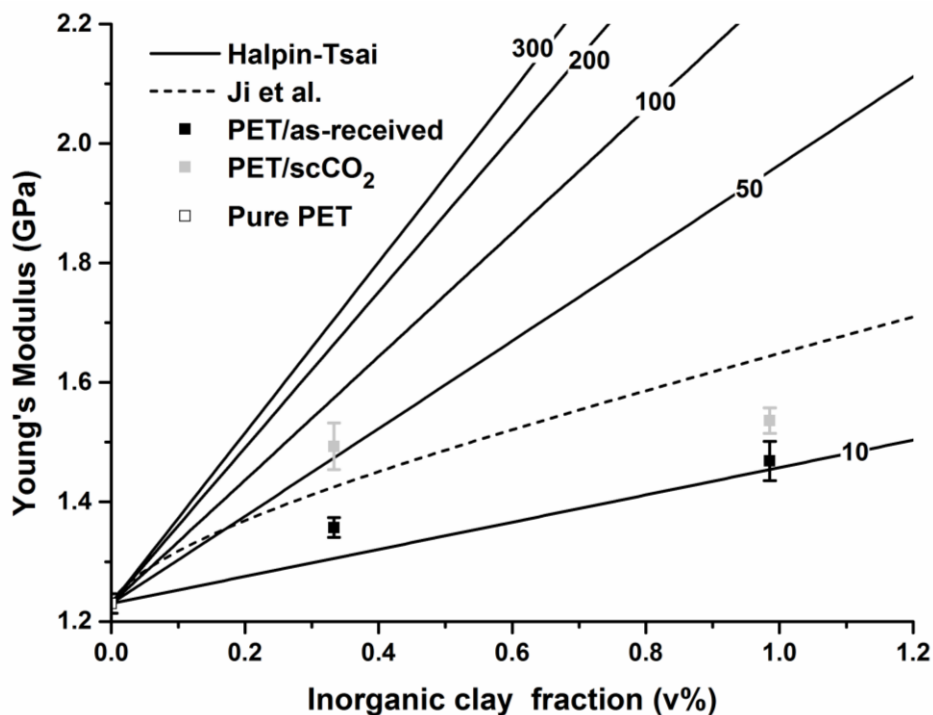
Figure 59 Experimental Young's moduli of PET/30B nanocomposites and comparison with theoretical predictions.

Figure 60 presents the DSC cooling and re-heating cycles for pure PET and PET/30B nanocomposites. In comparison with pure PET, incorporation of clay significantly changed the thermal behaviors of PET matrix. During the rapidly cooling cycle, pure PET displayed a relatively weak crystalline peak around $152.6^{o}C$ due to its slowly crystallizing rate, whereas all of the nanocomposites exhibited distinct crystalline peaks with shifting to higher temperature. Conversely, for the re-heating cycle, pure PET demonstrated a notable crystalline peak around $139.4^{o}C$, however no distinct crystalline peaks were observed for all nanocomposites and their melting peaks slightly shifted to higher temperature than that of pure PET. The significant changes of crystalline behavior were attributed to the heterogeneous nucleating effect of clay particles, as which were

incorporated into PET matrix and provide a large interfacial area and serve as heterogeneous nucleating sites that facilitate crystallization of the matrix. Similar phenomena have been reported by other researches and further study found that the crystallization rates of PET/clay nanocomposites were increased significantly [149]. The crystallinity of the samples before re-heating could be calculated from the enthalpy of melting ΔH_m and the enthalpy of crystallization ΔH_{hc} obtained from the re-heating cycle by applying the following equation:

$$\chi_c = \frac{(\Delta H_m - \Delta H_{hc})/w_{PET}}{\Delta H^0}$$

where W_{PET} is the PET weight fraction and ΔH^0 is the enthalpy of melting of 100% crystalline PET (140 J/g) [150]. The higher crystallinities of nanocompsoites summarized in table 9 confirmed that the presence of clay enhanced crystallization of PET.
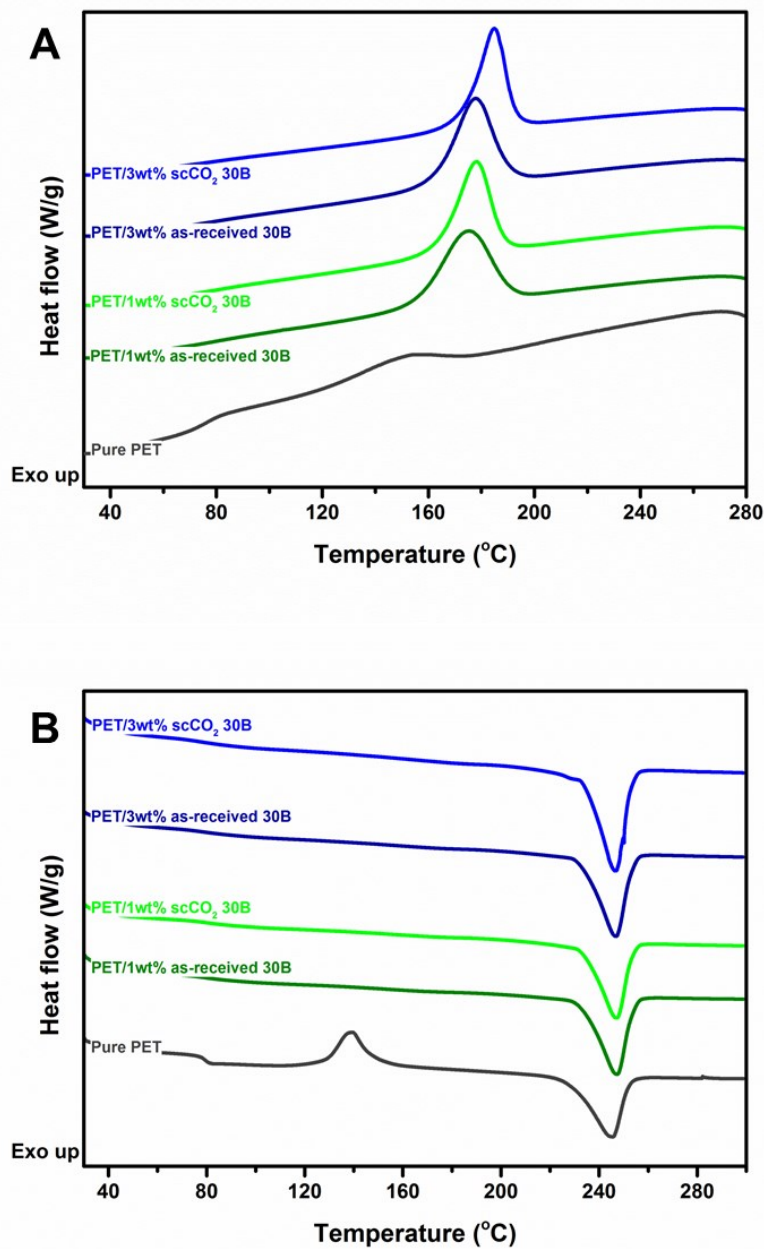
Figure 60 DSC Curves of neat PET and PET/30B nanocomposites A. cooling B. re-heating.

Table 9 also reports the effects of scCO$_2$ processing and clay fraction on cooling

crystallization temperature, T$_{cc}$, enthalpy of cooling crystallization, ΔH$_{cc}$, glass transition

temperature, T_g, melting temperature, T_m, enthalpy of re-heating crystallization, ΔH_{hc} and enthalpy of melting, ΔH_m of PET. With an increase in clay fraction or improvement of clay dispersion by $scCO_2$ processing, the T_{cc} of nnanocomposites significantly shifted to higher value and corresponding enthalpy increased slightly, those phenomena could attribute to the increase of heterogeneous nucleating sites. Comparing nanocomposites with as-received clay, the crystallization peaks of $scCO_2$ processed samples became narrow and sharp, which might be caused by the improved homogenous dispersion of clay. All of nanocomposites with as-received clay demonstrated slightly increase of T_g as compared with pure PET, whereas, no distinct shifts were observed for $scCO_2$ processed samples. The slightly higher T_g for as-received clay reinforce sample can be attributed to large amount of polymer intercalated between platelets and/or the presence of larger clay particles which could confine and/or block the movement of polymer chains, respectively [50, 151]. This result is in good agreement with previous research that showed increase of Tg in intercalated polymer/clay nanocomposites, whereas, exfoliated clay particles had limited effect on chains movement. In addition, the rest of thermal properties of all nanocomposites failed to reveal any variation as function of clay loading or $scCO_2$ processing, indicating that the increase of heterogeneous nucleating sites and improvement of their uniformly distribution have very little effects on re-crystallization and meting process of PET matrix. On the basis of DSC data, $scCO_2$ had achieved improved dispersion of clay with delaminated structure and uniform distribution, which is highly consistent with what we have seen in previously structural characterizations.

Table 9 Thermal properties of pure PET and PET/30B nanocomposites.

Sample	Cooling		Re-heating				
	T_{cc} (°C)	ΔH_{cc} (J/g)	T_g (°C)	T_m (°C)	ΔH_{hc} (J/g)	ΔH_m (J/g)	Crystallinity (%)
Pure PET	152.6	4.9	79.7	244.9	16.4	34.8	13.1
PET/ 1wt% as-received 30B	173.8	41.9	83.2	247.0	0	42.6	30.7
PET/ 1wt% scCO$_2$ 30B	177.6	43.5	80.1	247.0	0	42.2	30.4
PET/ 3wt% as-received 30B	177.2	45.2	83.4	246.7	0	42.8	31.5
PET/ 3wt% scCO$_2$ 30B	184.7	50.8	78.5	246.5	0	43.5	32.0

Figure 61 presents the oxygen permeation values of pure PET and clay reinforced nanocomposites as functions of scCO$_2$ processing, clay fraction and temperature. Oxygen permeation rate of the pure PET displays a dependence on temperature which is consistent with the well-known phenomenon whereby temperature affects the diffusivity and solubility of the permeant in polymer. With the increase in temperature, the oxygen permeation rate increased due to the increase of diffusivity of oxygen through PET. Consistent with the behavior of pure PET, increasing the temperature of oxygen permeation analysis also caused exponential increase in oxygen permeations of all nanocomposites. An exceptional increase of permeation in nanocomposite with 1wt% as-received clay was observed under 33°C which may be defects caused by the ununiformed distribution of clay particles. As expected, incorporation of impermeable clay particles into PET could both lower the solubility (decreasing organic phase) and effective diffusivity (creating tortuous pathways) of a permeant, which in turn decreases the permeation. Permeation data reported here demonstrated that increasing the clay fraction could further decrease permeation, and in comparison of sample with as-received clay at

the same clay loading, scCO$_2$ processed clay leads to better clay dispersion and distribution which could produce further improvements in barrier properties [144]. In particularly, at 23 ^{o}C, with 1wt% ofpre-dispersed clay leads to a significant reduction of oxygen permeation (~33%) compared to as-received clay (~8%). A maximum reduction (44%) of oxygen permeation was achieved by adding only 3wt% of pre-dispersed clay, indicating even within short melting processing time, in-situ dispersed clay could achieve significant improvement on barrier properties with only small amount of clay and absence of additives, however limited success on improving PET barrier properties had been reported without helping of additives [95].
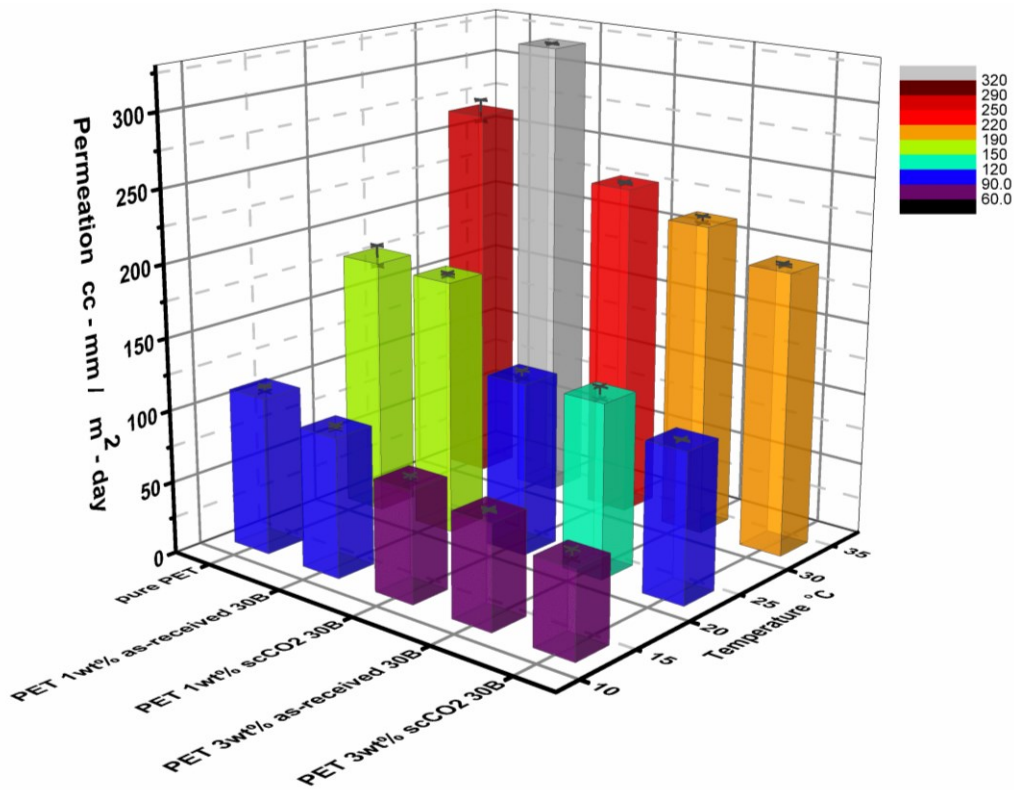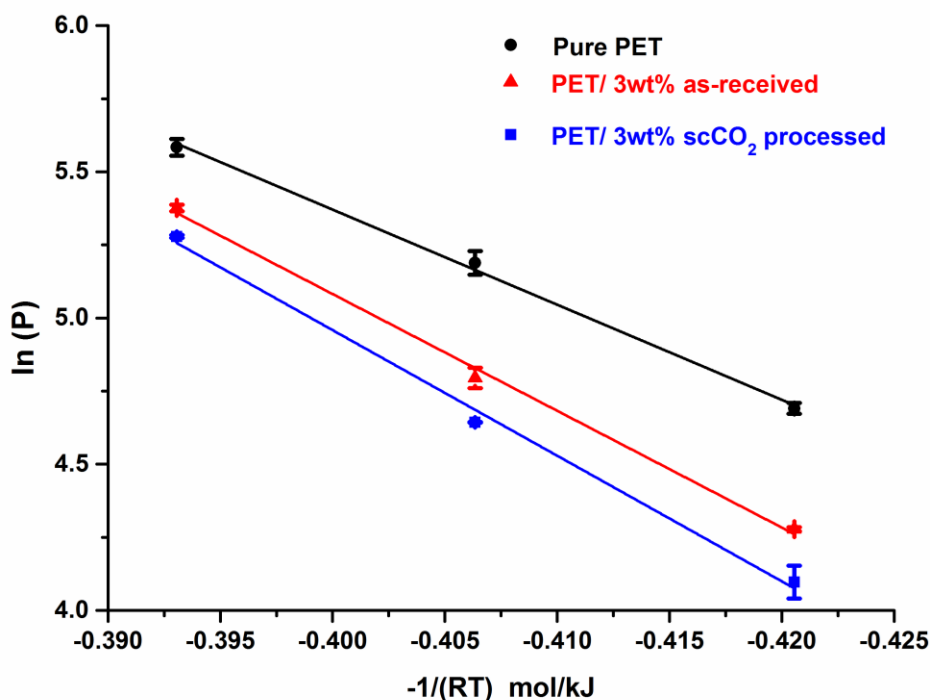

Figure 61 Oxygen permeations of pure PET and PET/30B nanocomposites at different temperatures.

The oxygen permeation data of three samples, pure PET and nanocomposites with 3wt% as-received or scCO$_2$ processed clay, tested at different temperatures were fit to the Arrhenius relation where temperature dependence of the permeation was expressed by the following equation:

$$P = P' e^{-E_P/RT}$$

Where P' is the exponential prefactor (measured in cc-mil/(m^2-day)), E$_P$ is the activation energy for permeation (in kJ/mol), R is the gas constant (8.314 J/ (mol-K)) and T is the absolute temperature (K) [155]. Figure 62 shows Arrhenius plots of the temperature dependence of the oxygen permeation for pure PET and PET/30B nanocomposites. Interestingly, all of samples showed well observing the above relationship within the tested temperature range, even with the present of clay particles, indicating that nanocomposites follow the well-known phenomenon whereby temperature affects diffusivity and solubility of a permeant through polymer. Therefore, it is reasonable that the curves for nanocomposites are well below that of pure PET due to both diffusivity and solubility were lower by incorporation of clay. Likewise, it is logical that the curve for scCO$_2$ processed nanocomposite is well below that of sample with as-received, given the expectation that improved clay dispersion could further decrease the diffusivity of the permeant. It should be noted that, however, modifiers on the clay surface possessing distinct chemical and physical properties compared with matrix could change permeant solubility. In particular, short modifier chains might also experience thermal transition within the testing temperature range where pure PET did not and would be expected to result in increase of permeant diffusivity, whereas no evidences of such changes were seen in figure 8. Therefore, nanocomposites exhibited

143

same behavior as the pure PET did in tested temperature range may indicate that small amount of modifier had limited effect on oxygen solubility and diffusivity, and may expected to show similar temperature dependent behavior as the permeable matrix phase, whereas the different slopes clearly reflected differences in the effective activation energies associated with detours permeation through these materials.

Figure 62 Arrhenius plots of temperature dependence of the oxygen permeation in pure PET and PET/30B nanocomposites.

The Arrhenius model semi-qualitatively captures the temperature dependence of permeation over the temperature range investigated, and the fitting parameters are summarized in Table 10. Permeation shows Arrhenius behavior as reflected by the correlation coefficients (0.992–0.996). The activation energies of permeation associated with pure PET and PET/clay nanocomposites were determined from the slope of semi-

logarithmic plots of the permeation against the reciprocal of the absolute temperature. The E_P for the pure PET used in this work was calculated to be 32.5 ± 1.5 kJ/mol, similar to the literature values [156, 157]. By contrast, PET/clay nanocomposites with as-received or $scCO_2$ processed clay resulted in significant increases of E_p values and improved clay dispersion by $scCO_2$ processing could further enhance the effect, indicating that the oxygen permeation was no longer solely a function of permeation through PET but was presumably a function of permation through a more tortuous path. It is impossible to separate contributions from sorption and diffusion based on current tests, but these results support the conclusion that the effect of temperature on the barrier properties of polymer/clay nanocomposites depends both on the Arrhenius behavior of the organic phases and detour effects induced by the clay particles [24].

Table 10 Fitted Arrhenius parameters for pure PET and PET/30B nanocomposites.

Samples	Exponential prefactor (cc-mil/(m²-day))	Activation energy (kJ/mol)	r²
Pure PET	9.58×10^7	32.5 ± 1.5	0.996
PET 3wt% as-received 30B	1.39×10^9	39.9 ± 2.1	0.994
PET 3wt% scCO₂ 30B	4.09×10^9	42.9 ± 2.7	0.992

As shown in Figure 63, the pure PET film exhibited high transparency and clarity. Although a slight discolor was observed with the incorporation of clay or increase of clay fraction, all the nanocomposites maintained the high transparency of the pure PET. The reason for discolor could be the degradation of the modifier on the clay surface since the melting extrusion temperature is 265°C while the temperature of maximum weight lose peak for 30B is 274°C. In comparison with nanocomposites reinforced by as-received clay, the nanocomposites with processed clay exhibited slightly improvement on optical

clarity of the nanocomposites, which might primarily resulted from both the exfoliated structure of the clay layers and the efficient dispersion of the clay particles in the PET matrix as evidenced by the XRD and TEM results. In other words, these images confirm that the presence of clay only slightly affected the transparencies and clarity of the nanocomposites.

Figure 63 Optical images of pure PET and PET/30B nanocomposites films (thickness ~0.2mm).

4.3.3 Permeation of HDPE/clay Nanocomposites

Series clays with different clay modification were melting compounded with high density polyethylene (HDPE) to intentionally study the effect of clay modification on improving HDPE's barrier properties. Figure 64 shows the transmission rate of oxygen for pure HDPE and clay reinforced nanocomposites, all nanocomposites displayed decreases of transmission rate compared with pure polymer, even the hydrophilic 30B reinforced nanocomposites achieved a 14.6% reduction in transmission rate. The best reduction (~20.5%) was achieved by using scCO$_2$ processed 20A, and a moderated

146

reduction of 18.4% was achieved by using 10A. Although detailed structural characterizations (WAXD and TEM) of HDPE/clay nanocomposites were not available in this section, we still can conclude that the incorporation of clay could decreased the oxygen transmission rate of HDPE and the improved reinforcements follow the trend that 20A>10A>30B. Based on the chemical structures of clays provided in table 1 and the chemical structure of HDPE, we summarized that HDPE has the best interaction with 20A because of the similar chemical structure and followed by 10A and 30B, because 10A and 30B are hydrophobic and hydrophilic respectively. In addition, $scCO_2$ processing lead to further decrease of transmission rate due to the improved clay dispersion and polymer-clay interfaces.
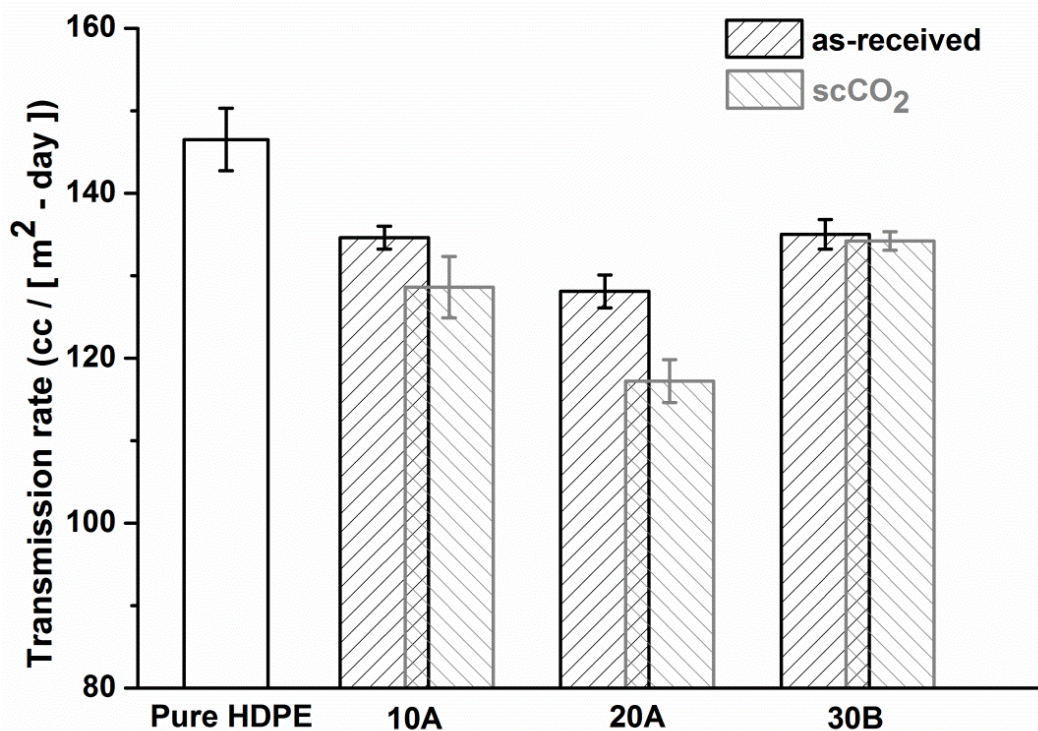

Figure 64 Oxygen permeations of pure HDPE and HDPE/clay nanocomposites.

4.3.4 Discussion

In this chapter, we followed the concept built in previous chapter and tried to improve barrier properties of engineering polymers such as PET and HDPE by dispersing clay particles with help of scCO$_2$. However, unlike what we have expected, two significant deviations were observed from the concept we got from PS when applying it to PET and HDPE.

Firstly, we found that incorporation of clay particles could not always result in reduction of barrier properties in PET and the clay modification played a very important role in improving barrier properties of polymer/clay nanocomposites. In general, stronger polymer-clay interaction leads to better improvement in barrier properties and poor polymer-clay interaction may increase the permeation of gas molecule by forming ineffective surface for them to pass-by. In particular, the improvements of barrier properties for PS/clay nanocomposites follow the order that: 10A>20A>30B; for PET/clay nanocomposites follow the order that: 30B>10A>20A, where in the case of 20A, the permeation was enhanced, and for HDPE/clay nanocomposites follow the order that: 20A>10A>30B.

In order to support the claim, FTIR spectrums of 30B, pure PET and PET/30B nanocomposites were measured to confirm the existence of strong polymer-clay interaction. As shown in figure 65, a sharp O-H stretching band was observed around 3630cm^{-1} due to the present of free hydroxyl group in 30B, in contrast, due to the hydrogen bonding in PET, the O-H stretching band became broaden and shift to lower wavenumber around 3430cm^{-1}. The carboxylic acid group C=O stretching band also exhibited at around 1680cm^{-1}. As 30B was compounded with PET, the O-H stretching band due to free hydroxyl group was vanished, and the O-H stretching band of hydrogen

bond was observed, indicating that 30B formed hydrogen bonds with PET molecules, which is a type of strong secondary bond than provide strong interaction between PET and 30B.
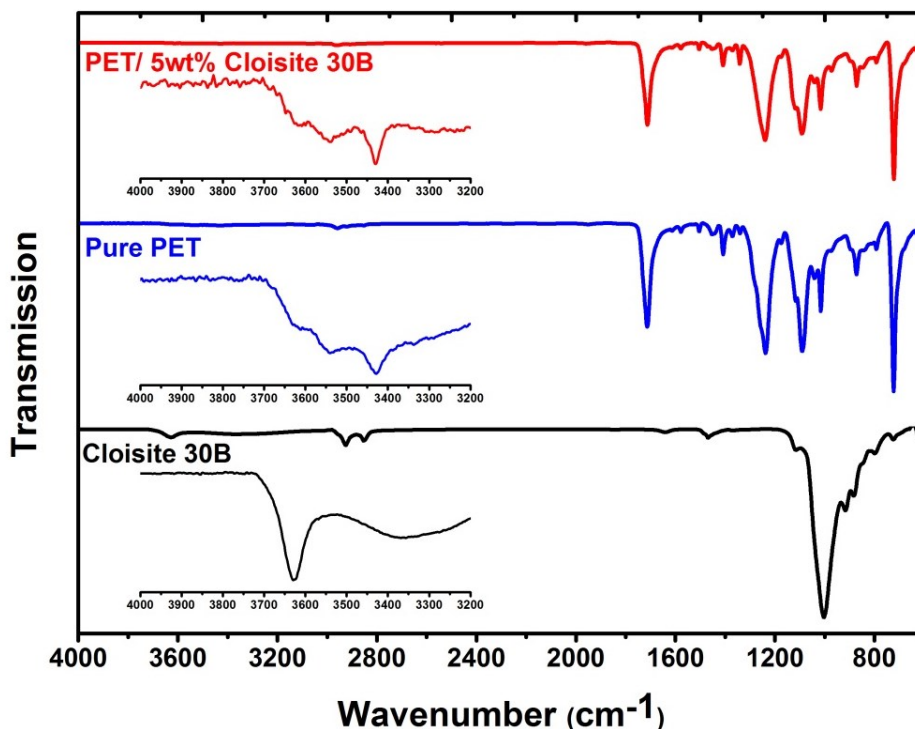
Figure 65 FTIR spectrums of 30B, pure PET and PET/30B nanocomposites.

Secondly, we found that for PET, increasing clay fraction or improving clay dispersion could not continuously or constantly decrease the permeation of the nanocomposites, especially at higher clay fraction, which was conflict with what we have observed in PS case. We attributed the deflection to the combinational effect of elevated processing temperature, low thermal stabilities of organic clays and excessive clay loading. We speculated that the relatively high processing temperature could cause the degradation of clay modifiers with poor thermal stabilities, which has been confirmed by

observed discolor in all of nanocomposites. The degradation of modifiers could harm the polymer-clay interaction and render a poor polymer-clay interface, which could combine with the high clay loading to form express channels inside nanocomposites for gas molecules. It has been reported that high clay loading caused low level of clay dispersion or aggregation. Those channels could facilitate the diffusion of gas molecule through the film and decrease the barrier properties dramatically.
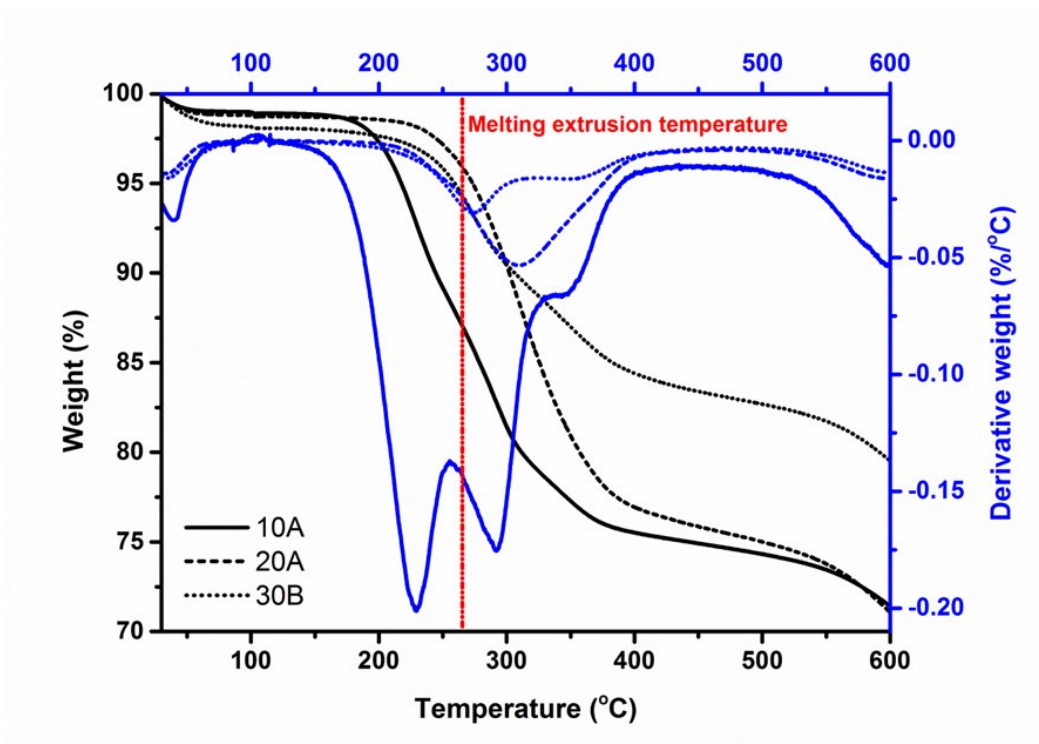
Figure 66 TGA curves of 10A, 20A and 30B.

Figure 66 compares the thermal stabilities of the clay used in this research with the processing temperature. As shown in the figure, the melting extrusion temperature was 265°C, whereas the temperatures of maximum weight lose peak for 10A, 20A and 30B were 228.5 ^{o}C, 310°C and 274°C respectively. Moreover, all of the organic clays had initial decomposition temperatures lower than the processing temperature, which provide sufficient evidence that poor polymer-clay could happen and harm barrier properties,

especially at higher clay fraction. Therefore, in order to further improve barrier properties, both enhancing polymer-clay compatibility and improving thermal stability of clay are important.

4.4 Conclusion

Melting extrusion was used to prepare a series of poly (ethylene terephthalate) (PET)/clay and high density polyethylene (HDPE)/clay nanocomposites without the present of co-solvents or additives and post-processing treatment. The effects of clay modification and fraction and $scCO_2$ processing on structural, mechanical, thermal and barrier properties of nanocomposites were investigated by using WAXD, TEM, rheology, Instron tester and oxygen permeation.

Various types of commercial clays were pre-dispersed by supercritical carbon dioxide ($scCO_2$) and directly melting compounded with Poly (ethylene terephthalate) to identify the best candidate for improving barrier properties of PET and HDPE. WAXD and TEM results of resultant nanocomposites confirmed that PET had penetrated into the clay inter-galleries and the pre-dispersed clay lead to improved homogeneously clay dispersion. Rheological results indicated that 10A and 20A formed network structure while 30B did not. Young's modulus were improved by adding clay particles, moreover improved clay dispersion lead to more significant improvement and maximum improvements of 34.8% was achieved by incorporating of 5wt% processed 10A. DSC results indicated well dispersed clay particles could serve as nucleation sites to increase the crystallinity, in addition, the crystallization temperature during cooling cycle shifted to higher temperature either by improving polymer-clay interaction or dispersion and 30B show the best PET-clay interaction. Unlike what we have expected, incorporation of clay

151

particles (type and loading) does not always lead to improvement in barrier properties. Strong polymer-clay interaction determines the extent of improvements in barrier properties, maximum reduction of permeation (22.6%) in PET was achieved by adding 5wt% of processed 30B and reduction of permeation (20.5%) in HDPE was achieved by using 5wt% of processed 20A.

30B was identified as the best candidate to improve PET barrier properties and was incorporated with PET at various clay fractions. WAXD and TEM results of resultant nanocomposites confirmed that PET had penetrated into the 30B inter-galleries and the pre-dispersed 30B lead to improved homogenous clay dispersion and polymer-clay interaction. Compared with as-received 30B reinforced samples, scCO$_2$ dispersed nanocomposites showed further enhancement on mechanical, crystalline and barrier properties with preserved transparency. Both tensile strength and Young's modulus were improved and maximum improvements of 12.1% and 24.9% respectively were achieved by incorporating of 3wt% processed 30B. DSC results indicated well dispersed 30B particles could serve as nucleation sites to increase the crystallinity, in addition, the crystallization temperature during cooling cycle shifted to higher temperature as improving of dispersion. Under 23°C, with only 1wt% of clay, pre-dispersed 30B lead to a more significant reduction of oxygen permeation (~33%) than as-received clay did (~8%) and a maximum reduction (44%) of oxygen permeation was achieved by adding 3wt% of pre-dispersed clay. Moreover, we confirmed that effect of temperature on the permeation of PET/30B nanocomposites depended both on the Arrhenius behavior of the organic phases and tortuous path effects, where improved clay dispersion resulted in a higher effective activation energy.

CHAPTER 5: OVERALL CONCLUSIONS

5.1 scCO$_2$ processing of clay

Results based on the clay processing with scCO$_2$ suggest that:

(1)   scCO$_2$ processing enables pre-dispersion of organic modified clays regardless what kind of modifier on them.

(2)   the degree of dispersion of different kind of clays actually is a competitive result between CO$_2$-philicity and modifiers interaction, which means stronger CO$_2$-philicity and weaker modifier interaction result in better pre-dispersion.

(3)   scCO$_2$ processing did not remove surface modifiers from nano-clays which kept the good solubility of clay in organic solvent and the compatibility to organic phase (based on TGA results).

(4)   the expanded flexible and puffy structure of the scCO$_2$ processed clays (as shown in figure 67) exposed more of the available surface area and should be easier to disperse into a polymer matrix than the as-received clay.
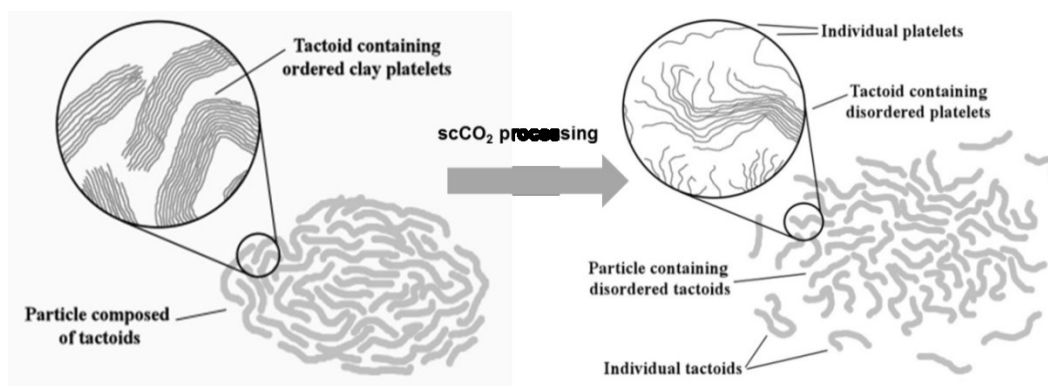

Figure 67 Schematic structure evolution of clay upon scCO$_2$ processing.

5.2 Effects of scCO$_2$ processing on clay dispersion, polymer-clay interaction and barrier properties

Our studies of scCO$_2$ processing on structural and barrier properties of PS/clay, PET/clay and HDPE/clay nanocomposites, suggest that:

(1)   scCO$_2$ processing result in improved clay dispersion by exfoliating the clay layers from the tactoids, in addition, the processed clay lead to more homogenous clay dispersion due to break down large clay particles. The improved homogenously clay dispersion could effectively increase the effective aspect ratio which in turn improves the barrier properties of resultant nanocomposites as shown in figure 68.

Figure 68 Schematic illustration of improved clay dispersion by scCO$_2$ processing.

(2)   scCO$_2$ processing results in improved polymer-clay interface due to scCO$_2$ processed clay exposed more available surface to polymeric matrix and the exfoliated structure formed strong polymer-clay interaction. The improved polymer-clay interface could effectively increase the effective aspect ratio which in turn improves the barrier properties of resultant nanocomposites as shown in figure 69.
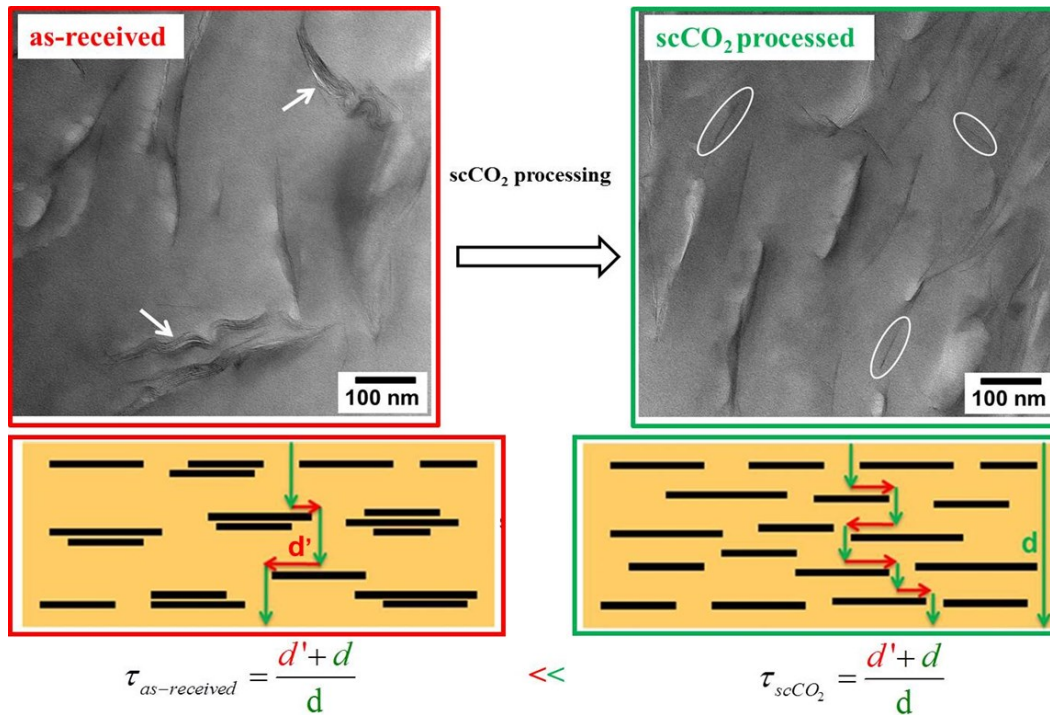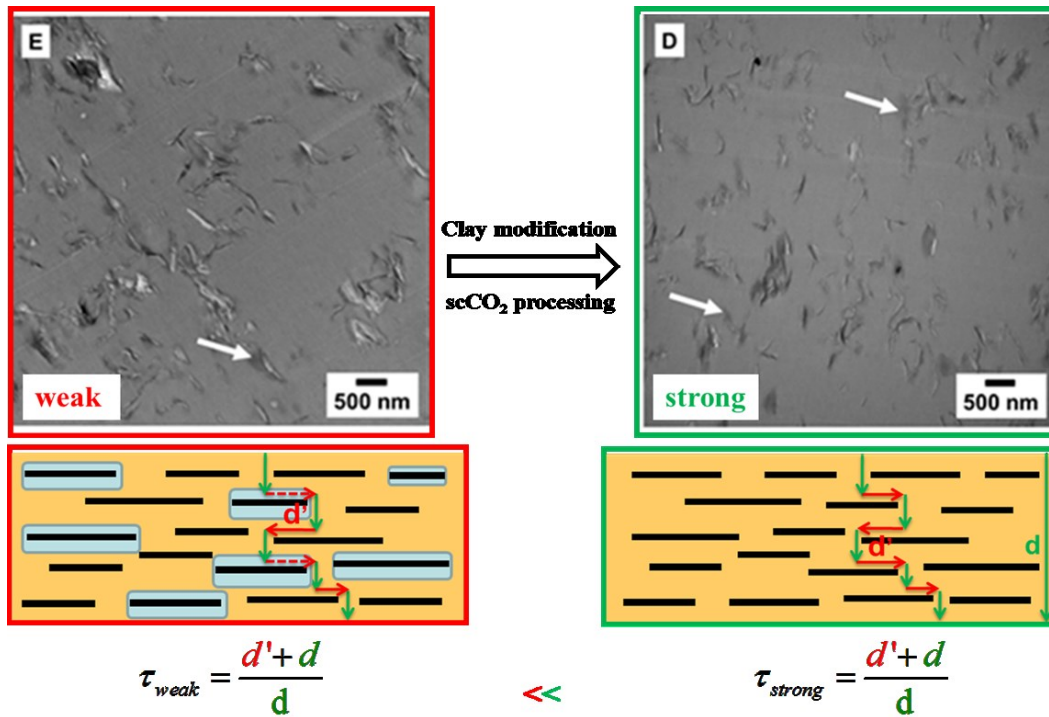

$$\tau_{weak} = \frac{d'+d}{d} \qquad << \qquad \tau_{strong} = \frac{d'+d}{d}$$

**Figure 69 Schematic illustration of improved polymer-clay interaction by scCO$_2$ processing.**

5.3 Effect of polymer-clay interaction on clay dispersion

Many simulation methods have been conducted to predicate clay particles dispersion in polymeric matrix. By tuning the polymer-filler interaction, homogeneous filler dispersion exists just at the intermediate interfacial interaction. Strong or weak

particles-polymer interactions both could lead to aggregation, due to an entropic depletion effect or local bridging of filler via polymer chains as shown in figure 70.

Polymer-clay interaction	Increase		
Clay dispersion			
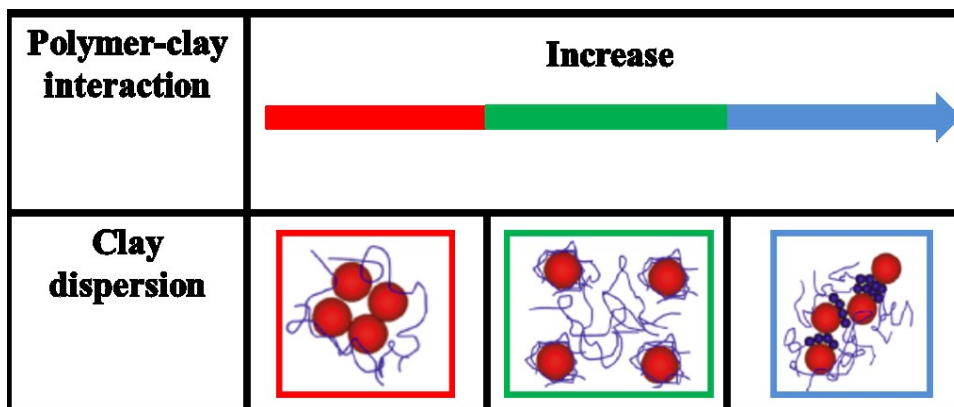
Figure 70 Relationship between polymer-clay interaction and clay dispersion [111].

Based on the investigations of structural properties of PS/clay and PET/clay nanocomposites, we find that:

(1)   in PS/clay nanocomposites, the dispersion of clay particles follow the trend that 20A>10A>30B.   Because 10A has a benzene ring functional group that can share electrons with benzene ring from PS, whereas 30B is hydrophilic that is incompatible with hydrophobic PS as shown in figure 71.

(2)   in PET/clay nanocomposites, the dispersion of clay particles follow the trend that 10A>20A>30B.   Because 30B has a hydroxyl functional group that can form hydrogen bond with PET molecules, whereas 20A is nonpolar molecules that has low compatibility with polar PET molecules as shown in figure 71.
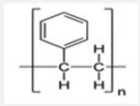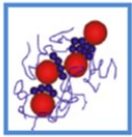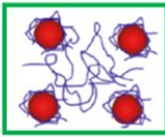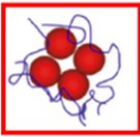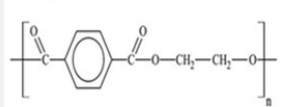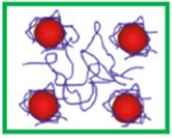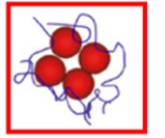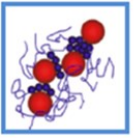
Clay / Polymer	10A CH_3 $CH_3 - N^+ - CH_2 - \bigcirc$ HT	20A CH_3 $CH_3 - N^+ - HT$ HT	30B CH_2CH_2OH $CH_3 - N^+ - T$ CH_2CH_2OH
PS			
PET			

Tallow (HT or T):
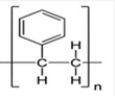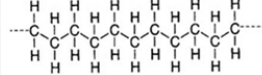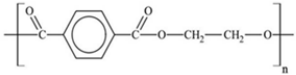
Figure 71 Schematic illustration of effect of polymer-clay interaction on clay dispersion.

5.4 Effect of polymer-clay interaction on barrier properties

Based on the study of barrier properties of PS/clay, PET/clay and HDPE/clay nanocomposites, we observed that:

(1)   beside clay dispersion, the polymer-clay interaction or polymer-clay compatibility also plays a very important role in improving matrix's barrier properties, because the strong polymer-clay interaction could form effective interface that in turn can increase the detour factor.

(2)   the maximum improvements in barrier properties of PS, HDPE and PET were achieved by using 10A, 20A and 30B respectively due to strong polymer-clay interactions as shown in figure 72.

Figure 72 Schematic illustration of effect of polymer-clay interaction on barrier properties.

CHAPTER 6: FUTURE WORK

Based on my previous research, in order to further improve barrier properties of PET by using clay reinforced nanocomposites, two important aspects need to be considered for future work- improving thermal stability of the reinforcement (inorganic and organic clay) and enhancing the PET-clay interaction and compatibility.

6.1 scCO$_2$ processing of natural clays

As have been mentioned above, it could be a breakthrough for high temperature melting compounding of PET/clay nanocomposites, if superior dispersion can be achieved even without modification. Therefore, we utilized scCO$_2$ to process natural clays by modifying our processing method. We used a stirring system to do a dynamic processing rather than a quiescent one. Adding stirring to the scCO$_2$ process enabled the natural clay platelets to fully contact supercritical phase, which could allow the supercritical CO$_2$ to diffuse into the inter gallery spaces. During depressurization, the trapped and saturated carbon dioxide will escape and lead to clay dispersion. We switched our processing parameters from the previous experiments (80°C, 2500psi, 4 h) to a new sets (50°C, 2500psi, 2h), which can result in higher density change. From the phase diagram of carbon dioxide we found that old condition corresponding to a processing density about 0.5g/cm^3, while the new condition corresponds to a higher density of 0.7g/cm^3. The new parameters give further dispersion to natural clay due to a bigger density change.

Two types of natural clay, Na$^+$ and Ca^{2+} balanced montmorillonites have been dispersed by scCO$_2$ with above processing conditions. SEM was employed to directly image the pristine clay powders to better visualize the change of original microstructure

and morphology of the clay particles and tactoids upon scCO$_2$ processing and WAXD was conducted to determine the change of inter-gallery spacing of the clay.
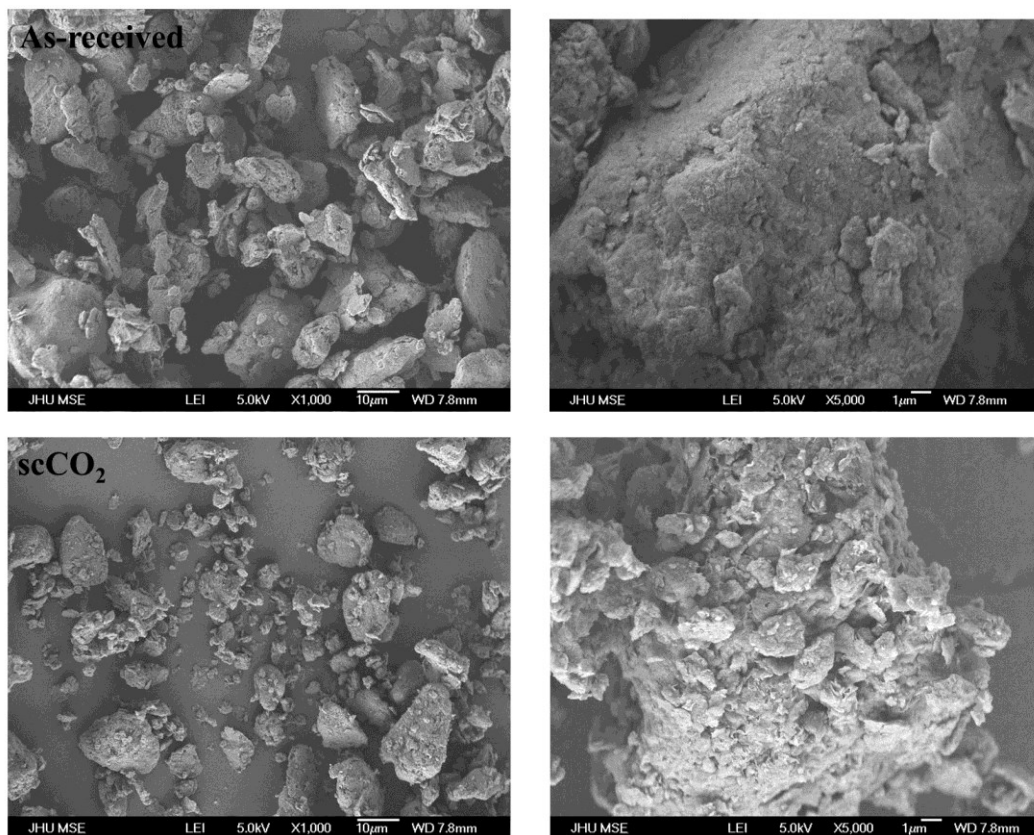
Figure 73 SEM images of Na$^+$ balanced montmorillonite before and after scCO$_2$ processing.

The SEM images of Na$^+$ balanced montmorillonite (Figure 73) before and after scCO$_2$ processing shows certain dispersion of natural clay. The particle size ranged from 5 to 20μm, and at high magnification a relatively tight particle structure was observed. The tactoids that formed particles have lateral dimensions of 1-3μm. Images of scCO$_2$ processed Na$^+$ montmorillonite revealed a significant change of micro morphology from the as-received nanoclay. We found that the diversity of composition was preserved, nevertheless, the dispersity of those structures decreased and more single tactoids with lateral dimensions of 1-3μm were observed. The particle size decreased to a range of 3-

12µm. At a higher magnification, loose tactoid-packed particles were observed. Similar results were also observed in SEM images of Ca^{2+} balanced montmorillonite (Figure 74). The as-received Ca^{2+} montmorillonite also showed a diversity of composition and high dispersity of micro structures, in which the particle size was in a range from 5 to 15µm. At a high magnification, a tight particle structure was observed but the packing was relatively loose when compared to Na^{+} montmorillonite. After scCO₂-processing, Ca^{2+} montmorillonite show a significantly changed morphology, where a significant amount of single tactoids with lateral dimensions of 1-3µm was observed. Moreover, at a higher magnification, cabbage-like tactoid clusters were observed.
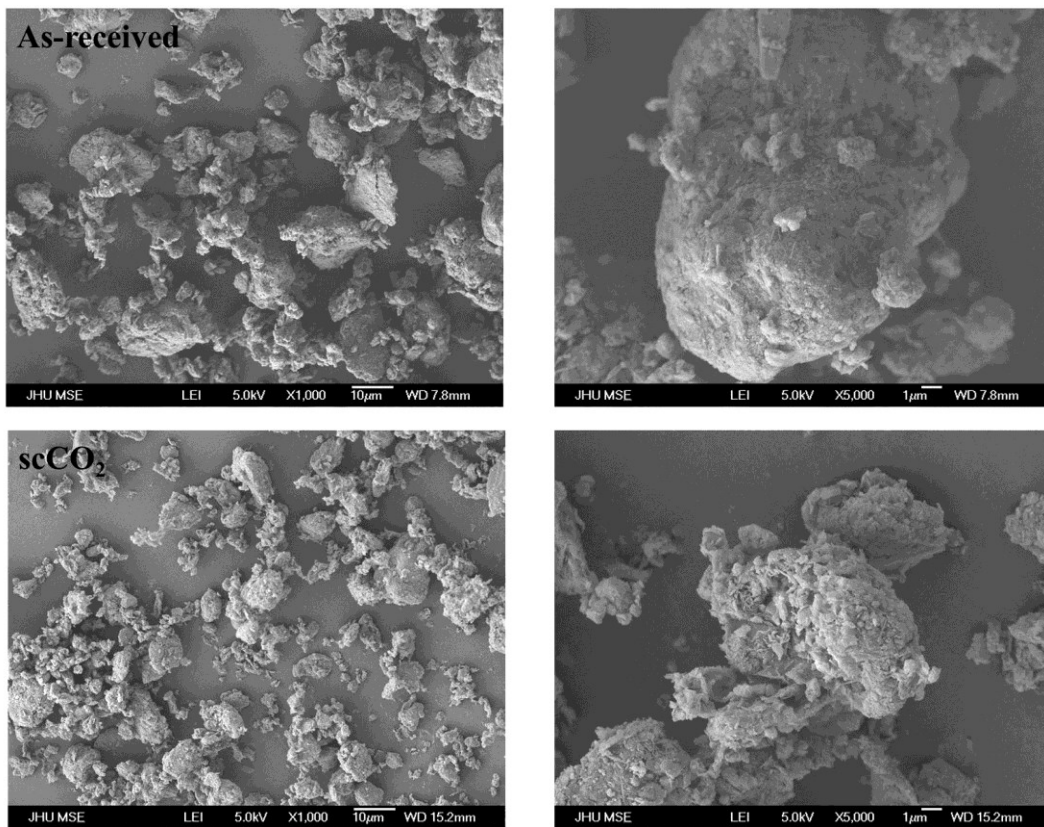
Figure 74 SEM images of Ca^{2+} balanced montmorillonite before and after scCO₂ processing.

Our results suggest that, upon depressurization, large particles are broken down into tactoids and a fraction of the outermost layers is delaminated from the tactoids during CO_2 expansion while the much less mobile inner layers just lose the initial coherence. It is reasonable to speculate that the puffy and expanded flexible structure of the $scCO_2$-processed clay contains many individual platelets and will exposes more of the available surface area, which should be easily accessible by organic modifiers or matrix molecules, leading to improved modification or dispersed nanocomposites.

WAXD was used to determine how the nano spacing between clay platelets changed during processing. The X-ray diffraction patterns of Na^+ and Ca^{2+} montmorillonites before and after $scCO_2$ processing are shown in following figure (Figure 75). Unlike the dispersion seen in SEM images, $scCO_2$ processing did not result in a change of diffraction pattern of Na^+ montmorillonite. The as-received and $scCO_2$ processed Na_+ montmorillonites displayed similar diffraction peaks, a d_{001} diffraction peak at $2\theta =6.8°$ corresponding to an equilibrium platelet spacing of 0.29 nm (basal spacing minus 1 nm for platelet thickness). For Ca^{2+} montmorillonite, a significant diffraction peak shift to lower 2θ was presented. The as-received Ca^{2+} montmorillonite showed a d_{001} diffraction peak at $2\theta =6.4°$ corresponding to an equilibrium platelet spacing of 0.38 nm, after $scCO_2$ processing, the diffraction peak shift to $2\theta =6.1°$ corresponding to an equilibrium platelet spacing of 0.45 nm. We attribute this change of microstructure to the weak inter platelet interactions inside Ca^{2+} montmorillonite tactoids and the result is in agreement with what we observed in SEM images above. Based on SEM and WAXD analysis, the optimized $scCO_2$ processing method is an effective and universal method to pre-disperse both natural and commercial clays. Generally the $scCO_2$

processing result in pre-dispersion of natural clays where micro morphology been changed, however in some cases nano scale structure change may be not achievable.
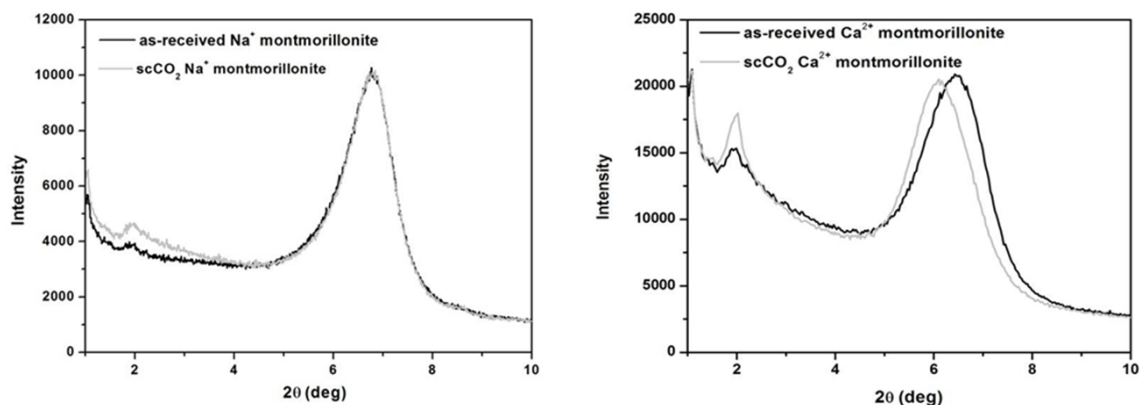
Figure 75 WAXD patterns of as-received and scCO2-processed Na$^+$ and Ca^{2+} montmorillonite

Thermal properties of PET/Na$^+$ nanocomposites were studied as function of scCO2 processing and loadings using DSC. Figure 76 presents the DSC cooling and re-heating cycles for pure PET and PET/Na$^+$ nanocomposites. In comparison with pure PET, incorporation of clay significantly changed the thermal behaviors of matrix. During the rapidly cooling cycle, pure PET displayed a relatively weak crystalline peak around 152.6^{o}C due to its slowly crystallizing rate, whereas all of the nanocomposites exhibited distinct crystalline peaks with shifting to higher temperature. Conversely, for the re-heating cycle, pure PET demonstrated a notable crystalline peak around 139.4^{o}C, however no distinct crystalline peaks were observed for all nanocomposites and their melting peaks slightly shifted to higher temperature than that of pure PET. The significant changes of crystalline behavior were attributed to the heterogeneous nucleating effect of clay particles, which serve as heterogeneous nucleating sites that facilitate crystallization of the matrix due to significantly decrease the activation energy

163

for nucleation. Similar phenomena have been reported by other researches and further study found that the crystallization rates of PET/clay nanocomposites were increased significantly [149].
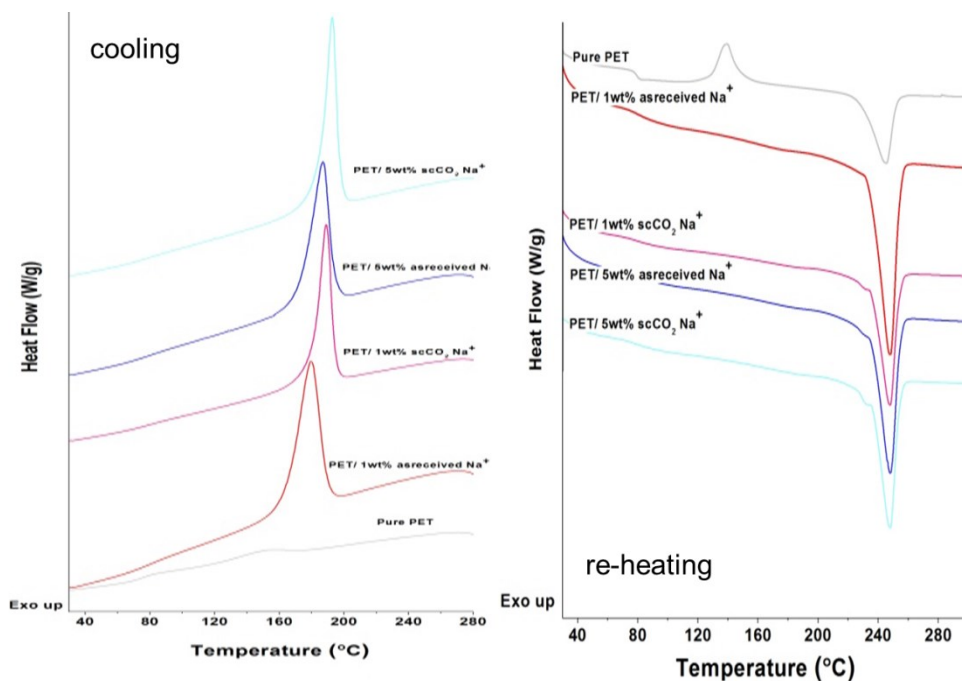
Figure 76 DSC curves of PET/as-received and scCO$_2$-processed Na$^+$ montmorillonite nanocomposites with different clay loading.

Table 11 reports the effects of scCO$_2$ processing and clay fraction on cooling crystallization temperature, T_c, enthalpy of cooling crystallization, ΔH_c, glass transition temperature, T_g, melting temperature, T_m, enthalpy of re-heating crystallization, T_c and enthalpy of melting, ΔH_m of PET. With an increase in clay fraction or improvement of clay dispersion by scCO$_2$ processing, the T_c of nanocomposites significantly shifted to higher value and corresponding enthalpy increased slightly, those phenomena could attribute to the increase of heterogeneous nucleating sites. Comparing nanocomposites with as-received clay, the crystallization peaks of scCO$_2$ processed samples became

narrow and sharp, which might be caused by the improved homogenous dispersion of clay. All of nanocomposites with as-received clay demonstrated slightly increase of T_g as compared with pure PET, whereas, no distinct shifts were observed for $scCO_2$ processed samples. The slightly higher T_g for as-received clay reinforce sample can be attributed to large amount of polymer intercalated between platelets and/or the presence of larger clay particles which could confine and/or block the movement of polymer chains, respectively [50, 151]. This result is in good agreement with previous research that showed increase of T_g in intercalated polymer/clay nanocomposites, whereas, exfoliated clay particles had limited effect on chains movement. In addition, the rest of thermal properties of all nanocomposites failed to reveal any variation as function of clay loading or $scCO_2$ processing, indicating that the increase of heterogeneous nucleating sites and improvement of their uniformly distribution have very little effects on re-crystallization and meting process of PET. On the basis of DSC data, $scCO_2$ had achieved improved dispersion of clay with delaminated structure and uniform distribution, which is highly consistent with what we have seen in previously structural characterizations.

Table 11 T_C, T_g, T_m, ΔH_C and ΔH_m PET/ Na^+ nanocomposites.

Sample	Cooling process			Reheating process		
	T_c (°C)	ΔH_c (J/g)	T_g (°C)	T_c (°C)	T_m (°C)	ΔH_m (J/g)
Pure PET	182.6	NA	79.7	139.4	244.9	34.8
PET/1wt% as-received Na^+	179.2	43.5	80.2	NA	247.6	42.9
PET/1wt% $scCO_2$ Na^+	188.8	54.4	79.2	NA	247.6	44.1
PET/5wt% as-received Na^+	186.6	52.1	83.0	NA	244.9	44.7
PET/5wt% $scCO_2$ Na^+	192.5	58.2	78.5	NA	247.9	44.8

Figure 77 presents the oxygen permeations of pure PET and Na^+ reinforced nanocomposites as functions of $scCO_2$ processing and clay fraction. As what has been

expected, incorporation of impermeable clay particles into PET could both lower the solubility (decreasing organic phase) and effective diffusivity (creating tortuous pathways) of gas molecules. The permeation data reported here displayed good agreement with the theoretical predications. The permeation exhibited continuously decreased with the increase of clay fraction. In particular, with the as-received clay, 1wt% leaded to a 32% of reduction of oxygen permeation and 5wt% resulted in a 40% reduction. In comparison with as-received clay, the incorporation of $scCO_2$ processed clay further decreased the permeation at 5wt%, a maximum reduction (~42%) in oxygen permeation has been achieved by applying 5wt% of $scCO_2$ processed clays. It is worth to mention that we used natural clay here to improved barrier properties and very promising results were shown here. If we take into consideration that the unmodified clay possesses unfavorable thermal dynamic interaction with the PET and the short processing time post high kinetic barrier to form good dispersion, the $scCO_2$ processing actually is a very promising way to disperse natural clay. Moreover the high thermal stability of natural clay offer unique thermal characteristics to PET/clay nanocomposites that can resistant to high temperature and open the window for PET/clay nanocomposites to undergo post processing treatment such as solid state polymerization, which is conducted at elevated temperature and has been reported to effectively improve physical properties of final PET product.
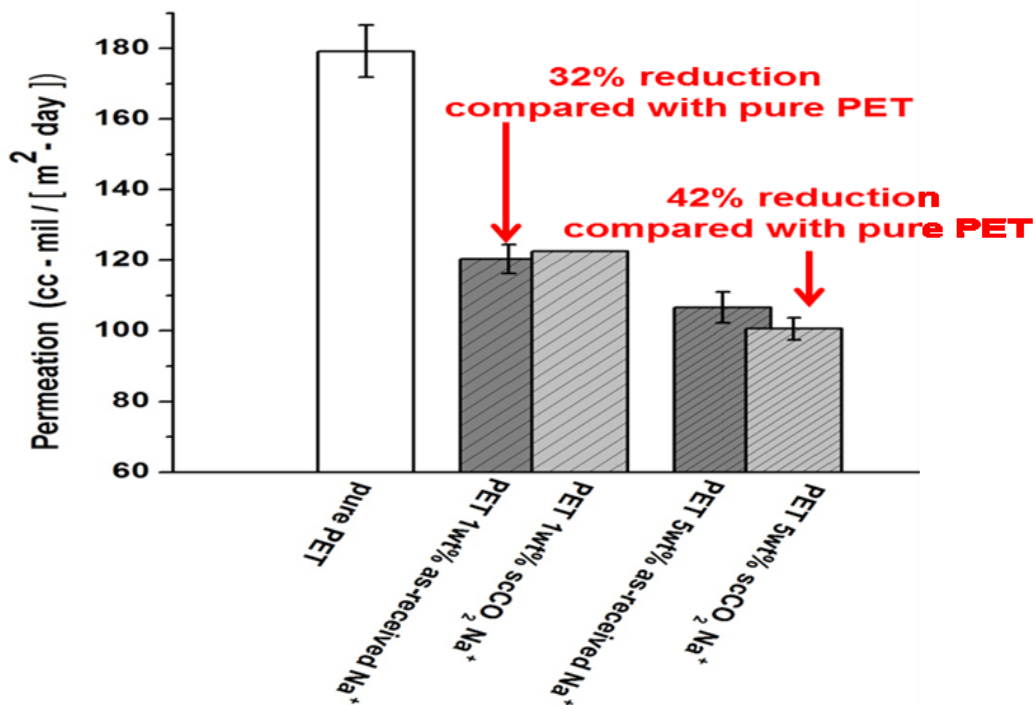
Figure 77 Oxygen permeations of pure PET and PET/Na$^+$ nanocomposites.

6.2 Synthesis of thermal stable and PET compatible modifiers

In order to improve both clay's thermal stability and compatibility to PET, we started synthesizing alkyl imidazolium salt based surfactant which has been reported to hold significantly improved thermal stability. The imidazolium salt also enables us to eventually work with other functional groups to manipulate polymer-modifier interaction and improve polymer-clay compatibility. The chemical structure of dimethyl alkyl imidazolium salt is shown in Figure 78. In order to improve the compatibility of modified clay with PET, the 'R' group should be an alkyl chain with optimum length and interaction with PET matrix.

167
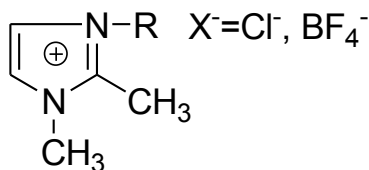
Figure 78 Chemical structure of dimethyl imidazolium salt.

Firstly, we chose 1-octadecene-2,3-dimethyl-imidazolium chloride, whose structure is shown in Figure 79. This modifier was synthesized by using the procedure: 1,2-dimethyl-imidazole (distilled, 0.95 mol) was added to an excess of octadecene chloride (1 mol) in 50 ml acetonitrile in a thick-walled, single-neck 2 l round-bottom flask equipped with a reflux condenser. The solution was degassed several times with dry nitrogen, and gradually heated to 60 $^\circ$C, and allowed to react for 1 day under nitrogen atmosphere. Then the temperature was increased to 90 $^\circ$C and the reaction refluxed for an additional 6 days under nitrogen. After the reaction was complete, a large excess of ethyl acetate was added to precipitate the imidazolium salt. This solid was filtered and washed several times with ethyl acetate to remove all of the unreacted imidazole and alkyl halide. Residual solvent was removed from the resulting 1-octadecene-2,3-dimethyl-imidazolium salt under vacuum, at 80 $^\circ$C, for 12 h. The solid was re-dissolved in a minimum of acetonitrile and precipitated with ethyl acetate. The white solid was filtered and washed with ethyl acetate, and solvent removed under vacuum at 80 $^\circ$C.
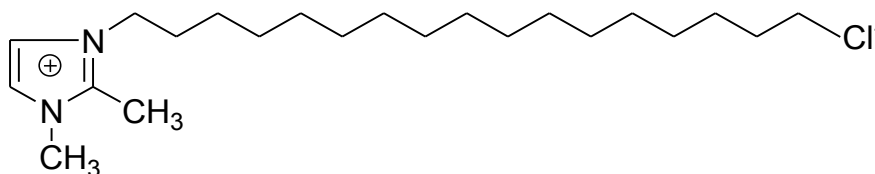
Figure 79 Chemical structure of 1-octadecene-2,3-dimethyl-imidazolium chloride.

The ^{1}H-NMR spectrum of synthesized 1-octadecene-2,3-dimethyl-imidazolium chloride are given in the following figure (Figure 80). From the spectrum we see that the well-defined chemical structure of 1-octadecene-2,3-dimethyl-imidazolium chloride modifier was obtained.
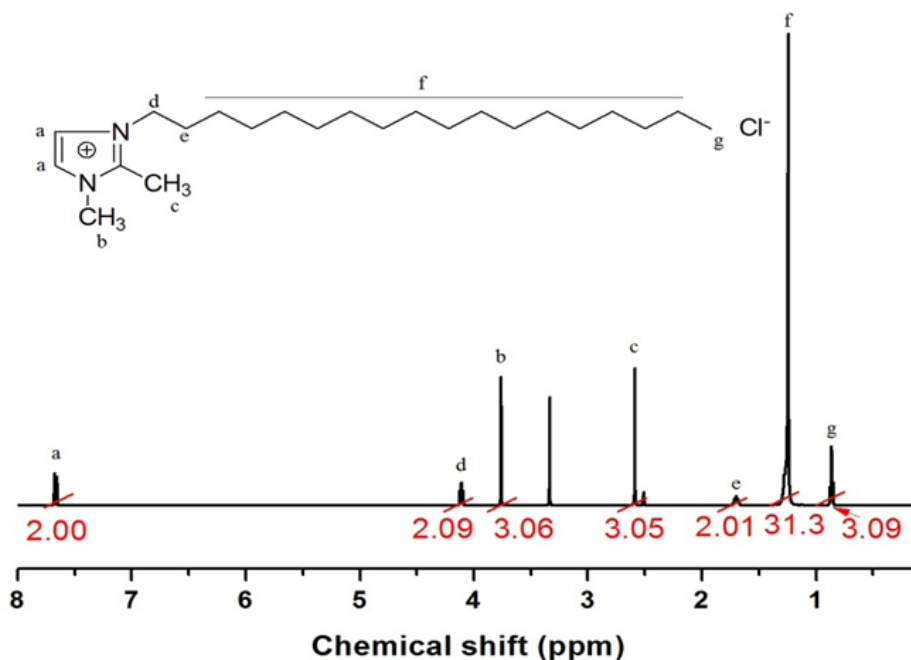
Figure 80 ^{1}H-NMR spectrum of 1-octadecene-2,3-dimethyl-imidazolium chloride.

After obtaining the modifier, the organic silicate hybrids were synthesized by a cation-exchange reaction between the layered silicates and excess alkyl imidazolium salt (twice the exchange capacity of the host). The alkyl chain modified imidazolium salt cation was dissolved in a 50:50 mixture of ethanol and deionized H_2O at 70°C. A 1wt% aqueous suspension of the layered silicate (stirred under 70°C for 24h) was added to the alkyl chain modified imidazolium salt cation solution and the mixture was stirred for 6h at 70°C. The cation-exchanged silicates were collected by filtration and subsequently washed with a mixture of hot ethanol and deionized H_2O several times until all unreacted

alkyl imidazolium salt have been removed. The filter cake was washed by deionized H_2O and dried at room temperature, and re-dissolved in to 40ml deionized H_2O and quickly freezing by liquid nitrogen. Finally, the freezing solid was lyophilized to remove deionized H_2O, and then the obtained fine powder was dry under vacuum oven at 80 ^oC and the final product was kept in desiccant. The cation-exchange capacity for sodium balanced montmorillonite clay is 96 milliequivalents/100g. So, for 8 grams of clay, we calculated with the following procedure.

$$Amount \quad of \quad Modifier = 16 \times 96 \div 100 \times 10^{-3} = 0.01536 mol$$

Because for the cations exchanging reaction happens between modifier and clay, we always double the molar equivalent of modifier to ensure the maximum ion exchange. For every modifier we need:

$$Amount \quad of \quad Modifier = 2 \times 16 \times 96 \div 100 \times 10^{-3} = 0.03072 \approx 0.04 mol$$

Example: We need 15.4g of the modifier 1-Octadecene-2,3-dimethyl-imidazolium chloride (molecular weight=385.07g/mol), to accomplish modification of both as-received clay and scCO$_2$ processed clay.

The organic modification process was assessed by solubility studies. Figure 81 showed the optical images of all solubility tests. When using DI water as the solvent, natural clay (A) showed good solubility in water because of the intrinsic hydrophilic property, while after modification, the organic modified clay (B) showed hydrophobic behavior (Top left). In order to validate modification reaction, the modifier (40 wt%) and natural clay (B) were mechanically mixed and put in to DMF. Images (top right) showed that modification reaction (C&D) made the organic clay solvable in DMF while mechanical mixing (B) cannot. The solutions of organic clay in DMF were kept for 1

week; we found that scCO$_2$ processed clay showed better modification than as-received clay (bottom right). Moreover, an as-received commercialized 20A sample was dissolved into DMF as a control; we found that the modified clays are better dispersed, because their solubilities in DMF are higher than that of commercialized 20A (bottom left).
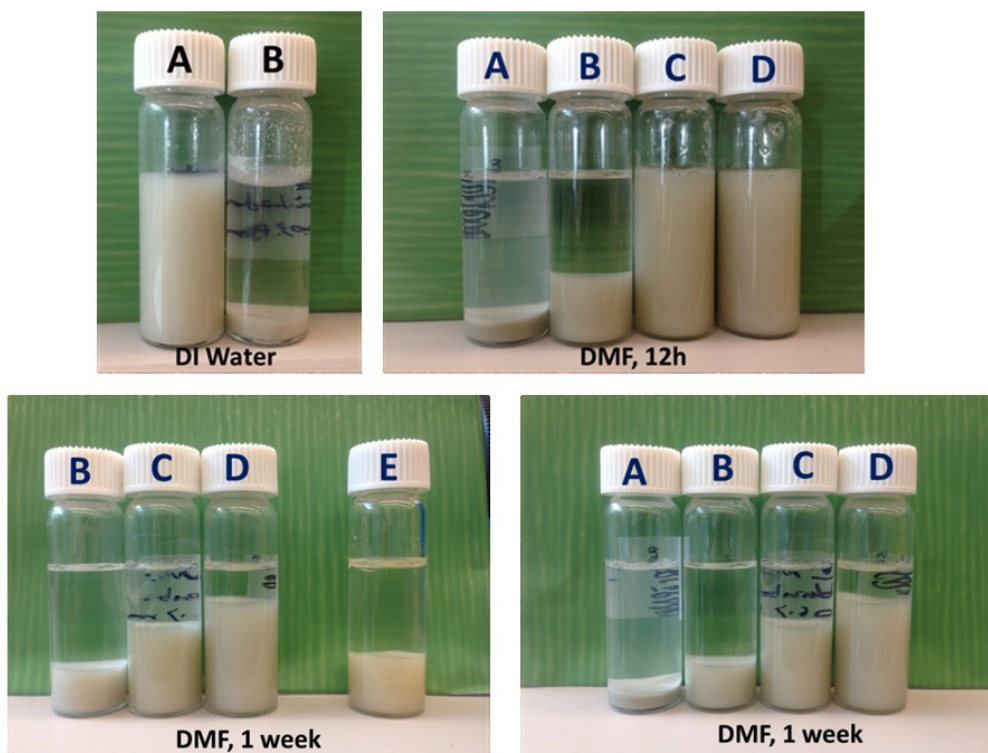
Figure 81 Optical images of natural Na$^+$ and modified clays in DI water and DMF

TGA (Figure 82) was used to confirm the improved thermal stability. Since the chemical structure of 1-octadecene-2,3-dimethyl-imidazolium modified clay is similar to that of 20A, so we compared 1-octadecene-2,3-dimethyl-imidazolium modified clay with 20A. Both 20A and imidazolium salt modified clay showed a three stages weight loss curve in temperature range from 20 to 700°C [74], indicating both of their modifiers have similar chemical structures and following same degradation evolution. The first stage was below 100°C, which was related with the release of free water on clay surface or inter

171

gallery space. Two separated stages were observed around 310 and 600°C were observed for 20A, which were attributed to the decomposition of organic modifiers and decomposition of structural water. In comparison, imidazolium salt modified clay exhibited similar weight lose peaks as 20A in this range, whereas the peaks positions were shifted to higher temperature of 345 and >700°C, which were attributed to the decomposition of organic modifiers and decomposition of structural water. We confirmed that imidazolium salt modified clay significantly improved the thermal stability. Additionally, the weight loss at 700°C for imidazolium salt modified clay is 30%, indicating 30wt% modifiers were attached on the clay surface through the cations exchanging reaction. The imidazolium salt modified clay was supposed to enable significantly improving physical properties of PET/clay nanocomposites, because the improved thermal stability could improve the polymer-clay interface due to avoid the severe thermally degradation of modifiers. However, our preliminary oxygen permeation test confirmed that although imidazolium salt modified clay significantly improved the thermal stability, it resulted in the similar effect on permeation test as 20A did; no prominent improvement in permeation was achieved. We speculate that for the imidazolium salt modified clay, the similar chemical structure of the modifier as 20A result in the PET-clay interaction, which form a relatively ineffective interface that cannot lead to a significant improvement in oxygen permeation. In order to improve PET's barrier properties, the compatibility between PET and clay should be taken into consideration as improving the thermal stability. Since 30B was proved to be a good candidate for PET, so we try to mimic 30B's chemical structure and improve its thermal stability simultaneously.
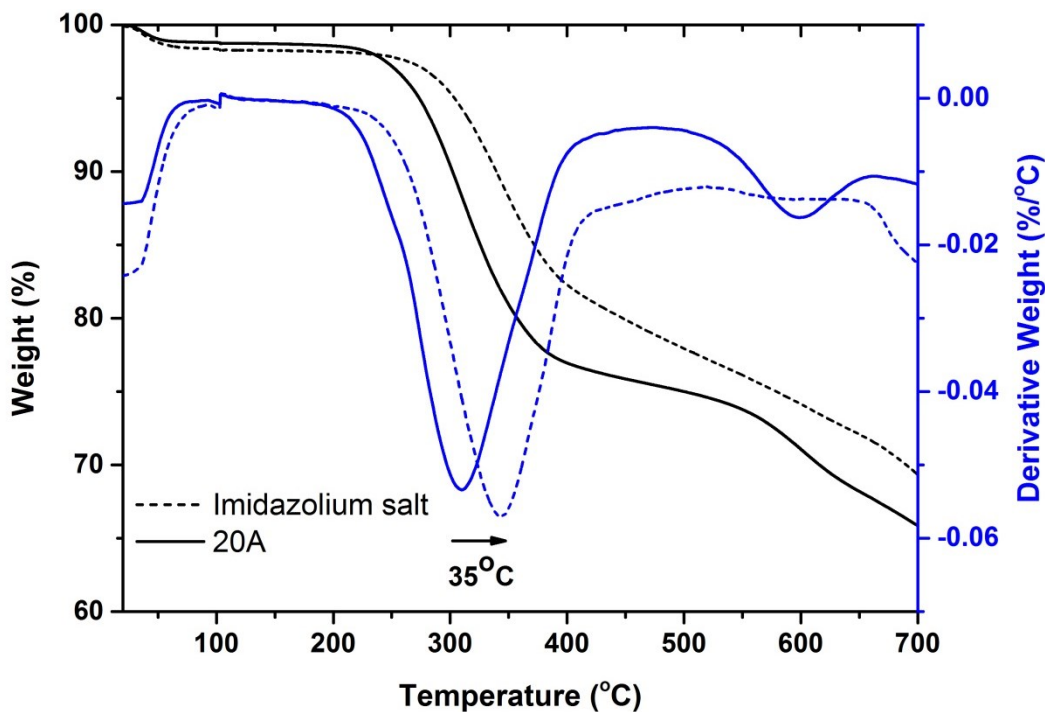
Figure 82 TGA curves of 20A and imidazolium salt modified clay.

In order to mimic 30B, we synthesized 1-octanol-2,3 dimethyl-imidazolium chloride which has a hydroxyl group, whose structure is shown in Figure 83. This modifier was synthesized by using the procedure: 1,2-dimethyl-imidazole (distilled, 0.95 mol) was added to an excess of 1-octanol chloride (1 mol) in 50 ml acetonitrile in a thick-walled, single-neck 2 l round-bottom flask equipped with a reflux condenser. The solution was degassed several times with dry nitrogen, and gradually heated to 60 °C, and allowed to react for 1 day under nitrogen atmosphere. Then the temperature was increased to 90 °C and the reaction refluxed for an additional 6 days under nitrogen. After the reaction was complete, a large excess of ethyl acetate was added to precipitate the imidazolium salt. This solid was filtered and washed several times with ethyl acetate to remove all of the unreacted imidazole and alkyl halide. Residual solvent was removed

173

from the resulting 1-octanol-2,3 dimethyl-imidazolium salt under vacuum, at 80 °C, for 12 h. The solid was re-dissolved in a minimum of acetonitrile and precipitated with ethyl acetate. The white solid was filtered and washed with ethyl acetate, and solvent removed under vacuum at 80 °C.

Figure 83 Chemical structure of 1-octanol-2,3 dimethyl-imidazolium chloride.

The ^{1}H-NMR spectrum of synthesized 1-octanol-2,3 dimethyl-imidazolium chloride are given in the following figure (Figure 84.). From the spectrum we see that the well-defined chemical structure of 1-octanol-2,3 dimethyl-imidazolium chloride modifier was obtained.
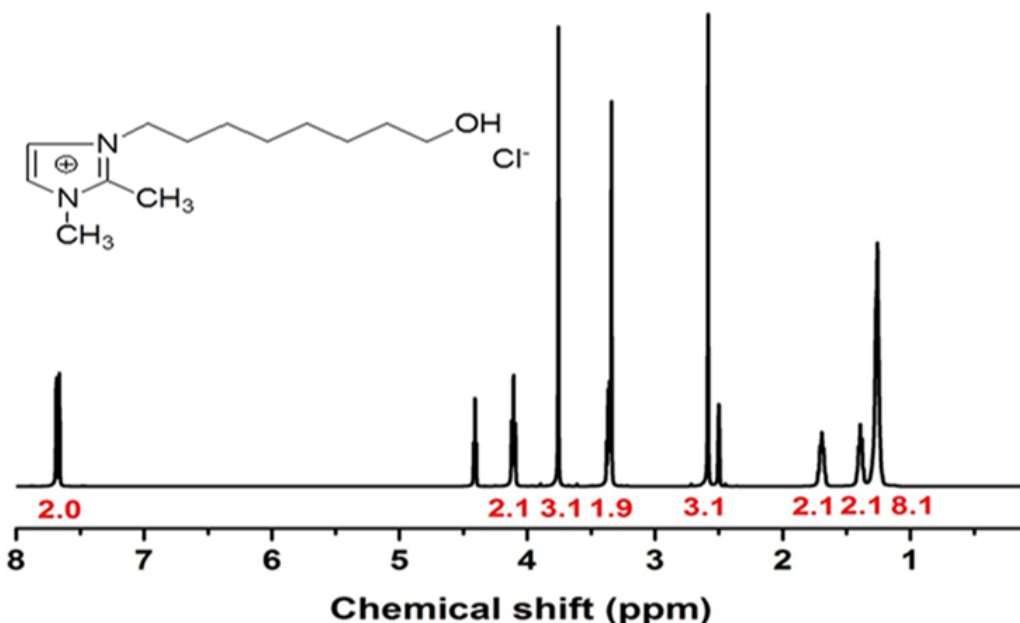
Figure 84 ^{1}H-NMR spectrum of 1-octanol-2,3 dimethyl-imidazolium chloride.

After obtaining the modifiers, the organic silicate hybrids were synthesized by a cation-exchange reaction between the layered silicates and excess 1-octanol-2,3 dimethyl-imidazolium salt (twice the exchange capacity of the host). The modified imidazolium salt cation was dissolved in a 50:50 mixture of ethanol and deionized H_2O at 70°C. A 1wt% aqueous suspension of the layered silicate (stirred under 70°C for 24h) was added to the modified imidazolium salt cation solution and the mixture was stirred for 6h at 70°C. The cation-exchanged silicates were collected by filtration and subsequently washed with a mixture of hot ethanol and deionized H_2O several times until all unreacted imidazolium salt have been removed. The filter cake was washed by deionized H_2O and dried at room temperature, and re-dissolved in to 40ml deionized H_2O and quickly freezing by liquid nitrogen. Finally, the freezing solid was lyophilized to remove deionized H_2O, and then the obtained fine powder was dry under vacuum oven at 80 ^{o}C and the final product was kept in desiccant. The cation-exchange capacity for sodium balanced montmorillonite clay is 96 milliequivalents/100g.

In order to confirm that we successfully attached 1-octanol-2,3 dimethyl-imidazolium chloride on to the clay surface and introduced a hydroxyl group, the FTIR spectrum of 1-octanol-2,3 dimethyl-imidazolium salt modified clay is shown in Figure 85. As shown in the figure, a sharp O-H stretching band was observed around 3300cm^{-1} due to the present of free hydroxyl group in 1-octanol-2,3 dimethyl-imidazolium chloride, in addition, two other characteristic peaks from imidazole ring were also observed, the stretching band of C=N exhibited a peak around 2350cm^{-1} and multiple peaks around 1500cm^{-1} were attributed to the imidazole ring, indicating that 1-octanol-2,3 dimethyl-imidazolium chloride was attached on clay surface and the hydroxyl was introduced.

We speculated that due to the potential of forming hydrogen bonding between PET and the hydroxyl group in 1-octanol-2,3 dimethyl-imidazolium chloride, the strong PET-clay interaction will result in effective interface and improving the barrier properties. In addition, the imidazolium salt base also improves the thermal stability of the modifier, which will avoid thermal degradation in melting extrusion and discolor of the samples.
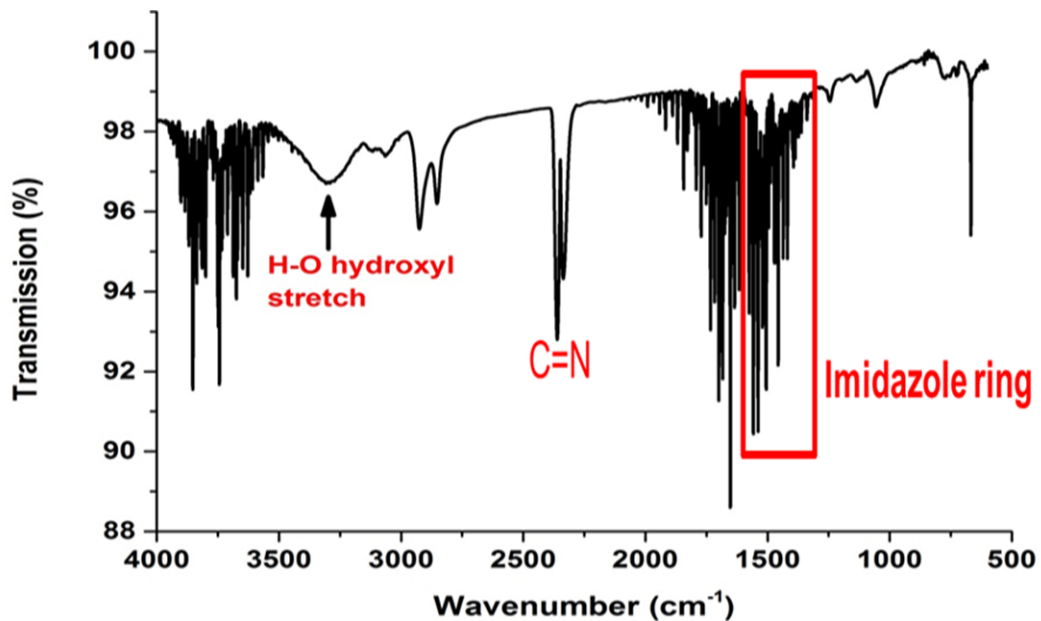
Figure 85 FTIR spectrum of 1-octanol-2,3 dimethyl-imidazolium salt modified montmorillonite clay.

REFERENCES

[1] http://www.wfp.org/hunger/stats.

[2] http://www.who.int/en/.

[3] http://www.huffingtonpost.com/eric-holt-gimenez/world-hunger_b_1463429.html.

[4] http://www.globalissues.org/issue/6/world-hunger-and-poverty.

[5] http://www.fao.org/docrep/014/mb060e/mb060e00.htm.

[6] http://www.worldfoodscience.org/cms/?pid=1006206&printable=1.

[7]http://www.ift.org/Knowledge-Center/Read-IFT-Publications/Science-Reports/Scientific-Status-Summaries/Editorial/Food-Packaging-and-Its-Environmental-Impact.aspx.

[8] http://www.kshs.org/p/kansas-archeology-basics/14588.

[9] http://www.wiley.com/WileyCDA/WileyTitle/productCd-EHEP000300.html.

[10]http://firatozel.files.wordpress.com/2011/09/chemical_migration_and_food_contact_materials.pdf.

[11]http://www.ldrt.gov.za/application/freight_transport_databank/lim/industries/shoes_textiles_clothing/index.html.

[12]https://www.smitherspira.com/global-packaging-industry-expected-to-reach-820-billion-by-2016.aspx.

[13] D. Feldman, Polymer Barrier Films, Journal of Polymers and the Environment, 9 (2001) 49-55.

[14] Y. Leterrier, Durability of nanosized oxygen-barrier coatings on polymers, Progress in Materials Science, 48 (2003) 1-55.

[15] N. Boutroy, Y. Pernel, J.M. Rius, F. Auger, H.J.v. Bardeleben, J.L. Cantin, F. Abel, A. Zeinert, C. Casiraghi, A.C. Ferrari, J. Robertson, Hydrogenated amorphous carbon film coating of PET bottles for gas diffusion barriers, Diamond and Related Materials, 15 (2006) 921-927.

[16] http://www.ptonline.com/articles/barrier-pet-bottles.

[17] G. Choudalakis, A.D. Gotsis, Permeability of polymer/clay nanocomposites: A review, European Polymer Journal, 45 (2009) 967-984.

[18] E. Manias, A. Touny, L. Wu, K. Strawhecker, B. Lu, T.C. Chung, Polypropylene/Montmorillonite Nanocomposites. Review of the Synthetic Routes and Materials Properties, Chemistry of Materials, 13 (2001) 3516-3523.

[19] E.P. Giannelis, Polymer-layered silicate nanocomposites: Synthesis, properties and applications, Applied Organometallic Chemistry, 12 (1998) 675-680.

[20] P.S. Thomas, P.A. Sreekumar, A.S. Aprem, S. Thomas, Poly(ethylene-co-vinyl acetate)/calcium phosphate nanocomposites: Mechanical, gas permeability, and molecular transport properties, Journal of Applied Polymer Science, 120 (2011) 1974-1983.

[21] B. Xu, Q. Zheng, Y. Song, Y. Shangguan, Calculating barrier properties of polymer/clay nanocomposites: Effects of clay layers, Polymer, 47 (2006) 2904-2910.

[22] J.M. Herrera-Alonso, E. Marand, J. Little, S.S. Cox, Polymer/clay nanocomposites as VOC barrier materials and coatings, Polymer, 50 (2009) 5744-5748.

[23] J.M. Herrera-Alonso, Z. Sedláková, E. Marand, Gas transport properties of polyacrylate/clay nanocomposites prepared via emulsion polymerization, Journal of Membrane Science, 363 (2010) 48-56.

[24] E. Dunkerley, D. Schmidt, Effects of Composition, Orientation and Temperature on the O2 Permeability of Model Polymer/Clay Nanocomposites, Macromolecules, 43 (2010) 10536-10544.

[25] B. Alexandre, D. Langevin, P. Médéric, T. Aubry, H. Couderc, Q.T. Nguyen, A. Saiter, S. Marais, Water barrier properties of polyamide 12/montmorillonite nanocomposite membranes: Structure and volume fraction effects, Journal of Membrane Science, 328 (2009) 186-204.

[26] N. Bitinis, R. Verdejo, E.M. Maya, E. Espuche, P. Cassagnau, M.A. Lopez-Manchado, Physicochemical properties of organoclay filled polylactic acid/natural rubber blend bionanocomposites, Composites Science and Technology, 72 (2012) 305-313.

[27] Y.S. Hu, D.A. Schiraldi, A. Hiltner, E. Baer, Structural Model for Oxygen Permeability of a Liquid Crystalline Polymer, Macromolecules, 36 (2003) 3606-3615.

[28] R. Ash, R.M. Barrer, J.H. Petropoulos, Diffusion in heterogeneous media: properties of a laminated slab, British Journal of Applied Physics, 14 (1963) 854.

[29] R.K. Bharadwaj, Modeling the barrier properties of polymer-layered silicate nanocomposites, Macromolecules, 34 (2001) 9189-9192.

[30] L. Sun, W.J. Boo, A. Clearfield, H.J. Sue, H.Q. Pham, Barrier properties of model epoxy nanocomposites, Journal of Membrane Science, 318 (2008) 129-136.

[31] L.E. Nielsen, Models for the Permeability of Filled Polymer Systems, Journal of Macromolecular Science: Part A - Chemistry, 1 (1967) 929-942.

[32] E.L. Cussler, S.E. Hughes, W.J. Ward Iii, R. Aris, Barrier membranes, Journal of Membrane Science, 38 (1988) 161-174.

[33] G.H. Fredrickson, J. Bicerano, Barrier properties of oriented disk composites, The Journal of Chemical Physics, 110 (1999) 2181-2188.

[34] A.A. Gusev, H.R. Lusti, Rational Design of Nanocomposites for Barrier Applications, Advanced Materials, 13 (2001) 1641-1643.

[35] http://en.wikipedia.org/wiki/Montmorillonite.

[36] S. Sinha Ray, M. Okamoto, Polymer/layered silicate nanocomposites: a review from preparation to processing, Progress in Polymer Science, 28 (2003) 1539-1641.

[37] S. Sinha Ray, Clay-Containing Polymer Nanocomposites From Fundamentals to Real Applications, in, Elsevier Science, Oxford :, 2013.

[38] E.P. Giannelis, Polymer Layered Silicate Nanocomposites, Advanced Materials, 8 (1996) 29-35.

[39] S. Lee, K.H. Henthorn, Particle Technology and Applications, CRC Press March 26, 2012

[40] T. Kurose, V.E. Yudin, J.U. Otaigbe, V.M. Svetlichnyi, Compatibilized polyimide (R-BAPS)/BAPS-modified clay nanocomposites with improved dispersion and properties, Polymer, 48 (2007) 7130-7138.

[41] H. Heinz, R.A. Vaia, R. Krishnamoorti, B.L. Farmer, Self-Assembly of Alkylammonium Chains on Montmorillonite: Effect of Chain Length, Head Group Structure, and Cation Exchange Capacity, Chemistry of Materials, 19 (2006) 59-68.

[42] Y. Xi, R.L. Frost, H. He, Modification of the surfaces of Wyoming montmorillonite by the cationic surfactants alkyl trimethyl, dialkyl dimethyl, and trialkyl methyl ammonium bromides, Journal of Colloid and Interface Science, 305 (2007) 150-158.

[43] S.K. Kumar, N. Jouault, B. Benicewicz, T. Neely, Nanocomposites with Polymer Grafted Nanoparticles, Macromolecules, 46 (2013) 3199-3214.

[44] M. Kráčalík, M. Studenovský, J. Mikešová, A. Sikora, R. Thomann, C. Friedrich, I. Fortelný, J. Šimoník, Recycled PET nanocomposites improved by silanization of organoclays, Journal of Applied Polymer Science, 106 (2007) 926-937.

[45] A.B. Morgan, J.W. Gilman, Characterization of polymer-layered silicate (clay) nanocomposites by transmission electron microscopy and X-ray diffraction: A comparative study, Journal of Applied Polymer Science, 87 (2003) 1329-1338.

[46] Y. Lyatskaya, A.C. Balazs, Modeling the Phase Behavior of Polymer−Clay Composites, Macromolecules, 31 (1998) 6676-6680.

[47] V.V. Ginzburg, C. Singh, A.C. Balazs, Theoretical Phase Diagrams of Polymer/Clay Composites: The Role of Grafted Organic Modifiers, Macromolecules, 33 (2000) 1089-1099.

[48] A.S. Zerda, A.J. Lesser, Intercalated clay nanocomposites: Morphology, mechanics, and fracture behavior, Journal of Polymer Science Part B: Polymer Physics, 39 (2001) 1137-1146.

[49] Y. Hu, L. Song, J. Xu, L. Yang, Z. Chen, W. Fan, Synthesis of polyurethane/clay intercalated nanocomposites, Colloid Polym Sci, 279 (2001) 819-822.

[50] X. Fu, S. Qutubuddin, Polymer–clay nanocomposites: exfoliation of organophilic montmorillonite nanolayers in polystyrene, Polymer, 42 (2001) 807-813.

[51] T. Lan, P.D. Kaviratna, T.J. Pinnavaia, Mechanism of Clay Tactoid Exfoliation in Epoxy-Clay Nanocomposites, Chemistry of Materials, 7 (1995) 2144-2150.

[52] P.C. LeBaron, Z. Wang, T.J. Pinnavaia, Polymer-layered silicate nanocomposites: an overview, Applied Clay Science, 15 (1999) 11-29.

[53] S. Sinha Ray, P. Maiti, M. Okamoto, K. Yamada, K. Ueda, New Polylactide/Layered Silicate Nanocomposites. 1. Preparation, Characterization, and Properties, Macromolecules, 35 (2002) 3104-3110.

[54] H. Shi, T. Lan, T.J. Pinnavaia, Interfacial Effects on the Reinforcement Properties of Polymer−Organoclay Nanocomposites, Chemistry of Materials, 8 (1996) 1584-1587.

[55] RamanathanT, A.A. Abdala, StankovichS, D.A. Dikin, M. Herrera Alonso, R.D. Piner, D.H. Adamson, H.C. Schniepp, ChenX, R.S. Ruoff, S.T. Nguyen, I.A. Aksay, R.K. Prud'Homme, L.C. Brinson, Functionalized graphene sheets for polymer nanocomposites, Nat Nano, 3 (2008) 327-331.

[56] Q.-X. Jia, Y.-P. Wu, Y.-Q. Wang, M. Lu, L.-Q. Zhang, Enhanced interfacial interaction of rubber/clay nanocomposites by a novel two-step method, Composites Science and Technology, 68 (2008) 1050-1056.

[57] K. Tamura, S. Yokoyama, C.S. Pascua, H. Yamada, New Age of Polymer Nanocomposites Containing Dispersed High-Aspect-Ratio Silicate Nanolayers, Chemistry of Materials, 20 (2008) 2242-2246.

[58] S. Takahashi, D.R. Paul, Gas permeation in poly(ether imide) nanocomposite membranes based on surface-treated silica. Part 1: Without chemical coupling to matrix, Polymer, 47 (2006) 7519-7534.

[59] J.B. Hooper, K.S. Schweizer, Theory of Phase Separation in Polymer Nanocomposites, Macromolecules, 39 (2006) 5133-5142.

[60] M. Manitiu, R.J. Bellair, S. Horsch, E. Gulari, R.M. Kannan, Supercritical Carbon Dioxide-Processed Dispersed Polystyrene−Clay Nanocomposites, Macromolecules, 41 (2008) 8038-8046.

[61] A. Usuki, M. Kawasumi, Y. Kojima, A. Okada, T. Kurauchi, O. Kamigaito, Synthesis and structure of smectic clay/poly (methylmethacrylate) and clay/polystyrene nanocomposite via in situ intercalative polymerisation, Mater. Res, 8 (1993) 1174-1178.

[62] Y. Zhong, Z. Zhu, S.-Q. Wang, Synthesis and rheological properties of polystyrene/layered silicate nanocomposite, Polymer, 46 (2005) 3006-3013.

[63] M. Okamoto, S. Morita, H. Taguchi, Y.H. Kim, T. Kotaka, H. Tateyama, Synthesis and structure of smectic clay/poly(methyl methacrylate) and clay/polystyrene nanocomposites via in situ intercalative polymerization, Polymer, 41 (2000) 3887-3890.

[64] P. Meneghetti, S. Qutubuddin, Synthesis of Poly(methyl methacrylate) Nanocomposites via Emulsion Polymerization Using a Zwitterionic Surfactant, Langmuir, 20 (2004) 3424-3430.

[65] B. Lepoittevin, N. Pantoustier, M. Devalckenaere, M. Alexandre, D. Kubies, C. Calberg, R. Jérôme, P. Dubois, Poly(ε-caprolactone)/Clay Nanocomposites by in-Situ Intercalative Polymerization Catalyzed by Dibutyltin Dimethoxide, Macromolecules, 35 (2002) 8385-8390.

[66] R.A. Vaia, E.P. Giannelis, Lattice Model of Polymer Melt Intercalation in Organically-Modified Layered Silicates, Macromolecules, 30 (1997) 7990-7999.

[67] J.I. Sohn, C.H. Lee, S.T. Lim, T.H. Kim, H.J. Choi, M.S. Jhon, Viscoelasticity and relaxation characteristics of polystyrene/clay nanocomposite, Journal of Materials Science, 38 (2003) 1849-1852.

[68] A.B. Morgan, J.D. Harris, Exfoliated polystyrene-clay nanocomposites synthesized by solvent blending with sonication, Polymer, 45 (2004) 8695-8703.

[69] R.A. Vaia, H. Ishii, E.P. Giannelis, Synthesis and properties of two-dimensional nanostructures by direct intercalation of polymer melts in layered silicates, Chemistry of Materials, 5 (1993) 1694-1696.

[70] R.A. Vaia, K.D. Jandt, E.J. Kramer, E.P. Giannelis, Microstructural Evolution of Melt Intercalated Polymer−Organically Modified Layered Silicates Nanocomposites, Chemistry of Materials, 8 (1996) 2628-2635.

[71] R.A. Vaia, E.P. Giannelis, Polymer Melt Intercalation in Organically-Modified Layered Silicates: Model Predictions and Experiment, Macromolecules, 30 (1997) 8000-8009.

[72] O. Meincke, B. Hoffmann, C. Dietrich, C. Friedrich, Viscoelastic Properties of Polystyrene Nanocomposites Based on Layered Silicates, Macromolecular Chemistry and Physics, 204 (2003) 823-830.

[73] S. Tanoue, L.A. Utracki, A. Garcia-Rejon, P. Sammut, M.-T. Ton-That, I. Pesneau, M.R. Kamal, J. Lyngaae-Jørgensen, Melt compounding of different grades of polystyrene with organoclay. Part 2: Rheological properties, Polymer Engineering & Science, 44 (2004) 1061-1076.

[74] J.M. Cervantes-Uc, J.V. Cauich-Rodríguez, H. Vázquez-Torres, L.F. Garfias-Mesías, D.R. Paul, Thermal degradation of commercially available organoclays studied by TGA–FTIR, Thermochimica Acta, 457 (2007) 92-102.

[75] S. Tanoue, L.A. Utracki, A. Garcia-Rejon, J. Tatibouët, K.C. Cole, M.R. Kamal, Melt compounding of different grades of polystyrene with organoclay. Part 1: Compounding and characterization, Polymer Engineering & Science, 44 (2004) 1046-1060.

[76] M. Kawasumi, N. Hasegawa, M. Kato, A. Usuki, A. Okada, Preparation and Mechanical Properties of Polypropylene−Clay Hybrids, Macromolecules, 30 (1997) 6333-6338.

[77] K.C. Baker, M. Manitiu, R. Bellair, C.A. Gratopp, H.N. Herkowitz, R.M. Kannan, Supercritical carbon dioxide processed resorbable polymer nanocomposite bone graft substitutes, Acta Biomaterialia, 7 (2011) 3382-3389.

[78] R.J. Bellair, M. Manitiu, E. Gulari, R.M. Kannan, Investigation of clay modifier effects on the structure and rheology of supercritical carbon dioxide-processed polymer nanocomposites, Journal of Polymer Science Part B: Polymer Physics, 48 (2010) 823-831.

[79] http://books.google.com/books?hl=en&lr=&id=nOZr7u6102sC&oi=fnd&pg=PR5&dq=S upercritical+carbon+dioxide+&ots=Es17rK1mEs&sig=qLU6SrpTvcF3oyGm2F9YgjiqW Vc#v=onepage&q=Supercritical%20carbon%20dioxide&f=false.

[80] J.M. DeSimone, Z. Guan, C.S. Elsbernd, Synthesis of Fluoropolymers in Supercritical Carbon Dioxide, Science, 257 (1992) 945-947.

[81] J.M. DeSimone, E.E. Maury, Y.Z. Menceloglu, J.B. McClain, T.J. Romack, J.R. Combes, Dispersion Polymerizations in Supercritical Carbon Dioxide, Science, 265 (1994) 356-359.

[82] S.P. Nalawade, F. Picchioni, L.P.B.M. Janssen, Supercritical carbon dioxide as a green solvent for processing polymer melts: Processing aspects and applications, Progress in Polymer Science, 31 (2006) 19-43.

[83] M.P. Scott, C.S. Brazel, M.G. Benton, J.W. Mays, J.D. Holbrey, R.D. Rogers, Application of ionic liquids as plasticizers for poly(methyl methacrylate), Chemical Communications, (2002) 1370-1371.

[84] E. Gulari, G.K. Serhatkulu, Method of delaminating a graphite structure with a coating agent in a supercritical fluid, in, U.S. Patent 7,157,517, Jan 2, 2007.

[85] S. Horsch, G. Serhatkulu, E. Gulari, R.M. Kannan, Supercritical CO2 dispersion of nano-clays and clay/polymer nanocomposites, Polymer, 47 (2006) 7485-7496.

[86] E. Gulari, G.K. Serhatkulu, R.K. Kannan, Method of delaminating aggregated particles with a coating agent in a substantially supercritical fluid, in, U.S. Patent 7,387,749, Jun 17, 2008.

[87] C.W. Manke, E. Gulari, D.F. Mielewski, E.C.-C. Lee, System and method of delaminating a layered silicate material by supercritical fluid treatment, in, U.S. Patent 6,469,073, Oct 22, 2002.

[88] D.F. Mielewski, E.C.-C. Lee, C.W. Manke, E. Gulari, System and method of preparing a reinforced polymer by supercritical fluid treatment, in, U.S. Patent 6,753,360, Jun 22, 2004.

[89] M. Manitiu, S. Horsch, E. Gulari, R.M. Kannan, Role of polymer–clay interactions and nano-clay dispersion on the viscoelastic response of supercritical CO2 dispersed polyvinylmethylether (PVME)–Clay nanocomposites, Polymer, 50 (2009) 3786-3796.

[90] Q.T. Nguyen, D.G. Baird, An improved technique for exfoliating and dispersing nanoclay particles into polymer matrices using supercritical carbon dioxide, Polymer, 48 (2007) 6923-6933.

[91] A.S. Zerda, T.C. Caskey, A.J. Lesser, Highly Concentrated, Intercalated Silicate Nanocomposites: Synthesis and Characterization, Macromolecules, 36 (2003) 1603-1608.

[92] Q. Zhao, E.T. Samulski, A comparative study of poly(methyl methacrylate) and polystyrene/clay nanocomposites prepared in supercritical carbon dioxide, Polymer, 47 (2006) 663-671.

[93] C. Chen, D.G. Baird, Dispersion of nano-clay at higher levels into polypropylene with carbon dioxide in the presence of maleated polypropylene, Polymer, 53 (2012) 4178-4186.

[94] C. Chen, J. Samaniuk, D.G. Baird, G. Devoux, M. Zhang, R.B. Moore, J.P. Quigley, The preparation of nano-clay/polypropylene composite materials with improved properties using supercritical carbon dioxide and a sequential mixing technique, Polymer, 53 (2012) 1373-1382.

[95] A. Ghanbari, M.C. Heuzey, P.J. Carreau, M.T. Ton-That, A novel approach to control thermal degradation of PET/organoclay nanocomposites and improve clay exfoliation, Polymer, 54 (2013) 1361-1369.

[96] M. Ozawa, M. Kimura, A. Isogai, The application of Ce   Zr oxide solid solution to oxygen storage promoters in automotive catalysts, Journal of Alloys and Compounds, 193 (1993) 73-75.

[97] O. Tabata, K. Kawahata, S. Sugiyama, I. Igarashi, Mechanical property measurements of thin films using load-deflection of composite rectangular membranes, Sensors and Actuators, 20 (1989) 135-141.

[98] Y. Fukushima, A. Okada, M. Kawasumi, T. Kurauchi, O. Kamigaito, Swelling behavior of montmorillonite by poly-6-amide, Clay Minerals, 23 (1988) 27-34.

[99] A. Blumstein, Polymerization of adsorbed monolayers. II. Thermal degradation of the inserted polymer, Journal of Polymer Science Part A: General Papers, 3 (1965) 2665-2672.

[100] P. Meneghetti, S. Qutubuddin, Synthesis, thermal properties and applications of polymer-clay nanocomposites, Thermochimica Acta, 442 (2006) 74-77.

[101] J.W. Gilman, Flammability and thermal stability studies of polymer layered-silicate (clay) nanocomposites, Applied Clay Science, 15 (1999) 31-49.

[102] J. Zhu, P. Start, K.A. Mauritz, C.A. Wilkie, Thermal stability and flame retardancy of poly(methyl methacrylate)-clay nanocomposites, Polymer Degradation and Stability, 77 (2002) 253-258.

[103] P. Kiliaris, C.D. Papaspyrides, Polymer/layered silicate (clay) nanocomposites: An overview of flame retardancy, Progress in Polymer Science, 35 (2010) 902-958.

[104] T. Kashiwagi, R.H. Harris Jr, X. Zhang, R.M. Briber, B.H. Cipriano, S.R. Raghavan, W.H. Awad, J.R. Shields, Flame retardant mechanism of polyamide 6–clay nanocomposites, Polymer, 45 (2004) 881-891.

[105] http://www.nanoclay.com/benefits2.asp.

[106] N. Sheng, M.C. Boyce, D.M. Parks, G.C. Rutledge, J.I. Abes, R.E. Cohen, Multiscale micromechanical modeling of polymer/clay nanocomposites and the effective clay particle, Polymer, 45 (2004) 487-506.

[107] J.-J. Luo, I.M. Daniel, Characterization and modeling of mechanical behavior of polymer/clay nanocomposites, Composites Science and Technology, 63 (2003) 1607-1616.

[108] C. Lu, Y.-W. Mai, Influence of Aspect Ratio on Barrier Properties of Polymer-Clay Nanocomposites, Physical Review Letters, 95 (2005) 088303.

[109] Z. Wang, H. Nakajima, E. Manias, T. Chung, Exfoliated PP/clay nanocomposites using ammonium-terminated PP as the organic modification for montmorillonite, Macromolecules, 36 (2003) 8919-8922.

[110] Garcı, amp, x, D. a-López, O. Picazo, J.C. Merino, J.M. Pastor, Polypropylene–clay nanocomposites: effect of compatibilizing agents on clay dispersion, European Polymer Journal, 39 (2003) 945-950.

[111] J. Liu, Y. Gao, D. Cao, L. Zhang, Z. Guo, Nanoparticle Dispersion and Aggregation in Polymer Nanocomposites: Insights from Molecular Dynamics Simulation, Langmuir, 27 (2011) 7926-7933.

[112] J.P. DeRocher, B.T. Gettelfinger, J. Wang, E.E. Nuxoll, E.L. Cussler, Barrier membranes with different sizes of aligned flakes, Journal of Membrane Science, 254 (2005) 21-30.

[113] N.K. Lape, E.E. Nuxoll, E.L. Cussler, Polydisperse flakes in barrier films, Journal of Membrane Science, 236 (2004) 29-37.

[114] J. Zhao, A.B. Morgan, J.D. Harris, Rheological characterization of polystyrene–clay nanocomposites to compare the degree of exfoliation and dispersion, Polymer, 46 (2005) 8641-8660.

[115] J. Brandrup, E. Immergut, E.A. Grulke, Polymer handbook. 1999, There is no corresponding record for this reference.

[116] D.Q. Vu, W.J. Koros, S.J. Miller, Mixed matrix membranes using carbon molecular sieves: II. Modeling permeation behavior, Journal of Membrane Science, 211 (2003) 335-348.

[117] E. Gorlier, J.M. Haudin, N. Billon, Strain-induced crystallisation in bulk amorphous PET under uni-axial loading, Polymer, 42 (2001) 9541-9549.

[118] B. Lepoittevin, P. Roger, Poly(ethylene terephthalate), in: Handbook of Engineering and Speciality Thermoplastics, John Wiley & Sons, Inc., 2011, pp. 97-126.

[119] G. Li, S.L. Yang, J.M. Jiang, C.X. Wu, Crystallization characteristics of weakly branched poly(ethylene terephthalate), Polymer, 46 (2005) 11142-11148.

[120] C.I.W. Calcagno, C.M. Mariani, S.R. Teixeira, R.S. Mauler, The effect of organic modifier of the clay on morphology and crystallization properties of PET nanocomposites, Polymer, 48 (2007) 966-974.

[121] M. Frounchi, A. Dourbash, Oxygen Barrier Properties of Poly(ethylene terephthalate) Nanocomposite Films, Macromolecular Materials and Engineering, 294 (2009) 68-74.

[122] M. Ros-Chumillas, Y. Belissario, A. Iguaz, A. López, Quality and shelf life of orange juice aseptically packaged in PET bottles, Journal of Food Engineering, 79 (2007) 234-242.

[123] A. Shirakura, M. Nakaya, Y. Koga, H. Kodama, T. Hasebe, T. Suzuki, Diamond-like carbon films for PET bottles and medical applications, Thin Solid Films, 494 (2006) 84-91.

[124] M.K. Akkapeddi, T.J. Kraft, E.P. Socci, Oxygen scavenging high barrier polyamide compositions for packaging applications, in, Google Patents, 2002.

[125] L.H. Carlblom, J.A. Seiner, K.W. Niederst, Multilayer packaging material for oxygen sensitive food and beverage, in, Google Patents, 1998.

[126] K. Sonneveld, What drives (food) packaging innovation?, Packaging Technology and Science, 13 (2000) 29-35.

[127] J. Lange, Y. Wyser, Recent innovations in barrier technologies for plastic packaging—a review, Packaging Technology and Science, 16 (2003) 149-158.

[128] M. Ozdemir, C.U. Yurteri, H. Sadikoglu, Physical polymer surface modification methods and applications in food packaging polymers, Critical reviews in food science and nutrition, 39 (1999) 457-477.

[129] M. Di Lorenzo, M. Errico, M. Avella, Thermal and morphological characterization of poly (ethylene terephthalate)/calcium carbonate nanocomposites, Journal of Materials Science, 37 (2002) 2351-2358.

[130] W. Gao, X. Ma, Z. Wang, Y. Zhu, The influence of surface modification on the structure and properties of a calcium carbonate filled poly (ethylene terephthalate), Colloids and Surfaces A: Physicochemical and Engineering Aspects, 389 (2011) 230-236.

[131] D. Arencon, J. Velasco, The influence of injection-molding variables and nucleating additives on thermal and mechanical properties of short glass fiber/PET composites, Journal of Thermoplastic Composite Materials, 15 (2002) 317-336.

[132] P. Rojanapitayakorn, P. Mather, A. Goldberg, R. Weiss, Optically transparent self-reinforced poly (ethylene terephthalate) composites: molecular orientation and mechanical properties, Polymer, 46 (2005) 761-773.

[133] A. Pegoretti, J. Kolarik, C. Peroni, C. Migliaresi, Recycled poly(ethylene terephthalate)/layered silicate nanocomposites: morphology and tensile mechanical properties, Polymer, 45 (2004) 2751-2759.

[134] T.V. Duncan, Applications of nanotechnology in food packaging and food safety: Barrier materials, antimicrobials and sensors, Journal of Colloid and Interface Science, 363 (2011) 1-24.

[135] C. Silvestre, D. Duraccio, S. Cimmino, Food packaging based on polymer nanomaterials, Progress in Polymer Science, 36 (2011) 1766-1782.

[136] K. Soon, E. Harkin-Jones, R.S. Rajeev, G. Menary, P.J. Martin, C.G. Armstrong, Morphology, barrier, and mechanical properties of biaxially deformed poly(ethylene terephthalate)-mica nanocomposites, Polymer Engineering & Science, 52 (2012) 532-548.

[137] M.D. Sanchez-Garcia, E. Gimenez, J.M. Lagaron, Novel PET Nanocomposites of Interest in Food Packaging Applications and Comparative Barrier Performance With Biopolyester Nanocomposites, Journal of Plastic Film and Sheeting, 23 (2007) 133-148.

[138] S. Li, K. Auddy, P. Barber, T.J. Hansen, J. Ma, H.C. zur Loye, H.J. Ploehn, Thermal, mechanical, and barrier properties of polyethylene terephthalate-platelet nanocomposites prepared by in situ polymerization, Polymer Engineering & Science, 52 (2012) 1888-1902.

[139] M. Dini, T. Mousavand, P.J. Carreau, M.R. Kamal, M.T. Ton-That, Effect of water-assisted extrusion and solid-state polymerization on the microstructure of PET/Clay nanocomposites, Polymer Engineering & Science, (2013).

[140] G.D. Barber, B.H. Calhoun, R.B. Moore, Poly(ethylene terephthalate) ionomer based clay nanocomposites produced via melt extrusion, Polymer, 46 (2005) 6706-6714.

[141] H. Ghasemi, P.J. Carreau, M.R. Kamal, S.H. Tabatabaei, Properties of PET/clay nanocomposite films, Polymer Engineering & Science, 52 (2012) 420-430.

[142] A. Ammala, C. Bell, K. Dean, Poly(ethylene terephthalate) clay nanocomposites: Improved dispersion based on an aqueous ionomer, Composites Science and Technology, 68 (2008) 1328-1337.

[143] K. Majdzadeh-Ardakani, E.A. Lofgren, S.A. Jabarin, The effect of particle size distribution on the dispersion of nanoclays in poly (ethylene terephthalate)/clay nanocomposites, Journal of Reinforced Plastics and Composites, (2013) 0731684413512229.

[144] K. Jang, J. Lee, I.-K. Hong, S. Lee, Effect of supercritical carbon dioxide as an exfoliation aid on bio-based polyethylene terephthalate glycol-modified/clay nanocomposites, Korea-Aust. Rheol. J., 25 (2013) 145-152.

[145] M. Hassan, M. Cakmak, Mechano optical behavior of polyethylene terephthalate films during simultaneous biaxial stretching: Real time measurements with an instrumented system, Polymer, 54 (2013) 6463-6470.

[146] A. Tuteja, P.M. Duxbury, M.E. Mackay, Multifunctional Nanocomposites with Reduced Viscosity, Macromolecules, 40 (2007) 9427-9434.

[147] M.E. Mackay, T.T. Dao, A. Tuteja, D.L. Ho, B. Van Horn, H.-C. Kim, C.J. Hawker, Nanoscale effects leading to non-Einstein-like decrease in viscosity, Nature materials, 2 (2003) 762-766.

[148] J.C.H. Affdl, J.L. Kardos, The Halpin-Tsai equations: A review, Polymer Engineering & Science, 16 (1976) 344-352.

[149] Y. Wang, J. Gao, Y. Ma, U.S. Agarwal, Study on mechanical properties, thermal stability and crystallization behavior of PET/MMT nanocomposites, Composites part B: engineering, 37 (2006) 399-407.

[150] R.G. Matthews, A. Ajji, M.M. Dumoulin, R.E. Prud'homme, The effects of stress relaxation on the structure and orientation of tensile drawn poly(ethylene terephthalate), Polymer, 41 (2000) 7139-7145.

[151] T.H. Kim, S.T. Lim, C.H. Lee, H.J. Choi, M.S. Jhon, Preparation and rheological characterization of intercalated polystyrene/organophilic montmorillonite nanocomposite, Journal of Applied Polymer Science, 87 (2003) 2106-2112.

[152] H.-N. Vu, A. Vermogen, C. Gauthier, K. Masenelli-Varlot, J.-Y. Cavaillé, Microstructure and fracture behavior of semicrystalline polymer–clay nanocomposites, Journal of Polymer Science Part B: Polymer Physics, 46 (2008) 1820-1836.

[153] X.L. Ji, J.K. Jing, W. Jiang, B.Z. Jiang, Tensile modulus of polymer nanocomposites, Polymer Engineering & Science, 42 (2002) 983-993.

[154] I.-N. Jan, T.-M. Lee, K.-C. Chiou, J.-J. Lin, Comparisons of Physical Properties of Intercalated and Exfoliated Clay/Epoxy Nanocomposites, Industrial & Engineering Chemistry Research, 44 (2005) 2086-2090.

[155] T. Sakai, H. Takenaka, N. Wakabayashi, Y. Kawami, E. Torikai, Gas permeation properties of solid polymer electrolyte (SPE) membranes, Journal of the Electrochemical society, 132 (1985) 1328-1332.

[156] A. Polyakova, R.Y.F. Liu, D.A. Schiraldi, A. Hiltner, E. Baer, Oxygen-barrier properties of copolymers based on ethylene terephthalate, Journal of Polymer Science Part B: Polymer Physics, 39 (2001) 1889-1899.

[157] N. Muruganandam, W.J. Koros, D.R. Paul, Gas sorption and transport in substituted polycarbonates, Journal of Polymer Science Part B: Polymer Physics, 25 (1987) 1999-2026.

AUTOBIOGRAPHY

NAME

Fengyuan Yang

EDUCATION

- **Ph.D. (2014)** *in Materials Science and Engineering*, The Johns Hopkins University.
- **MS (2009)** *in Materials Processing Engineering*, Beijing University of Chemical Technology.
- **BS (2006)** *in Polymer Science and Engineering*, Beijing University of Chemical Technology.
- **Minor (2006)** *in Computer Science and Engineering*, Beijing University of Chemical Technology.

PBLICATIONS

1. **Fengyuan Yang**, Mihai Manitiu, Robert Kriegel and Rangaramanujam M. Kannan. Supercritical CO_2 dispersed polystyrene/ clay nanocomposites: structure, rheology and permeability. Polymer (Accepted)
2. **Fengyuan Yang**, Robert Kriegel and Rangaramanujam M. Kannan. Effects of super critical carbon dioxide processing and composition on rheological and barrier properties of polystyrene-clay nanocomposites. Journal of Membrane Science (Submitted May. 2014)
3. **Fengyuan Yang**, Christopher Mubarak, Robert Kriegel and Rangaramanujam M. Kannan. Supercritical carbon dioxide ($scCO_2$) dispersion of poly (ethylene terephthalate)/clay nanocomposites: structural, mechanical, thermal and barrier properties. Composite Science and Technology (Submitted May. 2014)
4. **Fengyuan Yang**, Christopher Mubarak, Robert Kriegel and Rangaramanujam M. Kannan. Effects of supercritical carbon dioxide processing and clay modification on structural, mechanical, rheological and barrier properties of poly (ethylene terephthalate)/clay nanocomposites. European Polymer Journal (In preparation)
5. Juan M. Gonzalez, Claus V. Franzke, **Fengyuan Yang**, Roberto Romero, Guillermina Girardi. Complement activation triggers metalloproteinases release inducing cervical remodeling and preterm birth in mice, The American Journal of Pathology, 179 (2), 2011, 838-849.